University of Alberta

CONTRIBUTIONS TO OCEAN AND SEA ICE MODELLING WITH APPLICATION TO THE MODELLING OF THE SUBPOLAR NORTH ATLANTIC OCEAN

by

Daniel Deacu ©

A thesis submitted to the Faculty of Graduate Studies and Research in partial fulfillment of the requirements for the degree of **Doctor of Philosophy**.

Department of Earth and Atmospheric Sciences

Edmonton, Alberta
Spring 2006

Your file Votre référence
ISBN: 0-494-13959-5
Our file Notre référence
ISBN: 0-494-13959-5

Abstract

The first part of the thesis investigates the effect of the Gent-McWilliams (GM) parameterization with a variable eddy transfer coefficient in an eddy-permitting ocean model of the subpolar North Atlantic. One of the improvements obtained is a better representation of the overflow waters originating from the Nordic Seas, leading to a more realistic Deep Western Boundary Current, as well as to an increased eddy activity in the deep ocean in the eastern North Atlantic. In addition, the GM velocities "help" the Labrador Sea Water spread from the deep convection region to the currents that surround it, without incurring significant spurious diapycnal mixing. Furthermore, the simulated Labrador Current and the near-surface circulation in the eastern North Atlantic are in a better agreement with flow patterns inferred from observations. Although the variability of the flow is reduced in the experiments with variable eddy transfer coefficients, overall, their use has led to better representations of the general circulation and hydrography in the subpolar North Atlantic. An extended integration of the same model is then examined, focusing on the adjustment of the intermediate and deep waters as well as on model stability. It is shown that the model is able to retain a good representation of the water masses, especially in the Labrador Sea, through the full integration. It is also shown that open boundary conditions do not generate significant model drift, even for integrations approaching a century in length.

In the second part, a new particle model (SPICE) for sea ice dynamics that has no underlying grid is developed and tested. The evolution equations of the pack ice thickness, ice fraction and horizontal area of an arbitrary particle ensure that the ice volume of that particle is conserved. Additionally, each particle preserves its thickness as long as ridging does not occur. A corrected Smoothed Particle Hydrodynamics technique and a variable smoothing length are used for the computation of the spatial derivatives. The model was tested with two different rheologies in an idealized case of an ice pack with a free edge driven by a vortex wind. The simulations with SPICE using a nonlinear viscous rheology are compared with simulations with a more complex Lagrangian finite element model. The predicted locations of the free ice edge compare very well. Because the thickness transport is not plagued by numerical diffusion, the simulated ice edges are not eroded by thickness diffusion. The development of linear kinematic features as narrow bands of intense shearing that separate regions with quasi-uniform motion is simulated in experiments with a viscous-plastic rheology, showing that SPICE is able to simulate complex sea ice dynamics.

Table of Contents

List of Tables

List of Figures

List of Symbols, Nomenclature and Abbreviations

T^{-1}	Eady growth rate of the unstable baroclinic waves
f	Coriolis parameter
Ri	large-scale Richardson number
α	universal constant (Chapter 2)
	ridging function (Chapter 4)
k	eddy transfer coefficient
L	length scale of the baroclinic region
μ	universal constant
λ	local Rossby radius of deformation (Chapter 2)
	ice strength parameter (Chapter 4)
N	buoyancy frequency
g	gravitational acceleration
ρ	locally referenced density of seawater (Chapter 2)
	density of ice-water mixture (Chapter 4)
ρ_0	reference density of seawater
u, v	horizontal components of the velocity vector
S_{rho}	isopycnal slope
A_h	biharmonic horizontal viscosity coefficient
K_h	biharmonic horizontal diffusion coefficient
A_v	vertical viscosity coefficient
K_v	vertical diffusion coefficient
σ_0	potential density of sea water
Sv	Sverdrup
S	salinity (Chapters 2 and 3)
	horizontal area of an arbitrary pack ice particle (Chapter 4)
S_r	reference salinity
V	volume
psu	practical salinity unit
c_p	specific heat capacity of water
T	seawater temperature
T_r	reference temperature

FW	freshwater content
H	heat content (Chapter 3)
	sea surface elevation relative to a reference level (Chapter 4)
$\vec{u}$	horizontal velocity
$\boldsymbol{N}^e$	depth-integrated extra-stress within pack ice
ρ_{ice}	ice density
ρ_w	water density
h_{ice}	ice thickness
h_w	thickness of lead water column
A	ice fraction
h	mean thickness of an arbitrary pack ice particle
m	mass of mixture within an arbitrary pack ice particle
m_{ice}	mass of ice within an arbitrary pack ice particle
β	divergence of the horizontal velocity field
Γ	Heaviside function
A_c	critical ice fraction
$\tau^{\vec{a}}$	wind stress
$\tau^{\vec{w}}$	water stress
$\vec{F}$	resultant force acting on an arbitrary pack ice particle
$\vec{r}$	position vector
$\vec{r_p}$	position vector of an arbitrary pack ice particle
$\boldsymbol{\sigma}^E$	ice stress
σ^*	compressive strength of compact sea ice
$\boldsymbol{I}$	identity tensor
$\boldsymbol{D}$	strain rate tensor
ϕ_0, ϕ_1	viscous response functions
ϕ_b	bulk response functions
D_{ij}, $\dot{\epsilon}_{ij}$	arbitrary component of the strain rate tensor
P_{GM}	compressive strength of pack ice
γ	maximum shear strain rate
p^E	mechanical pressure
β_c	prescribed dilation rate value
γ_c	constant shear strain rate value
q^E	maximum shear stress
Φ	friction angle
Φ^*	limit friction angle
ϕ_s^*	sine of the limit friction angle
ζ	nonlinear bulk viscosity
η	nonlinear shear viscosity
P_{HS}	pack ice pressure
Δ	combined strain rate invariant
P^{yield}	compressive strength of pack ice
e	ratio of the major axis to the minor axis of an elliptical yield curve

p^e	depth-integrated mechanical pressure
ξ	smoothing length
W	kernel function
W^*	corrected kernel function
∇^*	corrected gradient
κ	smoothing length parameter
δt	time step size
δU	typical velocity variation
ω	angular velocity
χ	parameter of a vortex wind field
R	distance to the centre of a wind vortex
C_a	wind drag coefficient
C_w	water drag coefficient
ψ_a	air drag turning angle
ψ_w	water drag turning angle
V_g	geostrophic wind velocity
V_w	geostrophic ocean current velocity
P^*	maximum compressive strength of sea ice
$slpderivmax_{max}$	maximum value of the vertical derivative of the isopycnal slope
$taper$	tapering coefficient
KEM	kinetic energy of the mean flow
EKE	eddy kinetic energy
MKE	mean kinetic energy
$MOSF$	maximum value of the meridional overturning stream function at 40°
MAR	Mid-Atlantic Ridge
LC	Labrador Current
ETOPO5	Earth Topography - 5 minute
NOAA	National Oceanic & Atmospheric Administration (USA)
NAC	North Atlantic Current
LSW	Labrador Sea Water
DWBC	Deep Western Boundary Current
ISOW	Iceland-Scotland Overflow Water
DSOW	Denmark Strait Overflow Water
CGFZ	Charlie-Gibbs Fracture Zone
MOC	Meridional Overturning Circulation
BBL	Bottom Boundary Layer
PIC	particle-in-cell
SPH	Smoothed Particle Hydrodynamics
LKF	Linear Kinematic Feature
SB1	shear band 1

Chapter 1

Introduction

The North Atlantic Ocean plays a very important role in the climate system, because it transports a large amount of heat (or, more correctly, energy) towards high latitudes; the estimated transport is about 1.2×10^{15} W at 24°N (Trenberth and Caron, 2001). Therefore, it moderates the regional climate. For instance, the northwestern Europe has a milder climate than eastern Canada, at the same latitudes. The northward transport of warm and salty water in the upper layers via the Gulf Stream and the North Atlantic Current is matched by a southward transport of cold and dense water at depth, via the Deep Western Boundary Current. While the surface circulation is mainly wind-driven, that at depth is density-driven, and its strength is controlled by the amount of dense waters formed through deep convection in the Greenland, Iceland and Norwegian (GIN) Seas and the Labrador and Irminger Seas. The surface and deep currents generate the Atlantic Meridional Overturning Circulation (AMOC) whose strength (crucial in determining the northward oceanic heat transport) is used as a very important climate indicator. This is why oceanographers and climate scientists put considerable effort into its estimation, monitoring, and long-term prediction.

There is a growing concern that changes in the thermohaline forcing at high latitudes, such as increased amounts of fresh water released by accelerated melting of the Arctic ice cap, may lead to lower rates of dense water formation in a not too distant future. This would entail a slowdown of the deep circulation, and hence of the AMOC. Consequently, this could affect the stability and variability of the climate. Such an impact on the climate can be investigated in climate models, but the accuracy depends on the degree of realism of the simulations with these models. Reliable long-term predictions require that the ocean component of the climate models be able to simulate both the formation of deep waters and their transport accurately.

Physical processes in the subpolar gyre of the North Atlantic Ocean have a significant impact on the variability of the AMOC (Köhl, 2005). Of particular interest in this context are the formation through deep convection, in the Labrador Sea, of the Labrador Sea Water (LSW) and its spreading at intermediate depths within the North Atlantic basin. The deep circulation in the Labrador Sea and the LSW dispersal have received considerable attention since the mid-nineties, when several observational research programs started (Lavender et al., 2000; Fischer and Schott, 2002). The availability of observational data then prompted modelling studies investigating the dynamics of the observed regional circulation, and the water mass distribution and spreading (e.g. Käse et al., 2001; Myers, 2002; Myers and Deacu, 2004; Treguier et al., 2005). Although the ocean models used in these studies have reasonable skill, more accurate simulations are needed, and these can be obtained only if the models undergo continuous improvement.

In most of the real ocean, fluid parcels move along neutral surfaces (i.e. locally referenced isopycnal surfaces). This behaviour is poorly simulated in z-level ocean models – the grid points of such a model lie in horizontal planes, at predefined depths – due to the alteration of the salinity and temperature of water parcels by spurious mixing. For instance, significant spurious diapycnal mixing arises in such models when using horizontal rather than isopycnal mixing operators. The horizontal alignment of the explicit mixing of tracers has catastrophic effects on the representation of water masses and, subsequently, on the simulated ocean circulation. Moreover, the level of artificial mixing is magnified when large horizontal diffusivities are needed to maintain numerical stability of the model.

One way to reduce spurious mixing in non-eddy-resolving z-level ocean models is to replace the explicit tracer diffusion operators with an eddy parameterization. Gent and McWilliams (1990) devised a mesoscale eddy parameterization that provides a physically-based and more accurate stirring and mixing of tracers in non-eddy-resolving models. This can be implemented by means of a non-divergent eddy-induced velocity, whose horizontal component has the form

$$\mathbf{u}_h = -\partial_z(k\mathbf{L}), \quad \text{with } \mathbf{L} = -\frac{\nabla_h \rho}{\rho_z}. \tag{1.1}$$

Here, k is the eddy transfer coefficient, which is related to the strength of the mesoscale eddy stirring, ρ is the locally-referenced density, and $\mathbf{L}$ is the isopycnal slope vector. The sum of the eddy-induced velocity and the fluid velocity is then used as the transport velocity in the advective terms of the tracer equations.

The Gent-McWilliams parameterization has had a profound impact in the field of ocean and climate modelling. An example is the simulation of an enhanced northward heat transport in the North Atlantic Ocean (Danabasoglu et al., 1994). However, at the time the research presented in this thesis was started, it was largely believed that this type of adiabatic mixing parameterization could only be used in the non-eddy-resolving regime. An eddy-resolving ocean models is one that resolves the local baroclinic Rossby radius (the typical length scale of the baroclinic eddies), hence its resolution is less than $0.1°$. In the range of resolutions $0.1 - 1°$ models are only marginally-eddy-resolving/eddy-permitting. Since these models cannot fully resolve the mesoscale eddy field, the use of a refined form of the GM parameterization is largely justified. In support of this are studies indicating that some form of adiabatic mixing is required in z-level models, both in the eddy-permitting (Willebrand et al., 2001) and the eddy-resolving regime (Roberts and Marshall, 1998).

One of the main goals of this thesis is to contribute to the ocean modelling of the subpolar North Atlantic Ocean. Thus, the first part of this thesis (Chapters 2 and 3) addresses the parameterization of the effects of mesoscale eddies on tracers in eddy-permitting ocean models. Chapter 2 presents the implementation of a refined parameterization of the effect of the unresolved baroclinic eddies on tracers (salinity and temperature) in a z-level eddy-permitting model of the subpolar North Atlantic (SPOM), and thoroughly investigates its impact on the regional ocean circulation and the representation of water mass properties (with emphasis on the LSW and its dispersal pathways).

Because an increasing number of climate models incorporate eddy-permitting global ocean circulation models (e.g. Gent et al., 2002; Roberts et al., 2004), of great interest is the investigation of the long time behaviour of SPOM with the refined parameterization. An 80-year long integration of the model is analyzed in Chapter 3 to assess the impact of the parameterization after the spin-up phase. The focus is on the ability of the model to preserve the water mass characteristics over periods of time spanning decades of integration from an initial state of rest, under perpetual forcing, as well as on the model's stability.

The results presented in Chapters 2 and 3 have been obtained with an ocean model whose surface salinity and temperature were relaxed towards climatological values rather than being forced with buoyancy fluxes. Although natural, forcing an ocean model with heat and freshwater fluxes needs particular attention, since it may cause a rapid drift of the near-surface temperature and salinity towards unrealistic values, in the absence of any relaxation components/flux adjustment. This is generally considered as a result of lack of two-way interaction between ocean and atmosphere/sea-ice. It is thus sensible to expect to obtain more accurate simulations of the general ocean circulation in global coupled ice-ocean-atmosphere-land models. But, simulations with a global coupled model whose ocean component is eddy-permitting, or eddy-resolving, are still very computationally expensive. Therefore, as far as we are concerned, numerical investigations of the water mass formation and ocean circulation in the subpolar North Atlantic that require multiple and long integrations, such as testing of new parameterizations, sensitivity studies and the response to different forcing scenarios, are more likely to be carried out with regional ice-ocean models.

In the subpolar North Atlantic, sea ice can be found along the west coast of Greenland as well as on the Labrador and Newfoundland shelves. Although there is local growth in these areas, a significant amount of this sea ice is formed north of the Denmark Strait and in the Baffin Bay, and then it is transported by the East Greenland Current, and the Baffin Island and Labrador Currents, respectively. Characteristic to subpolar seas is the formation of the Marginal Ice Zone (MIZ) along the free ice edge (Wadhams, 2000), as a region of low sea ice concentration. This is the result of the continuous action of waves that break up large ice floes into smaller floes, followed by increased melting as these floes reach warmer waters in the open ocean. The location of the free ice edge usually signals the existence of oceanic fronts in its proximity. These oceanic features are highly unstable and generate eddying motions that induce large deformations in the ice pack.

The presence of sea ice modifies the momentum and buoyancy fluxes at the ocean surface, which are the main driving forces of the ocean circulation. Sea ice acts as an insulator for the relatively warm underlying ocean, leading to reduced loss of heat from the ocean to the atmosphere. A positive freshwater flux results from sea ice melting, and this increases the buoyancy of the sea water in the surface layer. A decrease in buoyancy occurs as a result of the brine rejection associated with sea ice growth. The generation of a freshwater cap in regions where deep convection usually occurs decreases the rate of dense water formation and, in extreme situations, may even stop this process. This is actually a scenario that has been investigated by oceanographers and climate scientists, more precisely, that of anomalously large freshwater fluxes resulting from increased precipitation, and land and sea ice melt due to greenhouse warming that could trigger significant changes in the AMOC and, subsequently, in the northward heat transport. There is a lot of debate on this subject as well as skepticism, mainly because the investigations have been conducted with numerical models. Nonetheless, a recent study by Curry and Mauritzen (2005) focusing on the quantification of the freshwater input and storage in the northern North Atlantic from observed data comes in its support. Based on the trend in the freshening of the sea water over the last four decades in this region, which includes the effect of the Great Salinity Anomaly (GSA) of the late 1960s and early 1970s – GSA was triggered by an anomalously large sea ice flux from the Arctic into the northern North Atlantic – the authors argue that a threshold that could lead to a very significant weakening of the AMOC could be reached in about one century.

There are also processes known to occur in subpolar seas as a result of ice-ocean dynamic interaction, which can only be simulated with a coupled ice-ocean model. An example is the upwelling/downwelling at the ice edge that occurs when the wind blows along the ice edge that has been both observed (Tang and Ikeda, 1989) and simulated with coupled ice-ocean models (Ikeda, 1985). Ice edge upwelling/downwelling is the result of the higher drag felt by the water beneath the ice cover compared to that felt by the open water. The doming of the isopycnals during upwelling may play a preconditioning role in local deep convection (Häkkinen, 1987), and hence in deep water formation.

Coupling a sea-ice model to SPOM should lead to more accurate simulations. For instance, one of the expected results is that of the ice melt water flux having a significant contribution to the freshening of the model LSW. Improperly specified freshwater flux at the ocean surface has been found to be one of the main factors responsible for the salinization of the LSW that currently plague most stand-alone ocean models (e.g. Treguier et al., 2005).

In a coupled model, the ice and the ocean components are usually run on the same horizontal grid. Because the number of degrees of freedom of the ice component is much smaller than that of the ocean, its resolution could be increased (while keeping that of the ocean constant) without raising the computational cost too much. Thus, a more accurate simulation of the dynamics and thermodynamics of the ice cover could be achieved. Eventually, this would lead to a more realistic representation of the atmosphere-ice-ocean interaction, and the recent study of Stössel and

Kim (2006) proves just that. Stössel and Kim (2006) show that refining the resolution of the ice component of their coupled ice-ocean model, in the Southern Ocean, leads to improved buoyancy forcing in the region, more realistic ice thickness distribution and a sharper ice edge. Interestingly, the high resolution allowed the use of coastal winds, which were shown to be critical in the deep water formation due to their influence on brine rejection during freezing in coastal polynyas.

No doubt, running a sea ice model at higher resolutions has many advantages. But, there are limits such as that imposed by the validity of the continuum hypothesis, which breaks down at the floe scale. In addition, if the model has poor conservation properties, higher resolutions may amplify the errors. Therefore, the sea ice model has to be carefully formulated and only used for the length scale range its rheology is valid for. It is also very important that the model be able to represent features that are characteristics to sea ice dynamics, such as large deformations along the free ice edge, crack development and localized shearing.

The second part of the thesis (Chapter 4) presents a new particle model for sea ice dynamics, which is formulated such that the ice mass of each particle is conserved. The model relies on Smoothed Particle Hydrodynamics techniques for its numerical integration, and is developed with a view of providing improved simulations of sea ice dynamics compared to traditional Eulerian models in areas where large deformations occur (e.g. marginal ice zone, bands of localized shear). This is the first step in building a dynamic-thermodynamic Lagrangian sea ice model, which will eventually be coupled with an ocean model of the subpolar North Atlantic and then used to provide a more accurate representation of the effect of ice-ocean interactions on the regional ocean circulation and hydrography. Nonetheless, the model could be used for short-term predictions (typical for sea ice forecasting), before adding the thermodynamic component to it.

Bibliography

Curry, R. and C. Mauritzen, 2005: Dilution of the northern North Atlantic Ocean in recent decades. *Science*, **308**, 1772–1774.

Danabasoglu, G., J. C. McWilliams, and P. R. Gent, 1994: The role of mesoscale tracer transports in the global ocean circulation. *Science*, **264**, 1123–1126.

Fischer, J. and F. A. Schott, 2002: Labrador Sea water tracked by profiling floats — from the boundary current into the open North Atlantic. *J. Phys. Oceanogr.*, **32**, 573–584.

Gent, P. R., A. P. Craig, C. M. Bitz, and J. W. Weatherly, 2002: Parameterization improvements in an eddy-permitting ocean model for climate. *J. Climate*, **15**, 1447–1459.

Gent, P. R. and J. C. McWilliams, 1990: Isopycnal mixing in ocean circulation models. *J. Phys. Oceanogr.*, **20**, 150–155.

Häkkinen, S., 1987: Upwelling at the ice edge: A mechanism for deep water formation? *J. Geophys. Res.*, **92**, 5031–5034.

Ikeda, M., 1985: A coupled ice-ocean model of a wind driven coastal flow. *J. Geophys. Res.*, **90**, 9119–9128.

Käse, R. H., A. Biastoch, and D. B. Stammer, 2001: On the mid-depth circulation in the Labrador and Irminger Seas. *Geophys. Res. Lett.*, **28**, 3433–3436.

Köhl, A., 2005: Anomalies of Meridional Overturning: Mechanisms in the North Atlantic. *J. Phys. Oceanogr.*, **35**, 1455–1472.

Lavender, K. L., R. E. Davis, and W. B. Owens, 2000: Mid-depth recirculation observed in the interior Labrador and Irminger Seas by direct velocity measurement. *Nature*, **407**, 66–69.

Myers, P. G., 2002: SPOM: A regional model of the sub-polar North Atlantic. *Atmos.-Ocean*, **40**, 445–463.

Myers, P. G. and D. Deacu, 2004: Labrador Sea freshwater content in a model with a partial cell topographic representation. *Ocean Modelling*, **6**, 359–377.

Roberts, M. J., H. Banks, N. Gedney, J. Gregory, R. Hill, S. Mullerworth, A. Pardaens, G. Rickard, R. Thorpe, and R. Wood, 2004: Impact of an eddy-permitting ocean resolution on control and climate change simulations with a global coupled GCM. *J. Climate*, **17**, 3–20.

Roberts, M. J. and D. Marshall, 1998: Do we require adiabatic dissipation schemes in eddy-resolving ocean models? *J. Phys. Oceanogr.*, **28**, 2050–2063.

Stössel, A. and J. T. Kim, 2006: Enhancing the resolution of sea ice in a global ocean GCM. *Ocean Modelling*, **11**, 28–48.

Tang, C. L. and M. Ikeda, 1989: Ice-edge upwelling off the Newfoundland coast during LIMEX. *Atmos.-Ocean*, **27**, 658–681.

Treguier, A. M., S. Theetten, E. P. Chassignet, T. Penduff, R. Smith, L. Talley, J. O. Beismann, and C. Böning, 2005: The North Atlantic Subpolar Gyre in four high-resolution models. *J. Phys. Oceanogr.*, **35**, 757–774.

Trenberth, K. E. and J. M. Caron, 2001: Estimates of meridional atmosphere and ocean heat transports. *J.Climate*, **14**, 3433–3443.

Wadhams, P., 2000: Ice in the ocean. CRC Press.

Willebrand, J., B. Barnier, C. Böning, C. Dieterich, P. D. Killworth, C. Le Provost, Y. Jia, J. M. Molines, and A. L. New, 2001: Circulation characteristics in three eddy-permitting models of the North Atlantic. *Prog. Oceanogr.*, **48**, 123–161.

Chapter 2

Effect of a Variable Eddy Transfer Coefficient in an Eddy-Permitting Model of the Subpolar North Atlantic Ocean

2.1 Introduction

The effects of baroclinic eddies on tracers need to be parameterized in coarse resolution ocean models. Gent and McWilliams (1990) proposed a mesoscale eddy parameterization scheme (hereafter denoted by GM) for z-coordinate models that can be implemented by adding a so-called "bolus velocity" (Gent et al., 1995) to the mean transport velocity employed for the advection terms in the tracer equations. The net effect of this eddy-induced velocity is expected to be that of stirring tracers quasi-adiabatically along isopycnal/isoneutral surfaces, similar to that produced by mesoscale eddies. Numerous studies have shown that the GM parameterization leads to improved model fields in coarse resolution models, including enhanced northward transport of heat in the North Atlantic, sharper thermoclines, and cooler deep oceans (Danabasoglu et al., 1994; Danabasoglu and McWilliams, 1995; Böning et al., 1995). These improvements resulted from simultaneous use of the GM scheme and a low, or even zero horizontal diffusion, which reduces consid-

[1]A version of this chapter has been published. Deacu, D. and P. G. Myers, 2005. Journal of Physical Oceanography, **35**, 289-307

erably the spurious diapycnal mixing and the ensuing spurious upwelling (Böning et al., 1995).

Simulations from an eddy-permitting ($1/3°$ resolution) z-coordinate model of the North Atlantic reported by Willebrand et al. (2001) showed that the unphysical diapycnal upwelling in the western boundary current region was the result of the tracer diffusion by means of the biharmonic horizontal diffusion scheme. The authors conclude that a non-diffusive/adiabatic scheme for tracer stirring and mixing might preclude this unwanted effect even in the eddy-permitting regime, in a manner similar to that in non-eddy-resolving models. An example that the GM scheme may be beneficial in eddy-permitting models has been reported by Haines and Wu (1998), where it improved the dispersal of the Levantine Intermediate Water in a model of the Mediterranean. Even in the eddy-resolving regime, Roberts and Marshall (1998) have argued that adiabatic dissipation schemes are still required since significant spurious diapycnal mixing is generated by horizontal tracer diffusion schemes, while Maltrud and McClean (2005) have mentioned that an adiabatic eddy mixing scheme could improve simulations with their $1/10°$ global ocean model.

In all of the listed studies that used the GM scheme (and many others), the strength of the eddy stirring of tracers was represented by a constant eddy transfer coefficient. England and Holloway (1998) reported negative effects when a relatively large value of this coefficient, namely $10^7\ cm^2\ s^{-1}$, was used everywhere in a series of North Atlantic simulations, and suggested that a spatially and temporally varying coefficient could be a remedy. A similar suggestion has been made by Beismann and Redler (2003) who found that the GM scheme with a constant eddy transfer coefficient led to an unrealistic pathway of the NADW in their model.

In order to take into account the inherent variability of the eddy-induced tracer transport in oceanic flows, Visbeck et al. (1997) proposed a method (hereafter referred to as VMHS) to calculate a variable eddy transfer coefficient that can be used with the GM scheme in coarse resolution ocean models. This coefficient is assumed to be proportional to the Eady growth rate of the unstable baroclinic waves, T^{-1}, given by,

$$T^{-1} = \frac{f}{\sqrt{Ri}}, \tag{2.1}$$

and to the square of a length scale, L, of the baroclinic region. Its expression is

$$k = \alpha T^{-1} L^2, \tag{2.2}$$

where f is the Coriolis parameter, Ri is the large-scale Richardson number, and α is a constant equal to 0.015.

Bryan et al. (1999) compared predictions of the magnitude of the bolus velocity yielded by the GM scheme employing a constant eddy mixing coefficient, a VMHS-like coefficient, and the variable eddy coefficient formulation of Held and Larichev (1996), with magnitudes from diagnostic calculations performed with their eddy-permitting model outputs. They found that the prediction with the VMHS-like coefficient given by,

$$k = \mu T^{-1} \lambda^2, \tag{2.3}$$

where μ is a constant equal to 0.13 and λ is the local Rossby radius of deformation, was the best fit to the model. Wright (1997) also found that the VMHS coefficient led to improvements in their $1.25°$ resolution model as compared to simulations with a constant eddy coefficient.

Gent et al. (2002) used the GM parameterization with the VMHS coefficient in an eddy-permitting global ocean model (having an average horizontal resolution of $\sim 0.7°$). Although they found that the VMHS scheme only produced minor differences in the global fields as compared to a constant eddy coefficient, the authors concluded that significant local differences could occur in regions where the variable eddy coefficient becomes larger, such as the Antarctic Circumpolar Current and the northern North Atlantic.

Observations conducted in the Labrador Sea have revealed the ubiquitous presence of geostrophic eddies with a length scale of about 10 km (approximately equal to typical Rossby radius of deformation values for that region) and baroclinic instability in the convection region (The Lab Sea Group, 1998). Eddy-permitting ocean models are a class of models that can simulate large eddies but do not allow for the geostrophic eddy field to be fully resolved since their horizontal grid spacing is still larger than the Rossby radius of deformation. This inability to resolve the Rossby radius is more preponderant towards high latitudes as the ratio of the local horizontal grid spacing to the local Rossby radius increases. Therefore, processes such as meandering of baroclinically unstable currents leading to a growth phase and the ultimate spawning of a baroclinic eddy are not simulated adequately. It is very likely that due to constraints imposed by the grid size, a resolved baroclinic eddy is only spawned after certain thresholds for available potential energy and velocity shear have been exceeded. It may be, for the case of frontal regions, that some large amount of available potential energy needs to be accumulated before it can be released by the shedding of baroclinic eddies of a scale sufficiently large to be resolved by the model grid. Sudden release of available potential energy can generate very energetic eddies that may have a negative impact on the model circulation in a region. Since the transport of tracers by the unresolved mesoscale eddies still needs to be parameterized in eddy-permitting models, the option of an eddy transfer coefficient varying according to the local susceptibility to baroclinic instability should have a positive contribution to the removal of available potential energy, and thus lead to more realistic simulations.

Recent simulations performed with an eddy-permitting model ($1/3^\circ$ resolution) of the subpolar North Atlantic (Myers, 2002) showed that the use of a better topographic representation (based on the partial cell approach of Adcroft et al. (1997)) leads to an improved representation of the circulation in that region. However, the changes to the circulation caused the model salinity in the Labrador Sea to drift to unrealistically high values. An overly strong Labrador Sea countercurrent caused excessive entrainment of high salinity water from the North Atlantic Current (NAC) into the Labrador Sea (Myers and Deacu, 2004), and thus occasioned the salinity drift. Myers and Deacu (2004) suggested that increased baroclinic eddy activity in the partial cell simulation might have been responsible for the acceleration of the countercurrent.

With the importance of eddy activity and instability processes in the simulations of Myers and Deacu (2004), a natural extension of that study was to consider the use of the GM scheme with VMHS-like eddy transfer coefficients. One result that might be expected would be a decreased baroclinic eddy activity due to an enhanced release of available potential energy in baroclinically unstable regions (e.g. frontal and deep-convection regions) since a very small value of the eddy transfer coefficient ($2.0 \times 10^5\ cm^2\ s^{-1}$) was used in the previous study. Additionally it was hoped that the improved representation of the eddy processes could permit reduced spurious diapycnal mixing through a drastic decrease of the horizontal tracer diffusivity.

Eddy-permitting ocean general circulation models are increasingly being used for climate studies (e.g. Roberts et al., 2004) and skillful eddy parameterizations are needed for these models to yield more accurate simulations (Gent et al., 1999). The main objective of the study presented in this paper is to investigate the effect of the use of the GM scheme with a variable eddy transfer coefficient, combined with a low level of horizontal diffusion, in simulations with an eddy-permitting model of the subpolar North Atlantic. In order to assess the relative contribution of using variable eddy transfer coefficients and reducing the explicit horizontal diffusion, we compare results from experiments that employ a spatially and temporally variable eddy transfer coefficient with results from two control experiments with constant values for this coefficient. One of the control experiments uses a value for the eddy transfer coefficient obtained as a spatial and time average of the eddy coefficient field from one of the experiments in which it is variable, and a small value for the biharmonic horizontal diffusion coefficient. The other one uses the settings of the model from previous studies, i.e. a lower value for the eddy transfer coefficient and a typical value of the biharmonic horizontal diffusion coefficient for the eddy-permitting regime.

The experiments with a variable eddy transfer coefficient correspond to two different implementations of the expressions (2.2) and (2.3) of this coefficient. The implementations are described in section 2.2, while more detail on the ocean model is given in section 2.3. Results from all experiments and their discussion are given in section 2.4. The conclusions are provided in section 2.5.

2.2 On the implementation of the VMHS eddy transfer coefficient in an eddy-permitting ocean circulation model

In an eddy-permitting ocean model, large geostrophic eddies can be simulated and their effect on tracers need not be parameterized. Therefore, the attention should be focused on parameterizing the smaller baroclinic eddies that cannot be explicitly resolved. The present study makes use of the assumption that, when using (2.2), this can be achieved to some extent by limiting the length scale of the baroclinic region, L, such that its upper bound is comparable to the length scale of the smallest eddies resolved by the model. Visbeck et al. (1997) devised a method of determining L based on the discrete field of the growth rate. Moreover, it is for this particular method that they found a value of 0.015 for the "universal" constant α. Since this value was considered by VMHS to be appropriate even for parameterizing baroclinic regions with relatively small length scales (see their convective chimney case, for example), which an eddy-permitting model cannot resolve at high latitudes, we chose to leave it unchanged.

In order to avoid overparameterizing the effects of the resolved eddies we set the upper limit for L to one degree of longitude, i.e. three times larger than the meridional grid size, which is constant in our model. Although this choice is not physically sound, it can be related to the minimum number of grid points in both zonal and meridional directions, required to represent an eddy on the horizontal grid properly. While the growth rate is precisely defined by (2.1), there is no such formal definition for the length scale L. We use the algorithm employed by the MOM3 model (Pacanowski and Griffies, 1998), and attributed to the Hadley Centre, to determine this length scale based on the previously calculated growth rate field. The details are given in Appendix A. When calculating the eddy transfer coefficient with formula (2.3), there is no need to limit λ (local Rossby radius) as this is at the lower end of the length scale range of mesoscale eddies (whose scale is typically 3-4 times larger than λ (Stammer, 1998)), i.e. exactly in the subrange of the mesoscale eddies unresolved by the eddy-permitting ocean models.

Note that, since λ does not require any input on setting its upper limit, one may find formula (2.3) preferable over formula (2.2) for computing the eddy transfer coefficient at different resolutions in the eddy-permitting regime. However, the limitation imposed on L leads to an overall decrease of this coefficient when increasing the resolution, which is more consistent with a narrower size range of the unresolved mesoscale eddies. No studies have been performed on the sensitivity of the eddy transfer coefficient given by the two formulas to the horizontal grid spacing. One way of dealing with the possible overparameterization of the effect of the mesoscale eddies in the eddy-permitting regime when using either Eq. (2.2) or Eq. (2.3) is to tune the constants α and μ, respectively.

The expression of the Richardson number in (2.1) is

$$Ri = \frac{N^2}{\left(\frac{du}{dz}\right)^2 + \left(\frac{dv}{dz}\right)^2}, \tag{2.4}$$

where N is the buoyancy frequency given by $N^2 = -\frac{g}{\rho_0}\frac{d\rho}{dz}$, g is the gravitational acceleration, ρ is the locally referenced density, ρ_0 is a reference density (with a value of $1g\ cm^{-3}$), and u and v are the horizontal components of the velocity vector. Two methods for calculating Ri have been considered. One of them (hereafter referred to as $STRAT$) follows the original VMHS approach, in which the velocity shear is expressed as a function of horizontal density gradients. The other (denoted by $SHEAR$) is similar to an implementation used at the Hadley Centre and directly calculates the velocity shear using the total velocity field, which is a prognostic variable.

In $STRAT$, the large-scale Richardson number (Ri) is calculated assuming that the mesoscale eddy field is quasi-geostrophic, which implies the existence of the thermal-wind balance. Therefore, the vertical velocity shear can be expressed in terms of horizontal density gradients. In this case, Ri becomes

$$Ri = \left(\frac{f}{NS_{rho}}\right)^2, \tag{2.5}$$

where S_{rho} stands for the isopycnal slope. Consequently, the reciprocal of the time scale (i.e. the growth rate) will depend on density gradients only,

$$T^{-1} = N\left|S_{rho}\right|. \tag{2.6}$$

The right-hand side of (2.6) is evaluated as an average for each vertical column over a depth interval where baroclinic eddies are most likely to occur. The lower and upper limits of this interval have been set to 100 m and 2000 m, respectively, as suggested by Treguier et al. (1997). Notice that due to vertical averaging the computed growth rate will not vary in the vertical direction.

The $SHEAR$ implementation makes direct use of (2.1) to compute the growth rate. The model directly evaluates the Richardson number from (2.4) as a depth average for each vertical column. The depth limits are the same as those given in the discussion of the $STRAT$ approach. The two implementations have been used for computing the eddy transfer coefficient using both (2.2) and (2.3). Four experiments have been performed, one for each combination of implementation and expression for the eddy transfer coefficient k. Those with k given by (2.2) will be referred to as $STRAT_L$, $SHEAR_L$, whereas $STRAT_\lambda$, and $SHEAR_\lambda$ will denote those with k calculated with (2.3).

Isopycnal surfaces can be very steep in some regions of the ocean (e.g. mixed layer, frontal and deep convection regions). Many of the commonly used isopycnal diffusion schemes (Cox, 1987) are only valid for small isopycnal slopes, as they are small-slope approximations of a general scheme proposed by Redi (1982). The limitation of isopycnal slopes to small values (e.g. 0.01, Danabasoglu et al. (1994)), also required for numerical stability (Cox, 1987), leads to significant spurious diapycnal fluxes of density (Mathieu, 1998). Therefore, in the absence of physical reasons for using the same slope limitation for the GM scheme (Mathieu, 1998), we have relaxed these limiting constraints, such that slopes of up to a maximum absolute value of 100 (corresponding to an almost vertical surface, with a maximum angle of $89.4°$) are used when calculating bolus velocity.

Since the *u*- and *v*-components of this velocity are proportional to the vertical derivatives of the *x*- and *y*-components of the isoneutral slope vector, respectively, very large values result in regions where these slopes exhibit a sudden decrease/increase. For example, this can happen at the base of the mixed layer and can generate spurious deepening (effect noticed in one of our test experiments). In order to reduce the amplitude of these negative effects, as well as to keep bolus velocity values within the range of values believed to occur in the ocean, i.e. less than 20 $cm\ s^{-1}$ (Mathieu, 1998), tapering of vertical derivatives of isopycnal slopes is necessary. A tapering formula of the form proposed by Gerdes et al. (1991) for isopycnal slopes has been used for tapering vertical derivatives of isopycnal slopes greater than a prescribed maximum value $slpderiv_{max} = 10^{-6}\ cm^{-1}$. The tapering coefficient is calculated with the formula

$$taper = \left(\frac{slpderiv_{max}}{|dS_{rho}/dz|}\right)^3, \tag{2.7}$$

where dS_{rho}/dz is the vertical derivative of the isopycnal slope. Thus, if the computed dS_{rho}/dz is larger than $slpderiv_{max}$, then it will be reduced by multiplication by $taper$. Note that for a maximum allowable eddy transfer coefficient of $10^7\ cm^2\ s^{-1}$ — Visbeck et al. (1997) found a value of $5 \times 10^6\ cm^2\ s^{-1}$ to be representative for the frontal region in their study — a maximum value of 10 $cm\ s^{-1}$ is obtained for the horizontal components of the bolus velocity when the vertical derivative of isopycnal slopes equals the prescribed maximum value.

A baroclinic time step of 1800 s has been used for all model runs presented in this paper. In this case, the eddy transfer coefficient fields need not be updated during every baroclinic time step. The updating frequency must be dependent on the growth rate (T^{-1}) field dynamics (Visbeck et al., 1997). We have chosen a simplified approach, whereby the updating takes place after a prescribed number of baroclinic time steps. For a baroclinic time step of 1800 s, this has been set equal to 24, which means that the eddy transfer coefficient is calculated and updated every 12 hours. The CPU cost associated with this procedure is negligible.

The minimum value of the eddy coefficient has been set equal to $5 \times 10^5\ cm^2\ s^{-1}$, which is much smaller than the minimum value of $3 \times 10^6\ cm^2\ s^{-1}$ chosen by Wright (1997) to remove noise in his simulations with one of the Hadley Centre's ocean models. We chose a smaller value in order to let the eddy transfer coefficient vary towards low values and thus enlarge its range. We also employed a low background horizontal diffusion to help remove noise in the tracer fields.

2.3 Model

SPOM (Sub-Polar Ocean Model) is a regional configuration of the Modular Ocean Model - Array (MOMA) set up specifically for process and sensitivity studies of ocean variability questions in the subpolar North Atlantic. The original model formulation is based on a Bryan-Cox-Semtner type ocean general circulation model using the inviscid version of the Killworth et al. (1991) free surface scheme. The model is briefly described in the following. The reader will find more details in Myers (2002).

The model has a non-isotropic horizontal resolution of $1/3° \times 1/3°$, and its computational domain covers the region of the North Atlantic from $38°N$ to $70°N$. At a given latitude, the grid spacing in the zonal direction equals that at the Equator (that corresponds to $1/3°$) multiplied by cosine of that latitude. The meridional grid spacing remains constant over the grid. The model has 36 levels, unevenly spaced in the vertical, with greater resolution in the upper water column. The topography was taken from the $1/12°$ ETOPO5 (NOAA, 1988) data set, and then linearly interpolated to the model's resolution. Actual depths are used with the model's incorporation of a partial cell formulation (other than ensuring no partially filled level has less than 10 m of water in it).

The standard settings for our first control run specify a biharmonic horizontal viscosity coefficient $A_h = 7.5 \times 10^{18}\ cm^4\ s^{-1}$, and a biharmonic horizontal diffusion coefficient $K_h = 7.5 \times 10^{18}\ cm^4\ s^{-1}$. The vertical viscosity coefficient is $A_v = 1.5\ cm^2\ s^{-1}$ and the vertical diffusion coefficient is $K_v = 0.3\ cm^2\ s^{-1}$. The constant value of the eddy transfer coefficient used by the GM scheme is $2.0 \times 10^5\ cm^2\ s^{-1}$.

Convective adjustment is performed using the complete convection scheme of Rahmstorf (1993). A momentum flux given by a quadratic friction law is applied at the bottom. Currently, SPOM does not incorporate a bottom boundary layer (BBL) parameterization such as that of Beckmann and Döscher (1997), which was found to improve significantly the downslope flow of the overflow waters in the North Atlantic.

The southern boundary is open, while restoring buffer zones are included along the model's closed northern boundaries. The open boundary formulation is based on the formulation of Stevens (1991), modified with a flow relaxation scheme that restores the sea surface height to a reference state (based on calculations from the diagnostic model of Myers and Weaver (1995)). Data along the southern boundary is taken from Grey and Haines (1999). More details on the open boundary condition can be found in Myers (2002).

Monthly-mean climatological forcing for both the tracers and the winds is applied at the surface. The surface temperature and salinity are relaxed to monthly mean data taken from the NODC (1994) data atlas, with a hard restoring timescale of 2 hours. As discussed in Myers (2002), this choice is made to fix the potential water formation regions while leaving the basin interior free to evolve. This restoring boundary condition also constrains the properties of the newly formed waters. Surface momentum fluxes are provided by the monthly climatology of Trenberth et al. (1990), averaged over the period 1980 – 1986. The model initial conditions are taken from the NODC (1994) data set, linearly interpolated to the model grid and depth levels.

2.4 Results and discussion

Results from experiments employing constant and variable eddy transfer coefficients are presented and discussed in this section. For each of them, the model has been started from rest and integrated over a period of 14 years. The constant values and value ranges for the tracer mixing parameters used in these experiments are given in Table 2.1.

Table 2.1: Experiments and values of tracer mixing coefficients. The value of the eddy transfer coefficient in $CONTROL_{AVG}$ is the spatial and temporal average of this coefficient calculated over the last 4 years of the integration in $SHEAR_\lambda$.

Experiment	Biharmonic horizontal diffusion coefficient (K_h) ($\times 10^{14}\ cm^4\ s^{-1}$)	Eddy transfer coefficient (k) ($\times 10^6\ cm^2\ s^{-1}$)
$CONTROL_S$	7.5×10^4	0.20
$CONTROL_{AVG}$	7.5	2.74
$STRAT_L$	7.5	0.5 – 10.0
$SHEAR_L$	7.5	0.5 – 10.0
$STRAT_\lambda$	7.5	0.5 – 10.0
$SHEAR_\lambda$	7.5	0.5 – 10.0

Although the following analysis covers the subpolar North Atlantic, the attention is focused on the Labrador Sea region, for which a more detailed comparison with observations and other model studies is provided. There are many similarities among the results obtained from the experiments with variable eddy transfer coefficients. Therefore, in many situations, only results from one of these will be compared to those from the two control experiments.

2.4.1 Energetics

Higher values of the domain-averaged instantaneous kinetic energy (not shown) reveal that the circulation is generally more energetic in the experiments with low horizontal diffusion. The only exception is $STRAT_\lambda$, where values similar to those from $CONTROL_S$ have been obtained. Values of the mean kinetic energy (MKE), kinetic energy of the mean flow (KEM), and eddy kinetic energy (EKE) per unit mass, for all of the experiments, are presented in Table 2.2. These energies are defined as follows,

$$KEM = \frac{1}{V}\int_V \frac{1}{2}\left(\overline{u}^2 + \overline{v}^2\right) dV, \tag{2.8}$$

$$EKE = \frac{1}{V}\int_V \frac{1}{2}\left(\overline{u'^2} + \overline{v'^2}\right) dV, \tag{2.9}$$

$$MKE = KEM + EKE, \tag{2.10}$$

where $\overline{u}$ and $\overline{v}$ are time-mean values of the velocity components u and v, respectively, with $u' = u - \overline{u}$ and $v' = v - \overline{v}$. The time-mean values, as with all of the time-mean fields presented henceforth, have been obtained as time averages over the last 4 years of integration (years 11-14).

Table 2.2: Domain- and time-averaged kinetic energies and eddy transfer coefficients (calculated over the last four years of integration), and maximum overturning streamfunction at $40°N$. Notation: KEM = kinetic energy of the mean flow; EKE = eddy kinetic energy; MKE = mean kinetic energy; k = eddy transfer coefficient; MOSF = maximum value of the meridional overturning streamfunction at $40°N$ calculated from the mean velocity field.

Experiment	KEM (cm^2s^{-2})	EKE (cm^2s^{-2})	MKE =KEM+EKE (cm^2s^{-2})	$\frac{EKE}{KEM}$	k ($\times 10^6$ cm^2s^{-1})	MOSF (Sv)
$CONTROL_S$	8.5	12.3	20.8	1.45	0.20	19
$CONTROL_{AVG}$	18.7	10.1	28.8	0.54	2.74	41
$STRAT_L$	17.5	7.0	24.5	0.40	2.26	34
$SHEAR_L$	17.7	9.9	27.6	0.56	1.44	36
$STRAT_\lambda$	15.1	4.9	20.0	0.32	3.67	34
$SHEAR_\lambda$	15.7	7.0	22.7	0.45	2.74	32

Although EKE is diminished in the experiments with variable eddy transfer coefficients, indicating a decreased variability of the flow, KEM is almost double that in $CONTROL_S$, and is thus responsible for larger values of MKE (Table 2.2). The

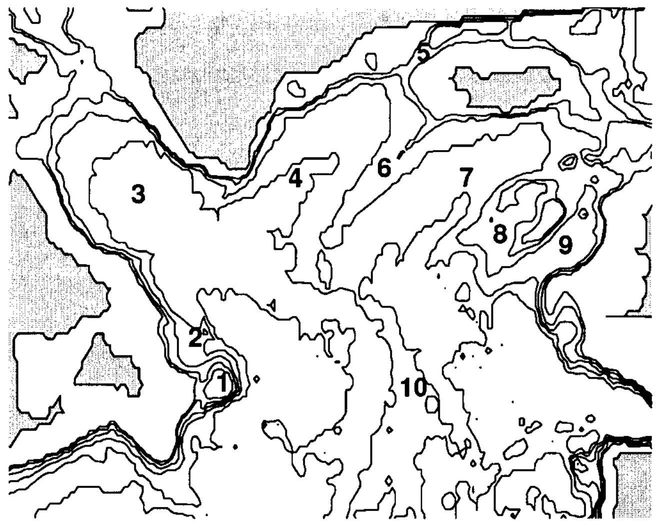

Figure 2.1: The main features of the bottom topography of the North Atlantic basin as they are represented in SPOM: 1 - Flemish Cap; 2 - Orphan Knoll; 3 - Labrador Basin; 4 - Irminger Basin; 5 - Denmark Strait; 6 - Reykjanes Ridge; 7 - Iceland Basin; 8 - Rockall Plateau; 9 - Rockall Trough; 10 - Mid-Atlantic Ridge. The bathymetry contour lines correspond to the following depths: 500 m, 1000 m, 2000 m, 3000 m and 4000 m.

enhanced release of available potential energy in regions where the eddy transfer coefficient takes high values (e.g. off Flemish Cap (Fig. 2.1), and the frontal region along the Labrador slope) reduces the level of baroclinic instability and is largely responsible for the significant reduction of the variability of the flow. For example, lower EKE values are obtained in these experiments along the pathway of the NAC, especially around Flemish Cap. In this region known for its high eddy variability, and baroclinic instability, the maximum EKE value drops from $\sim 700\ cm^2\ s^{-2}$ at $52\ m$ depth in $CONTROL_S$ to $\sim 500\ cm^2\ s^{-2}$ in $SHEAR_L$ and $\sim 420\ cm^2\ s^{-2}$ in $SHEAR_\lambda$. As discussed in Myers and Deacu (2004), which was based on an experiment similar to $CONTROL_S$, the higher EKE values in the partial cell model formulation were in better agreement with float-based observations. Thus, one of the improvements brought about by the more accurate representation of the bottom topography has been partly lost in $CONTROL_{AVG}$, and in the experiments with variable eddy transfer coefficients. This may be regarded as an undesirable side effect, since ocean modellers strive to obtain increased and thus more realistic mesoscale eddy activity. Nonetheless, this apparent shortcoming offers the possibility to increase the eddy variability through a reduction of the horizontal viscosity coefficient without compromising the model's numerical stability. Preliminary results from a simulation with a one order of magnitude lower biharmonic horizontal viscosity coefficient, namely $7.5 \times 10^{17}\ cm^4\ s^{-1}$, have shown that this is achievable, although we have not examined this experiment in detail.

The most energetic flow occurs in $CONTROL_{AVG}$. Its high KEM and low EKE/KEM regime signals a potential resemblance to the flows simulated in the the variable eddy transfer coefficient experiments. In some of the experiments, higher MKE values than that in $CONTROL_S$ may be noted, despite the horizontal and vertical viscosity coefficients remaining unchanged. This may be explained in part by the reduced viscous dissipation of momentum due to the reduced velocity shear characterizing the less variable flows in these experiments. It may also be related to the improved spreading of dense waters in the deep ocean, which acts to accelerate the meridional overturning circulation (see subsection on overflow waters). The relatively lower values of EKE, and EKE/KEM in $STRAT_\lambda$ and $SHEAR_\lambda$ mainly originate from the path of the NAC near Grand Banks and Flemish Cap. It is here that the eddy transfer coefficient takes larger values in these experiments compared to those in $STRAT_L$ and $SHEAR_L$.

An important result obtained in the experiments with variable eddy transfer coefficients is the increased eddy activity in the deep ocean, where eddy-permitting models usually fail to generate EKE values close to values estimated from observations (Smith et al., 2000). Sections of EKE at $48°N$ (Fig. 2.2) show that in both $CONTROL_S$ and $CONTROL_{AVG}$ the EKE values in the eastern basin are below 1 $cm^2\ s^{-2}$, whereas EKE intensifies at depth, reaching 5 $cm^2\ s^{-2}$ on the eastern flank of the Mid-Atlantic Ridge (MAR) in $SHEAR_L$, which compares very well with values estimated from moored current meters (Colin de Verdière et al., 1989), as well as with predictions provided by higher resolution models (Smith et al., 2000). Similar values have been obtained in $STRAT_L$ and $SHEAR_\lambda$, while values above 2 $cm^2\ s^{-2}$ appear in $STRAT_\lambda$.

The intensification of EKE in the deep ocean on the eastern flank of MAR visible in Fig. 2.2(c) is independent of the currents in the surface layer (i.e. NAC branches). It is generated by the topographically controlled and seasonally variable flow of dense water (Iceland Scotland Overflow Water) that crosses the Iceland-Scotland Ridge, which is better simulated in the experiments with variable eddy transfer coefficient (see, for example, Fig. 2.3). This can be readily seen in horizontal EKE sections (not shown) at depths greater than 3000 m, which show quite widespread eddy variability in the eastern basin, with local maxima around the Rockall Plateau and along the MAR.

2.4.2 Mean Circulation

Labrador Sea

The simulated Labrador Current (LC) branches at Hamilton Bank into an offshore branch that flows along the continental slope and an inshore branch flowing over the shelf. Contrary to observations, which indicate higher near-surface velocities for the offshore branch (estimated by Lazier and Wright (1993) to be twice as large as than those for the inshore branch, near $54°N$), in $CONTROL_S$ the offshore branch of the LC is not only weaker than the inshore branch but it also loses its strength as it flows along the slope (Fig. 2.4(a)). The relative strength of the LC branches is more realistically reproduced in the other experiments, with a stronger offshore branch all the way to Flemish Cap (Fig. 2.4(b)-2.4(f)). A deep reaching Labrador Current is visible in the vertical sections of the mean meridional velocity at $53°N$ shown in Fig. 2.5. Its almost barotropic structure with speeds higher than 15 $cm\ s^{-1}$ in all experiments, except $CONTROL_S$, are in very good agreement with the observed structure of the deep LC and its average velocity of $15 \pm 3\ cm\ s^{-1}$ at $54°N$ estimated by Lazier and Wright (1993), as well as with the mean value of 18 $cm\ s^{-1}$ estimated by Fischer and Schott (2002) for the core speed from float

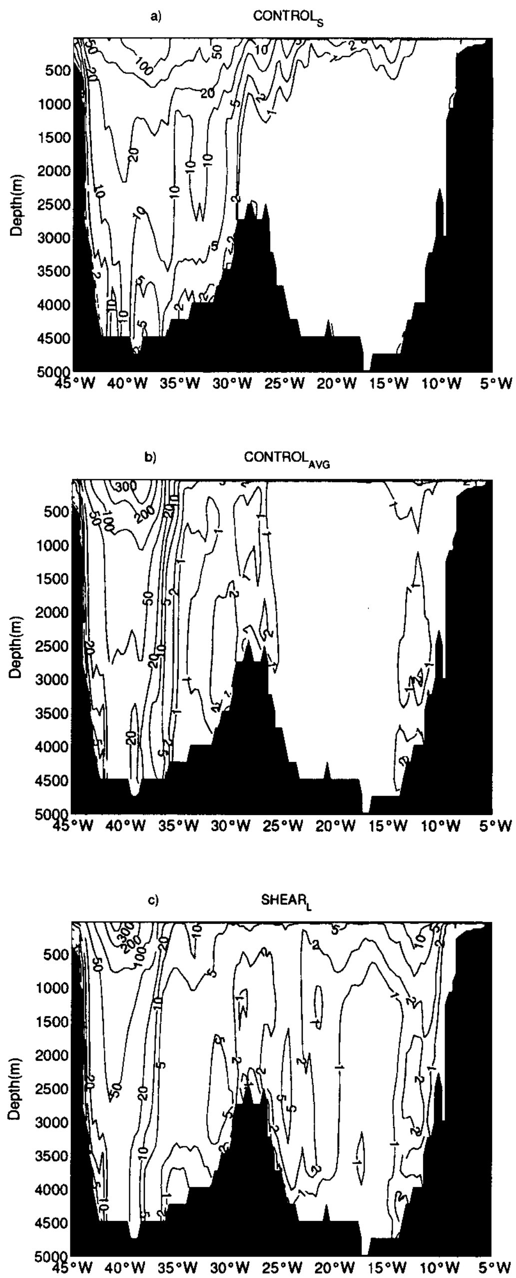

Figure 2.2: Eddy kinetic energy (in $cm^2\ s^{-2}$) at 48°N in $CONTROL_S$ (a), $CONTROL_{AVG}$ (b), and $SHEAR_L$ (c).

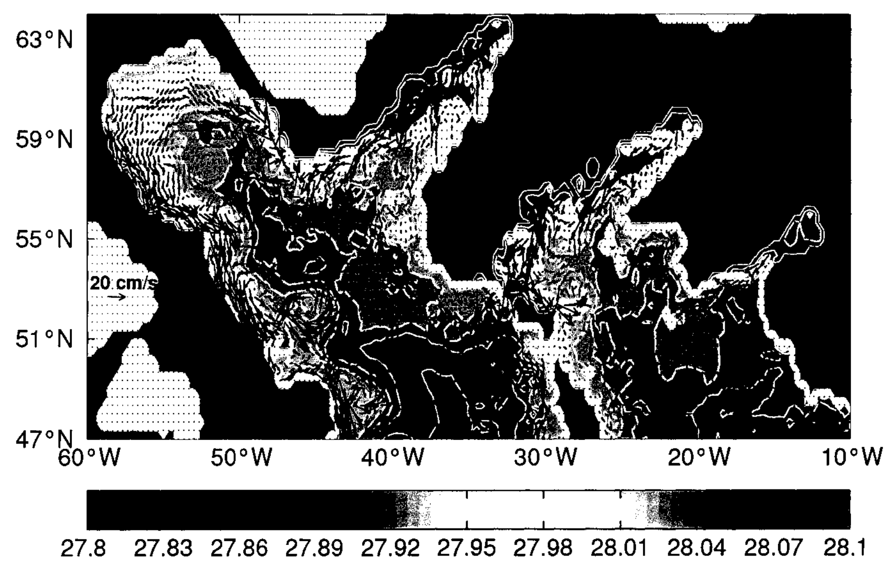

Figure 2.3: Potential density (σ_0) at 2980 m depth for model day 5040 (in June, year 14) in $SHEAR_\lambda$. The contour interval is 0.03. Superimposed are the horizontal velocity vectors at the same depth and time.

data.

A countercurrent similar to the current opposite and adjacent to the cyclonic boundary currents in the Labrador and Irminger seas recently revealed by observations (Lavender et al., 2000; Cuny et al., 2002; Fischer and Schott, 2002) first occurred in simulations with SPOM when a partial cell approach was used for the bottom-most cell (Myers, 2002). There are several quasi-stationary cyclonic eddies on the inshore flank of the countercurrent simulated with SPOM, which act as recirculating cells and thus resemble those reported by Lavender et al. (2000). Since the energy analysis performed on the model output by Myers and Deacu (2004) indicated transfer of EKE into KEM in the Labrador Sea region, the authors argued that baroclinic eddies occurring due to baroclinic instability in the frontal region along the Labrador continental slope may be responsible for the acceleration of the countercurrent, producing such a current in the model that is too intense compared to the observations.

These eddies may be too energetic in the previous version of the model (i.e. in $CONTROL_S$), as a high level of available potential energy may need be accumulated in the frontal region before the shedding of an eddy at the scale of the resolved flow is possible. One would expect that an increased release of available potential energy in the region by means of higher values of the bolus velocity would have a positive impact on the simulated countercurrent and circulation in the Labrador Sea. Lower levels of available potential energy have been obtained in $CONTROL_{AVG}$ and in the $STRAT$ and $SHEAR$ experiments, in which the values of the eddy transfer coefficient in the frontal region are at least one order of magnitude higher than in $CONTROL_S$, but this led to a weaker countercurrent in $STRAT_L$ and $SHEAR_L$ only (Fig. 2.5). However, a notable aspect is the reduced strength of the countercurrent relative to that of the LC in all experiments, except $CONTROL_S$, which is an a better agreement with the pattern obtained from observations (Lavender et al., 2000; Cuny et al., 2002; Fischer and Schott, 2002). Velocities between 5 $cm\ s^{-1}$ and 10 $cm\ s^{-1}$ have been obtained for the countercurrent in the Labrador

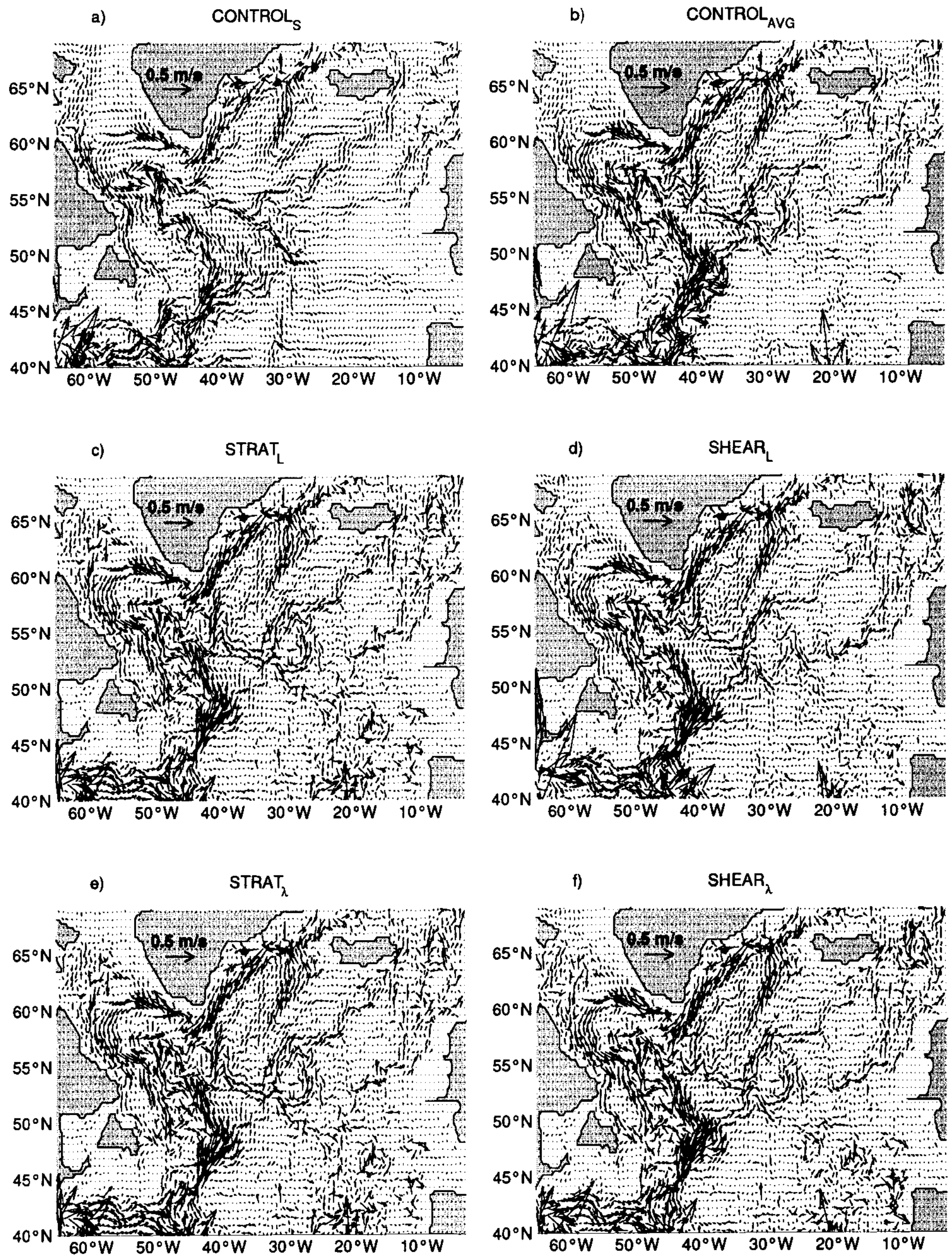

Figure 2.4: Time-mean horizontal velocity at 52 m depth in $CONTROL_S$ (a), $CONTROL_{AVG}$ (b), $STRAT_L$ (c), $SHEAR_L$ (d), $STRAT_\lambda$ (e), $SHEAR_\lambda$ (f). Vectors are plotted at every other grid point.

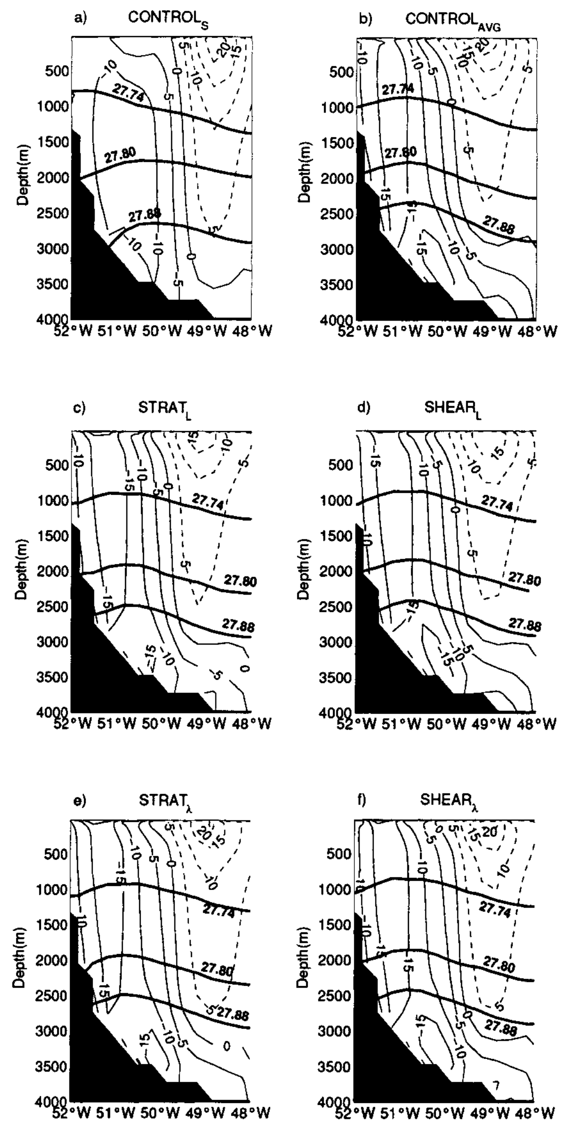

Figure 2.5: Cross-sections of the mean meridional flow and potential density σ_0 at $53°N$ in $CONTROL_S$ (a), $CONTROL_{AVG}$ (b), $STRAT_L$ (c), $SHEAR_L$ (d), $STRAT_\lambda$ (e), $SHEAR_\lambda$ (f). The thin continuous and dashed lines are isotachs ($cm\ s^{-1}$), whereas the thick lines depict potential density. Positive and negative values of velocity indicate northward and southward flow, respectively. The 27.74 and 27.80 isopycnals are the limits for the Labrador Sea Water. The Iceland Scotland Overflow Water layer is limited by the 27.80 and 27.88 isopycnals, and overlies the Denmark Strait Overflow Water layer.

Sea Water (LSW) layer, at $53°N$, in all experiments (Fig. 2.5), and these are close to the values measured by Fischer and Schott (2002).

A distinct feature visible in the experiments with reduced horizontal diffusion is the deep core of the Deep Western Boundary Current (DWBC), whose axis lies above the 3500 m isobath at $53°N$ (Fig. 2.5(b)- Fig. 2.5(f)). Its location and velocity values ($> 15\ cm\ s^{-1}$) at this latitude are consistent with those indicated by Fischer and Schott (2002) (see their Fig. 4b). The current is indistinguishable from the deep Labrador Current in $CONTROL_S$ (Fig. 2.5(a)). The DWBC is a major component of the large-scale meridional overturning circulation. Its realistic simulation, crucial for coupled climate modelling, requires accurate representation of the overflow waters that form the North Atlantic Deep Water carried by this current (Willebrand et al., 2001). Eddy-permitting z-level ocean models have difficulties in this respect, and bottom boundary layer schemes (Beckmann and Döscher, 1997) have been devised to address this issue. An explanation of the improved simulation of the DWBC in our experiments with reduced horizontal diffusion is given in the overflow waters section.

The North Atlantic Current and Eastern Basin

The mean near-surface current pattern obtained in all experiments (Fig. 2.4) shows the North Atlantic Current (NAC) as a relatively narrow current east of the Grand Banks (approx. $45°N$ and $43°W$), which branches near $46°N$. There is a branch that flows northeastwards and then crosses the Mid-Atlantic Ridge, which is visibly wider in $CONTROL_S$, most likely because of increased eddy activity in the region in this experiment. In the other experiments, this branch stays closer to the inshore branch before turning northeastwards at about $50°N$.

A narrower but strong branch flows past Flemish Cap and then northwestwards into the Labrador Sea. The latter fails to follow its classical path with an eastward turning in the region known as the "Northwest Corner" at $52°N$ (Krauss, 1986; Lavender et al., 2000). Instead, it continues into the Labrador Sea, associated with the countercurrent discussed above. The countercurrent is still too intense in all of the experiments, and this has a major negative impact on the strength and pathway of the simulated NAC, by entraining much of its water into the Labrador Sea and thus affecting the eastward shift of NAC at the "Northwest Corner".

One of the remarkable differences in the near-surface circulation in the eastern basin consists of the flow pattern around the Reykjanes Ridge. An anticyclonic flow around the ridge is obtained in $CONTROL_S$, whose southwestward component on the eastern flank originates from the NAC branch in the Iceland Basin (Fig. 2.4(a)). In the experiments with reduced horizontal diffusion this component is very weak relative to the intense northeastward current on the western flank of the ridge (the Irminger Current) and the branch of the NAC flowing in the Iceland basin (Fig. 2.4(b)- 2.4(f)). This is in better agreement with the pattern of the average surface circulation derived from drifter data by Flatau et al. (2003). In none of the experiments, however, does the Irminger Current show up as a branch of the NAC as in Flatau et al. (2003). The presence of the relatively strong southwestward current in $CONTROL_S$ leads a higher entrainment and recirculation of NAC water in the subpolar gyre, whereas most of this water appears to be carried across the Iceland-Scotland Ridge into the Norwegian Basin in the other experiments.

Another interesting feature of the upper-layer circulation in the eastern basin is the branch of NAC that flows around the Rockall Plateau into the Rockall Trough, which follows more closely the topography in the experiments with reduced horizontal diffusion. Observational data support the association of this branch with the local topography (Flatau et al., 2003). The current appears to be strongly influenced by the flow of the model's ISOW through the Rockall Trough. The steepening of the isopycnals occurring as this water flows against the southeastern slope of the Rockall Plateau may lead to the generation of this current as a quasi-geostrophic current, which thus bears some resemblance to the countercurrent in the Labrador Sea.

2.4.3 Overflow waters

The step-like topography of the z-level ocean models induces significant spurious vertical mixing of the overflow waters during their downslope spreading (Beckmann and Döscher, 1997). The use of partially filled bottom cells reduces this unwanted effect and enhances the propagation of the overflow plume by reducing the height of the step between adjacent bottom-most cells (Käse et al., 2001). On the other hand, Ezer and Mellor (2004) have shown that this spurious vertical mixing intensifies with increased horizontal diffusion in z-models, and concluded that the replacement of the horizontal diffusion with an isopycnal diffusion scheme might lead to an improved simulation of the downslope spreading of the overflow waters. Results from our experiments that employ the GM scheme and have a low background horizontal diffusion support this. Thus, the more stratified and clearly identifiable DWBC obtained in these experiments is nothing else but the product of a better representation of the model's overflow waters (DSOW and ISOW) leading to an improved capability to maintain their water mass properties as they flow against the Greenland and Labrador continental slopes (Fig. 2.6).

Figure 2.5 shows that the 27.80 isopycnal that caps the overflow water mass in our model remains at about the same depth along the Labrador slope, in all experiments. However, the ISOW layer (bounded by the 27.80 and 27.88 isopycnals) is thicker in $CONTROL_S$ (Fig. 2.5(a)) than in the other experiments (Fig. 2.5(b)-2.5(f)), whereas the DSOW layer (beneath the 27.88 isopycnal) is thinner. The continuous transformation of the water mass properties of the DSOW along its path through spurious mixing with ambient water is considered to be a principal mechanism whereby this water becomes lighter and thus contributes to the thickness of the ISOW layer in $CONTROL_S$. This also explains why the density-driven DWBC is weaker and hardly distinguishable from the deep LC in the same experiment. A very similar situation has been reported by Ezer and Mellor (2004) for an idealized case, in which a thicker intermediate water mass resulted from a decreased downslope spreading of their dense plume combined with enhanced spurious mixing of

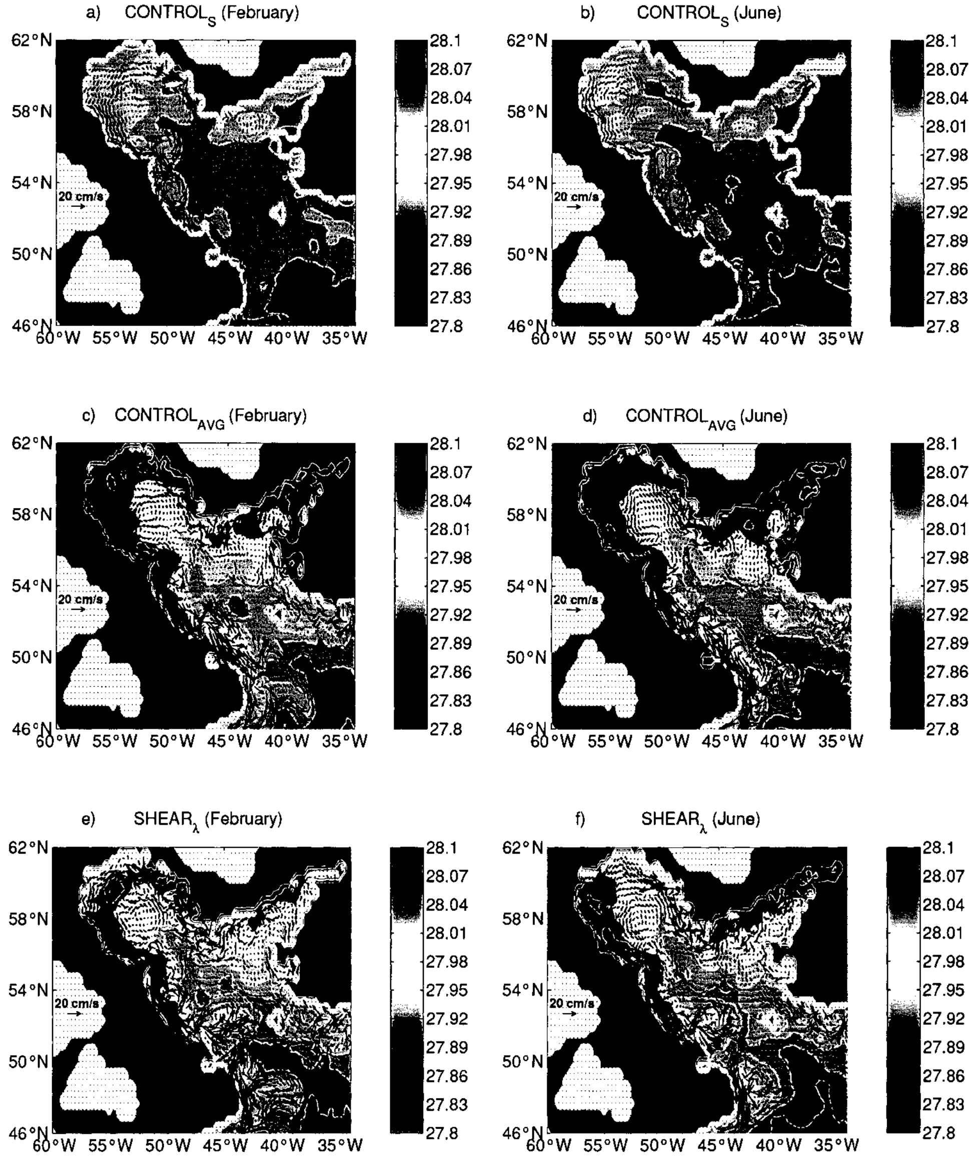

Figure 2.6: Potential density (σ_0) at 3225 m depth for model days 4920 (in February, year 14) and 5040 (in June, year 14) in $CONTROL_S$ (a, b), $CONTROL_{AVG}$ (c, d), and $SHEAR_\lambda$ (e, f). The contour interval is 0.03. Superimposed are the horizontal velocity vectors at the same depth and time.

the dense water with ambient water as the horizontal diffusion was increased in their experiments with a z-level model.

Another aspect that fits in this context is that of the link between the numerical stability of SPOM and the representation of the overflow waters. It is very likely that the reduced vertical mixing due to convective adjustment triggered by statically unstable regions at the bottom, which occurs when dense water overlies lighter water, may have had a positive impact on the numerical stability. This effect, first noticed and reported by Mellor et al. (2002) and Ezer and Mellor (2004), may partly explain why SPOM remained numerically stable despite the significant reduction in horizontal diffusion.

The two quasi-stationary cyclonic eddies visible at all levels near $52°N$ and $56°N$ (offshore of the Labrador continental slope) have a major impact on the circulation simulated with SPOM in all experiments by controlling the intensity of the countercurrent (Fig. 2.4 and Fig. 2.6). Initially, they were thought to be generated entirely through baroclinic instability in the frontal region. Therefore, they were expected to become less energetic as a result of increased release of available potential energy in experiments that used higher values for eddy transfer coefficient in the region, and this was one of the motivations of the study presented herein. However, the expected behaviour seems to have occurred to some extent in $STRAT_L$ and $SHEAR_L$ only. Further investigation took into consideration the DWBC and revealed that its interaction with topography is associated with the above mentioned eddies. Thus, the eddy near $56°N$ appears to be related to the doming of isopycnals produced by the accumulation of dense water where the DWBC abruptly changes its direction, northeast of Hamilton Bank (Fig. 2.6). The other eddy is generated where the DWBC is deflected seawards by the Orphan Knoll (Fig. 2.6 and Fig. 2.3); similar cyclonic circulation in this region has been identified observationally (Fischer and Schott, 2002; Lavender et al., 2000). There are also transient eddies that occur along the pathway of the DWBC (along the Labrador continental slope and offshore Flemish Cap) in all experiments (Fig. 2.6), but only an in-depth investigation can tell us whether they are due to shear instability or baroclinic instability.

A remarkable improvement relative to $CONTROL_S$ is the simulation of the flow of dense water (ISOW) originating from the Norwegian Sea in all the other experiments. Most of this water flows along the eastern slope of the Reykjanes Ridge, and then part of it flows around the ridge to enter the Irminger Basin, while the rest continues its path along the eastern flank of MAR. Figure 2.3 shows the interaction of this flow with a topographic feature near $52°N$ and $31°W$, which is a coarse representation of the Recate Seamount in the model on the south side of the CGFZ. The density-driven current is deflected by this feature and a cyclonic recirculation centred near $52.5°N$ and $28°W$ (Fig. 2.4(b)-2.4(f)) occurs. The quasi-stationary eddy generated here resembles that identified from observations by Bower et al. (2002), although it is located about 2 degrees east of this one. Notice, however, that the location of the simulated eddy is sensitive to the grid resolution as well as to the representation of the topography. There is also flow of ISOW along the southeastern and southwestern slopes of the Rockall Plateau.

As mentioned previously, the improved representation of the dense overflow waters (DSOW and ISOW) in the model, in the experiments with reduced horizontal diffusion, has led to the simulation of a stronger and more clearly identifiable DWBC. Consequently, one would expect an increased southward transport of the meridional overturning circulation (MOC). Figure 2.7 depicts the meridional overturning streamfunction calculated from the mean meridional velocity field averaged over the last four years of the integration. In both $CONTROL_{AVG}$ and $SHEAR_\lambda$, the overturning circulation is stronger than in $CONTROL_S$. The overturning transport at $40°N$ is 19 Sv in $CONTROL_S$, 41 Sv in $CONTROL_{AVG}$, and 32 Sv in $SHEAR_\lambda$ (the values for all of the experiments are given in Table 2.2). The strength of the meridional overturning circulation in the North Atlantic obtained in $CONTROL_S$ is in better agreement with the observational estimates, which are less than 20 Sv (Ganachaud and Wunsch (2000)). The unrealistically high values obtained in the rest of the experiments are the result of the generally larger mean meridional velocities used in the calculations. The latter are not brought about by an unreasonably high production and transport of North Atlantic Deep Water (LSW, ISOW, and DSOW), but rather by the occurrence of more energetic mean flows due to reduced velocity shear in those experiments.

It should be noted that, in all of the experiments with reduced horizontal diffusion, the returning southward component of meridional overturning circulation is more concentrated towards the bottom (Fig. 2.7). This downward shift is somewhat similar to that obtained by Dengg et al. (1999), when a BBL scheme was used to facilitate the flow of the dense waters in an eddy-permitting model of the subpolar North Atlantic, while preserving its properties. However, the overturning transport exhibited changes of only 1 Sv in their experiments. Significant sensitivity of the Atlantic MOC to the overflow waters originating from the Nordic Seas was found in modelling studies carried out by Döscher et al. (1994) and Döscher and Redler (1997).

2.4.4 Salinity

In order to assess the effect of the variable eddy transfer coefficients on the freshwater content of the Labrador Sea, this quantity has been calculated for the Labrador Sea region between latitudes $52°N$ and $64°N$ (shown in Fig. 2.8), every 3 months, and through the entire period of integration. The formula used for freshwater content is

$$FW = \int_V \frac{S_r - S}{S_r} dV, \tag{2.11}$$

where V is the volume of the domain under consideration, S is the model output salinity, and S_r is a reference salinity (with a value of $35.0\,psu$, chosen to be consistent with the model salinity in $CONTROL_S$ at the offshore edge of the Labrador Current, see Myers (2002) for more details). Figure 2.8 shows that there are no major differences in the freshwater content time series obtained in the experiments with variable eddy transfer coefficients. They all have seasonal variations characterized with smaller amplitudes and higher annual mean values relative to the two

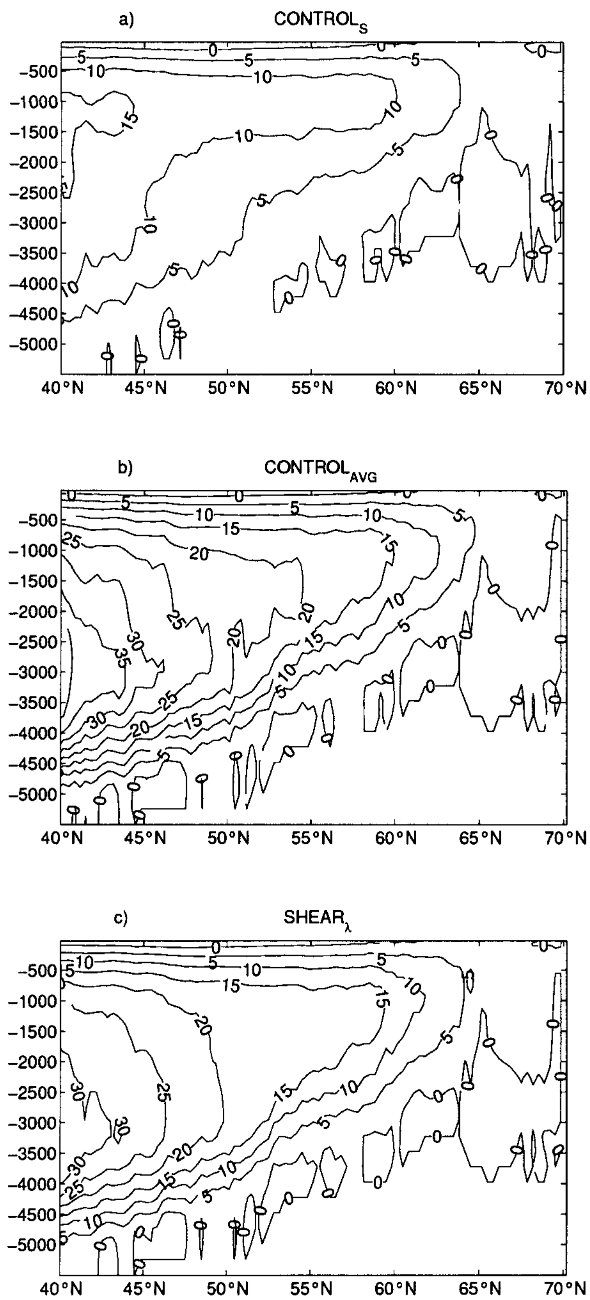

Figure 2.7: Meridional overturning streamfunction for the subpolar North Atlantic (in Sv) in $CONTROL_S$ (a), $CONTROL_{AVG}$ (b), and $SHEAR_\lambda$ (c). The contour interval is 5 Sv.

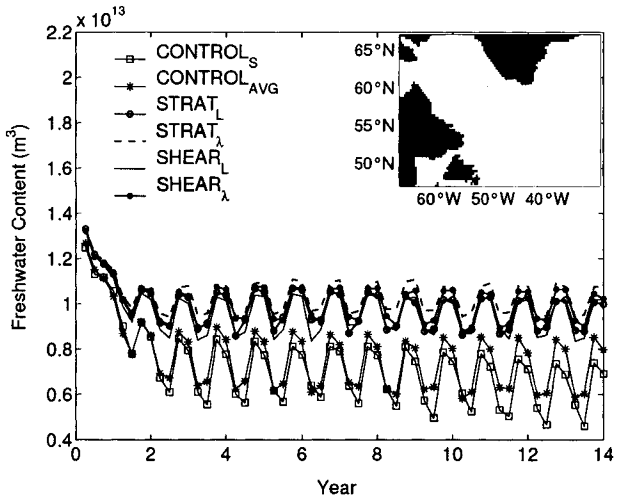

Figure 2.8: Freshwater content for a limited region in the Labrador Sea (the gray-shaded region in the upper-right corner of the figure)

$CONTROL$ experiments. An improvement in these simulations consists in the diminished loss of freshwater indicated by the higher annual mean values obtained after the initial drift from the initial conditions has ceased. This is one of the few instances in which a clear distinction can be made between the results obtained from the experiments with variable eddy transfer coefficients and $CONTROL_{AVG}$, and it shows that small local differences can lead to dissimilar global effects. A seasonal equilibrium has also been reached in all experiments other than $CONTROL_S$.

Although the 14-year period of integration is insufficient for the model to reach a thermodynamical equilibrium, some qualitative comparisons involving the salinity fields evolved from the initial conditions can be made. The time-mean salinity has been plotted on the $\sigma_2 = 36.95$ isopycnal surface, which is representative for the LSW, to offer a rather qualitative view of the spreading of this water in three different experiments (Fig. 2.9). Salinity is overpredicted in the Labrador Sea in all experiments, since the observed salinity values associated with the LSW are typically less than 34.9 psu (Lilly et al., 1999). This is a typical problem in non-eddy-resolving models of the North Atlantic. A reduction in salinities in the Labrador and Irminger basins is obtained in $CONTROL_{AVG}$ (Fig. 2.9(b)). Further reductions occur in the experiments with variable eddy transfer coefficients (Fig. 2.9(c)), which are the closest to the observations. These changes on this isopycnal surface are brought about by a shift in LSW formation from saltier to fresher water classes.

The LSW on the $\sigma_2 = 36.95$ isopycnal is associated with a minimum in salinity (Fig. 2.9). The plots obtained in $CONTROL_{AVG}$ and $SHEAR_\lambda$ (Fig. 2.9(b) and 2.9(c)) illustrate two main pathways of spreading of the LSW from the deep convection region (centred at about $58°N$ and $53°W$ in the model). One pathway is established through the spreading of LSW from the deep convection region towards the LC, followed by embedment in the LC and southward transport by this current, along with spreading towards the eastern North Atlantic basin along the pathway of the NAC. Notice that the MAR acts as a barrier to the spreading of the LSW into the eastern basin along this isopycnal due to its high depth in the model. The other pathway is from the deep convection region to the Irminger Sea. It occurs as a result of entrainment of LSW into the countercurrent simulated in the Labrador Sea, that reaches into the Irminger Sea. Interestingly, part of the water following this path is LSW recirculated by the countercurrent along the Labrador slope.

Salinity sections at $53°N$ (Fig. 2.10) show that an improved representation of the LSW (visible as the tongue of relatively homogeneous low salinity water centred at 2000 m depth in Fig. 2.10(b) and 2.10(c)) and its seaward spreading is obtained in $CONTROL_{AVG}$ and $SHEAR_\lambda$. Similar results have been obtained in the other experiments with variable eddy transfer coefficients. Consistent with the freshwater content analysis (Fig. 2.8), the LSW core salinity is lower in $SHEAR_\lambda$.

2.4.5 GM velocities

Instantaneous horizontal bolus velocity fields obtained in the $SHEAR_L$ experiment have been plotted every 30 days over the period February-July of the last year of integration, on level 20 of the model ($\sim$ 1500 m depth). These fields are depicted in Fig. 2.11. The plot for model day 4920 (February) shows that high magnitudes for this quantity are concentrated in the region of the Labrador Sea where

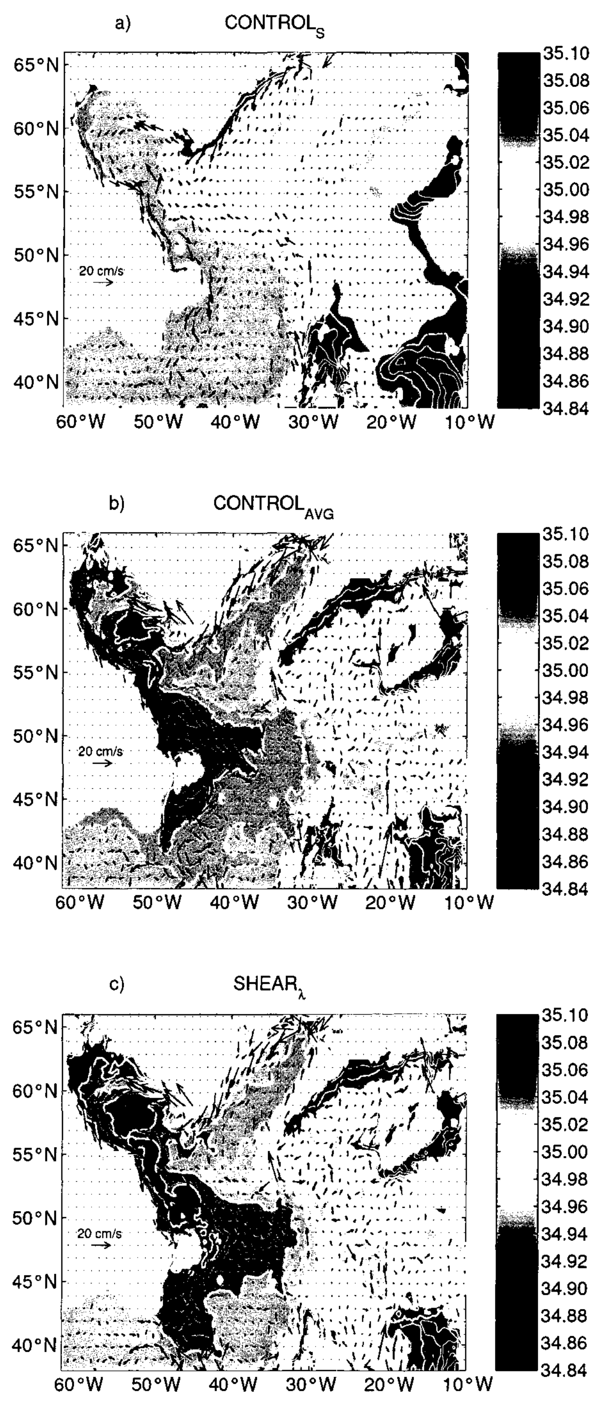

Figure 2.9: Time-mean salinity (in psu) on the $\sigma_2 = 36.95$ isopycnal in $CONTROL_S$ (a), $CONTROL_{AVG}$ (b), and $SHEAR_\lambda$ (c). The contour interval is 0.02. Superimposed are vectors of the mean horizontal velocity (plotted at every other grid point) on the same isopycnal surface.

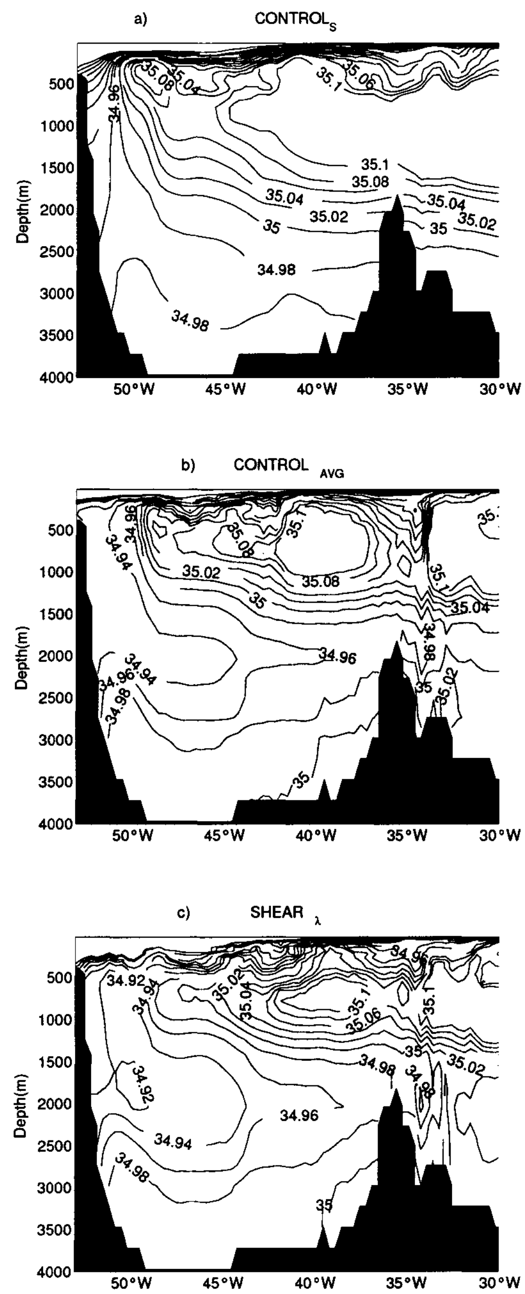

Figure 2.10: Time-mean salinity (in psu) at $53°N$ in $CONTROL_S$ (a), $CONTROL_{AVG}$ (b), and $SHEAR_\lambda$ (c). The tongue of low salinity centred at 2000 m depth, which is visible on the right-hand side of (b) and (c), corresponds to the model's Labrador Sea Water. Only contours for salinity values between 34.8 and 35.1 psu have been plotted. The contour interval is 0.02.

the simulated deep convection occurs at this time of the year, as well as along the northeastern part of the East Greenland slope, on the path of the Denmark Strait Overflow Water (DSOW). The bolus velocity in the deep convection region induces an outflow at depths between approximately 700 m and 2300 m that carries LSW towards the shore where it gets embedded into the southward flowing boundary currents, as well as towards the countercurrent leading to direct LSW export to the Irminger Sea (Fig. 2.11(b) and 2.11(c)). This is matched by an inflow at shallower depths, advecting lighter water towards the interior of the gyre. This circulation is similar to the eddy-induced "overturning circulation" in the deep convection region of the Labrador Sea proposed by Khatiwala and Visbeck (2000). The plots of the eddy-induced velocity for the next three months indicate a post-convection spreading towards the boundary, which is associated with slumping of steep isopycnals. This process leads to a large decrease in baroclinic activity in the region as a consequence of the restratification of the water mass. An eddy-induced flow is visible in the frontal region of the Labrador Current, in the plots for June and July. The steepening of the isopycnals that occurs as the Labrador Current is transporting LSW southwards leads to the intensification of the eddy-induced flow. This suggests a timescale of 4-5 months for the LSW to reach Flemish Cap from the deep convection region. Plots of the potential density (not shown) on level 15 show that the LSW spreading towards the LC followed by its southward transport is simulated in the experiments with reduced horizontal diffusion only. Notice also the intensification in time of the eddy-induced flow along the East Greenland slope as well as on the western side of the Reykjanes Ridge. This flow is generated by the steepening of isopycnals caused by the seasonally variable flow of ISOW and DSOW at depth.

2.5 Conclusions

A variable eddy transfer coefficient for the GM parameterization has been tested in a $1/3°$-resolution ocean model of the subpolar North Atlantic. The aim of the study is to assess the impact of the quasi-adiabatic transport/stirring of tracers by

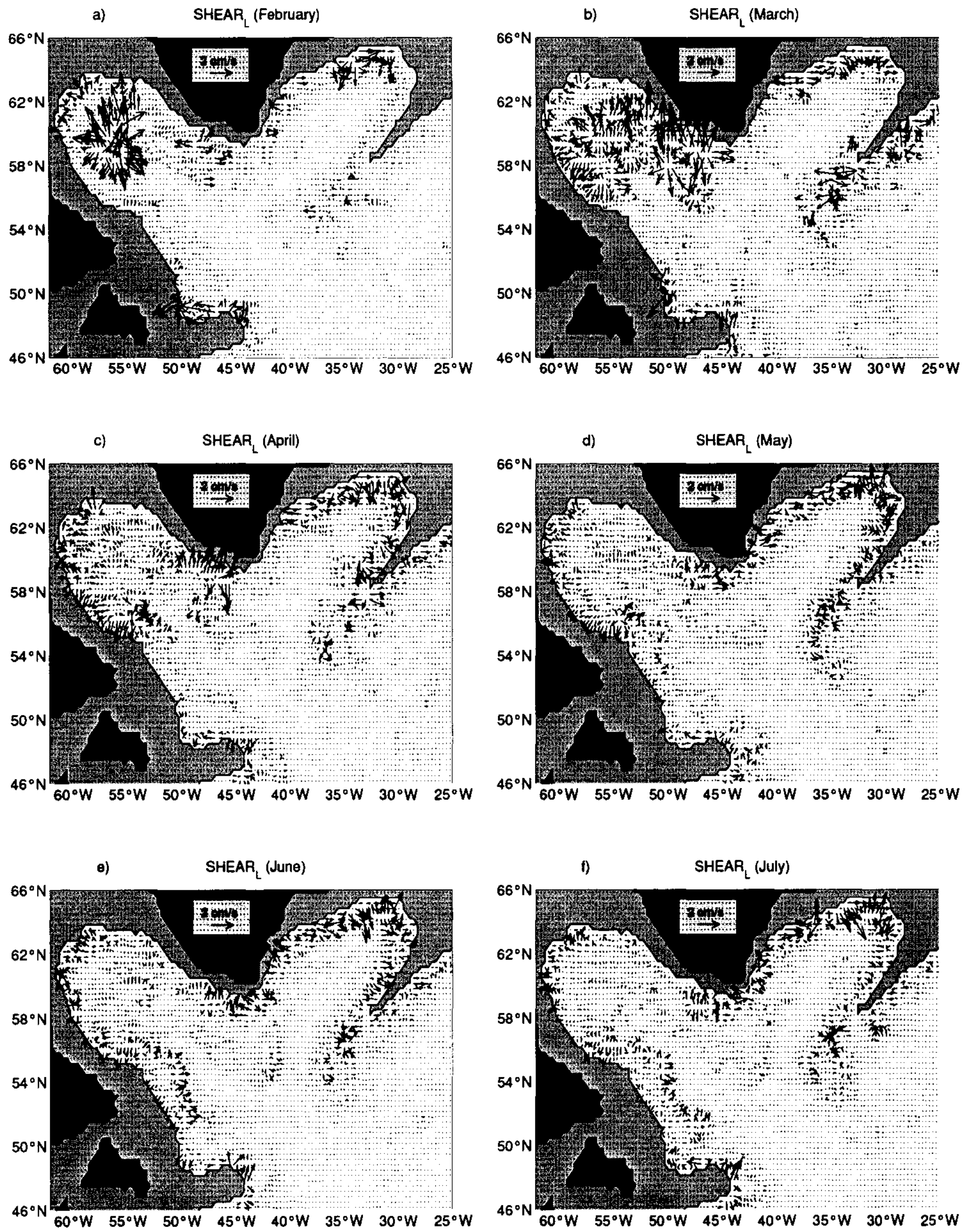

Figure 2.11: GM/bolus/eddy-induced velocity vector fields obtained in the $SHEAR_L$ experiment on level 20 ($\sim$ 1500 m) for the model days (a) 4920 (February), (b) 4950 (March), (c) 4980 (April), (d) 5010 (May), (e) 5040 (June), (f) 5070 (July) of the 14^{th} year of integration from rest.

means of eddy-induced velocities that use either variable or constant eddy transfer coefficients and a low level of explicit horizontal diffusion, in the eddy-permitting regime.

Two formulae have been employed for the computation of the eddy transfer coefficient field, each of them implemented in two different ways. Results from the four experiments corresponding to the four formula-implementation pairs have been compared with results from two control experiments. In both control experiments, the eddy-induced velocities are calculated using a constant eddy transfer coefficient. The one that uses a lower value for this coefficient also uses a typical value of the biharmonic horizontal diffusion coefficient for the eddy-permitting regime. The second control experiment employs a larger eddy transfer coefficient and a significantly lower horizontal diffusion coefficient.

More realistic and quite similar simulations have been obtained in all of the experiments with a low level of horizontal diffusion, i.e. in the experiments with variable eddy transfer coefficients and in the control experiment with a higher value of this coefficient. Therefore, we conclude that the reduction of the spurious diapycnal mixing obtained in these experiments has a primary positive impact on the circulation and hydrography, whereas the use of a variable eddy transfer coefficient has a secondary importance. Nonetheless, aside from its physically motivated use, there are instances of better predictions for global quantities (e.g. overturning transport, freshwater content of the Labrador Sea) that indicate that a variable eddy transfer coefficient is preferable.

Many of the improvements obtained in the experiments with reduced horizontal diffusion are brought about by a better representation of the overflow waters originating from the Nordic Seas. Among these are a more realistic Deep Western Boundary Current and an increased eddy activity in the deep ocean in the eastern North Atlantic. In the same experiments, the higher values of the GM velocities combined with a reduced spurious diapycnal mixing in the deep convection region at the time the deep convection is occurring "help" the Labrador Sea Water spread from this region to the currents that surround it. Two classical pathways for the spreading of this water, one via the Labrador Current and the other via the countercurrent in the Labrador Sea, are then established.

The relative strength of the two branches of the Labrador Current and the almost barotropic structure of its offshore branch as well as the near-surface circulation in the eastern North Atlantic simulated in the experiments with low horizontal diffusion are in better agreement with flow patterns inferred from observations. A more energetic but less time-variable flow is obtained in the same experiments. The undesirable effect of reduced eddy activity in the upper layers is the result of the increased release of available potential energy.

A strong countercurrent occurs in the Labrador Sea, in all of the experiments. This has a negative impact on the pathway of the NAC in the "Northwest Corner", as well as on the hydrography of the Labrador Sea by entraining NAC water into the region. However, in the experiments with variable eddy transfer coefficients, the existence of a larger volume of LSW along the Labrador slope leads to an increased recirculation of this water mass and thus diminishes the model salinity drift in the Labrador Sea.

Since quite similar results have been obtained in all of the experiments with variable eddy transfer coefficients, none of the four formula-implementation pairs used for this coefficient stands out as the best. Note, however, that the eddy coefficient field was found to be more "dynamic" in the $SHEAR$ experiments than in the $STRAT$ experiments, in the sense that it changed more rapidly in time. Moreover, the same field had a smaller time- and domain-average value and led to higher EKE/KEM ratios, indicating increased variability of the flow. Tuning of the constants used in the expressions for the eddy transfer coefficient has not been tested, but it can provide a means of limiting the possible overparameterization of the effect of mesoscale eddies when using eddy-induced velocities with variable eddy transfer coefficients in eddy-permitting ocean models.

Bibliography

Adcroft, A., C. Hill, and J. Marshall, 1997: Representation of topography by shaved cells in a height coordinate ocean model. *Mon. Wea. Rev.*, **125**, 2293–2315.

Beckmann, A. and R. Döscher, 1997: A method for improved representation of dense water spreading over topography in geopotential-coordinate models. *J. Phys. Oceanogr.*, **27**, 581–591.

Beismann, J. O. and R. Redler, 2003: Model simulations of CFC uptake in North Atlantic Deep Water: Effects of parameterizations and grid resolution. *J. Geophys. Res.*, **108**, doi:10.1029/2001JC001253.

Böning, C. W., R. Holland, F. Bryan, G. Danabasoglu, and J. C. McWilliams, 1995: An overlooked problem in model simulations of the thermohaline circulation and heat transport in the Atlantic Ocean. *J.Climate*, **8**, 515–523.

Bower, A. S., B. Le Cann, T. Rossby, W. Zenk, J. Gould, K. Speer, P. L. Richardson, M. D. Prater, and H.-M. Zhang, 2002: Directly measured mid-depth circulation in the northeastern North Atlantic Ocean. *Nature*, **419**, 603–607.

Bryan, K., J. K. Dukowicz, and R. D. Smith, 1999: On the mixing coefficient in the parameterization of bolus velocity. *J. Phys. Oceanogr.*, **29**, 2442–2456.

Colin de Verdière, A., H. Mercier, and M. Arhan, 1989: Mesoscale variability from the western to the eastern Atlantic along 48°N. *J. Phys. Oceanogr.*, **19**, 1149–1170.

Cox, M. D., 1987: Isopycnal diffusion in a z-coordinate ocean model. *Ocean Modelling*, **74**, 1–5.

Cuny, J., P. B. Rhines, P. P. Niiler, and S. Bacon, 2002: Labrador Sea boundary currents and the fate of the Irminger Sea Water. *J. Phys. Oceanogr.*, **32**, 627–647.

Danabasoglu, G. and J. C. McWilliams, 1995: Sensitivity of the global ocean circulation to parameterizations of mesoscale tracer transports. *J.Climate*, **8**, 2967–2987.

Danabasoglu, G., J. C. McWilliams, and P. R. Gent, 1994: The role of mesoscale tracer transports in the global ocean circulation. *Science*, **264**, 1123–1126.

Dengg, J., C. Böning, U. Ernst, R. Redler, and A. Beckmann, 1999: Effects of an improved model representation of overflow water on the subpolar North Atlantic. *Int. WOCE Newsletter*, **37**, 10–14.

Döscher, R., C. W. Böning, and P. Herrmann, 1994: Response of circulation and heat transport in the North Atlantic to changes in thermohaline forcing in northern latitudes: A model study. *J. Phys. Oceanogr.*, **24**, 2306–2320.

Döscher, R. and R. Redler, 1997: The relative importance of northern overflow and subpolar deep convection for the North Atlantic thermohaline circulation. *J. Phys. Oceanogr.*, **27**, 1894–1902.

England, M. H. and G. Holloway, 1998: Simulations of CFC content and water mass age in the deep North Atlantic. *J. Geophys. Res.*, **103**, 15885–15901.

Ezer, T. and G. L. Mellor, 2004: A generalized coordinate ocean model and a comparison of the bottom boundary layer dynamics in terrain-following and in z-level grids. *Ocean Modelling*, **6**, 379–403.

Fischer, J. and F. A. Schott, 2002: Labrador Sea water tracked by profiling floats — from the boundary current into the open North Atlantic. *J. Phys. Oceanogr.*, **32**, 573–584.

Flatau, M. K., L. Talley, and P. P. Niiler, 2003: The North Atlantic Oscillation, surface current velocities, and SST changes in the subpolar North Atlantic. *J. Climate*, **16**, 2355–2369.

Ganachaud, A. and C. Wunsch, 2000: Improved estimates of global ocean circulation, heat transport and mixing from hydrographic data. *Nature*, **408**, 453–456.

Gent, P. R., F. Bryan, S. Doney, and W. Large, 1999: A perspective on the ocean component of climate models. *Exchanges*, **14**, 11–14.

Gent, P. R., A. P. Craig, C. M. Bitz, and J. W. Weatherly, 2002: Parameterization improvements in an eddy-permitting ocean model for climate. *J. Climate*, **15**, 1447–1459.

Gent, P. R. and J. C. McWilliams, 1990: Isopycnal mixing in ocean circulation models. *J. Phys. Oceanogr.*, **20**, 150–155.

Gent, P. R., J. Willebrand, T. McDougall, and J. C. McWilliams, 1995: Parameterizing eddy-induced tracer transports in ocean circulation models. *J. Phys. Oceanogr.*, **25**, 463–474.

Gerdes, R., C. Koberle, and J. Willebrand, 1991: The influence of numerical advection schemes on the results of ocean general circulation models. *Climate Dyn.*, **5**, 211–226.

Grey, S. M. and K. Haines, 1999: Climatological hydrography of the North Atlantic. *Int. WOCE Newsletter*, **36**, 23–25.

Haines, K. and P. Wu, 1998: GCM studies of intermediate and deep waters in the Mediterranean. *J. Mar. Syst.*, **18**, 197–214.

Held, I. M. and V. D. Larichev, 1996: A scaling theory for horizontally homogeneous, baroclinically unstable flow on a beta plane. *J. Atmos. Sci.*, **53**, 946–952.

Käse, R. H., A. Biastoch, and D. B. Stammer, 2001: On the mid-depth circulation in the Labrador and Irminger Seas. *Geophys. Res. Lett.*, **28**, 3433–3436.

Khatiwala, S. and M. Visbeck, 2000: An estimate of the eddy-induced circulation in the Labrador Sea. *Geophys. Res. Lett.*, **27**, 2277–2280.

Killworth, P. D., D. Staniforth, D. J. Webb, and S. M. Patterson, 1991: The development of a free-surface Bryan-Cox-Semtner ocean model. *J. Phys. Oceanogr.*, **21**, 1333–1348.

Krauss, W., 1986: The North Atlantic Current. *J. Geophys. Res.*, **91**, 5061–5074.

Lavender, K. L., R. E. Davis, and W. B. Owens, 2000: Mid-depth recirculation observed in the interior Labrador and Irminger Seas by direct velocity measurement. *Nature*, **407**, 66–69.

Lazier, J. R. N. and D. G. Wright, 1993: Annual velocity variations in the Labrador Current. *J. Phys. Oceanogr.*, **23**, 659–678.

Lilly, J. M., P. B. Rhines, M. Visbeck, R. Davis, J. R. N. Lazier, F. Schott, and D. Farmer, 1999: Observing deep convection in the Labrador Sea during winter 1994/1995. *J. Phys. Oceanogr.*, **29**, 2065–2098.

Maltrud, M. E. and J. L. McClean, 2005: An eddy resolving global $1/10°$ ocean simulation. *Ocean Modelling*, **8**, 31–54.

Mathieu, P. P., 1998: Parameterization of mesoscale turbulence in a world ocean model. Ph.D. thesis, Université catholique de Louvain, 203 pp. [Available from Institut d'Astronomie et de Géophysique G. Lemaitre, Univesité catholique de Louvain, Chemin du cyclotron 2, B-1348, Louvain-la-Neuve, Belgium.].

Mellor, G. L., S. Hakkinen, T. Ezer, and R. Patchen, 2002: *A generalization of a sigma coordinate ocean model and an intercomparison of model vertical grids.* Ocean Forecasting: Conceptual Basis and Applications, N. Pinardi and J. Woods, Eds.. Springer, New York, 55-72 pp.

Myers, P. G., 2002: SPOM: A regional model of the sub-polar North Atlantic. *Atmos.-Ocean*, **40**, 445–463.

Myers, P. G. and D. Deacu, 2004: Labrador Sea freshwater content in a model with a partial cell topographic representation. *Ocean Modelling*, **6**, 359–377.

Myers, P. G. and A. J. Weaver, 1995: A diagnostic barotropic finite-element ocean circulation model. *J. Atmos. Oceanic Technol.*, **12**, 511–526.

NOAA, 1988: Data announcement 88-MGG-02, Digital relief of the surface of the earth. Technical report, National Geophysical Data Center, National Oceanic and Atmospheric Administration, Boulder, Colorado.

NODC, 1994: *World ocean atlas CD-ROM series 1994*. National Oceanographic Data Center, National Oceanic and Atmospheric Administration.

Pacanowski, R. C. and S. M. Griffies, 1998: *MOM 3.0 Manual*. NOAA/Geophysical Fluid Dynamics Laboratory, Princeton, USA 08452.

Rahmstorf, S., 1993: A fast and complete convection scheme for ocean models. *Ocean Modelling*, **101**, 9–11.

Redi, M. H., 1982: Oceanic isopycnic mixing by coordinate rotation. *J. Phys. Oceanogr.*, **12**, 1154–1158.

Roberts, M. J., H. Banks, N. Gedney, J. Gregory, R. Hill, S. Mullerworth, A. Pardaens, G. Rickard, R. Thorpe, and R. Wood, 2004: Impact of an eddy-permitting ocean resolution on control and climate change simulations with a global coupled GCM. *J. Climate*, **17**, 3–20.

Roberts, M. J. and D. Marshall, 1998: Do we require adiabatic dissipation schemes in eddy-resolving ocean models? *J. Phys. Oceanogr.*, **28**, 2050–2063.

Smith, R. D., M. E. Maltrud, F. O. Bryan, and M. W. Hecht, 2000: Numerical simulation of the North Atlantic Ocean at $\frac{1}{10}^{\circ}$. *J. Phys. Oceanogr.*, **30**, 1532–1561.

Stammer, D., 1998: On eddy characteristics, eddy transports, and mean flow properties. *J. Phys. Oceanogr.*, **28**, 727–739.

Stevens, D. P., 1991: The open boundary condition in the United Kingdom fine-resolution Antarctic model. *J. Phys. Oceanogr.*, **21**, 1494–1499.

The Lab Sea Group, 1998: The Labrador Sea deep convection experiment. *Bull. Amer. Meteor. Soc.*, **79**, 2033–2058.

Treguier, A. M., I. M. Held, and V. D. Larichev, 1997: On the parameterization of quasi-geostrophic eddies in primitive equation ocean models. *J. Phys. Oceanogr.*, **27**, 567–580.

Trenberth, K. R., W. G. Large, and J. G. Olson, 1990: The mean annual cycle in global ocean wind stress. *J. Phys. Oceanogr.*, **20**, 1742–1760.

Visbeck, M., J. Marshall, T. Haine, and M. Spall, 1997: Specification of eddy transfer coefficients in coarse-resolution ocean models. *J. Phys. Oceanogr.*, **27**, 381–402.

Willebrand, J., B. Barnier, C. Böning, C. Dieterich, P. D. Killworth, C. Le Provost, Y. Jia, J. M. Molines, and A. L. New, 2001: Circulation characteristics in three eddy-permitting models of the North Atlantic. *Prog. Oceanogr.*, **48**, 123–161.

Wright, D. K., 1997: A new eddy mixing parametrization and ocean general circulation model. *International WOCE Newsletter*, **26**, 27–29.

Chapter 3

Analysis of an 80-Year Integration of a 1/3-degree Ocean Model of the Subpolar North Atlantic

3.1 Introduction

The stirring and mixing of tracers caused by baroclinic eddies can be parameterized in non-eddy-resolving ocean models by means of the scheme of Gent and McWilliams (1990) (GM hereafter). The use of the GM parameterization has led to many improvements in simulations with coarse-resolution z-level ocean models, such as increased northward transport of heat in the North Atlantic, sharper thermoclines and cooler deep oceans (Danabasoglu and McWilliams, 1995; Böning et al., 1995). A major achievement was the reduction of spurious diapycnal mixing obtained as a result of employing a very low explicit horizontal diffusion in these simulations.

In most published simulations with ocean models that use the GM parameterization, the eddy-transfer coefficient entering the expression of the eddy-induced velocity is taken as constant. Negative effects were obtained when a relatively large constant value of this coefficient ($10^7\ cm^2\ s^{-1}$) was used in a model of the North Atlantic (England and Holloway, 1998). Since the intensity of the eddy-induced tracer

[2]A version of this chapter has been published. Deacu, D. and P. G. Myers, 2005. Journal of Oceanography, **61**, 549-555

transport is variable in the ocean, there have been attempts to take it into account. The variable eddy-transfer coefficient proposed by Visbeck et al. (1997) (henceforth referred to as VMHS) for the GM scheme outperformed a constant coefficient in simulations with a $1.25°$-resolution model of Wright (1997), and a discussion of its effect in an eddy-permitting global ocean model was presented by Gent et al. (2002).

Myers and Deacu (2004) modelled the subpolar North Atlantic with an eddy-permitting model ($\frac{1}{3}°$-resolution) and found an unrealistic drift of the model Labrador Sea salinity. They suggested that enhanced baroclinic eddy activity along the Labrador slope strengthened the countercurrent adjacent to the Labrador Current, which entrained too much high-salinity water of North Atlantic Current origin into the Labrador Sea. Deacu and Myers (2005) considered the inclusion of a VMHS eddy-transfer coefficient and found it had a positive effect on the model results. Improvements to the simulated velocity field included a better representation of the Labrador Current and a distinct core of the Deep Western Boundary Current (DWBC) along the Labrador Slope. The more realistic circulation positively impacted the pathways of water masses and thus the hydrography. In part, this was because the spatio-temporally varying eddy-transfer coefficient field that continuously adjusted to the baroclinicity of the simulated flow, along with a biharmonic horizontal diffusion coefficient set to a relatively low value ($10^{14}\ cm^4\ s^{-1}$), allowed for enhanced spreading of water masses along isopycnal surfaces.

The improvements discussed by Deacu and Myers (2005) were obtained in a series of 14-year integrations. Because such time periods are too short for a complete adjustment of the model intermediate and deep waters, it was considered of interest to investigate the model's behaviour over periods of several decades. Of interest, too, is the impact of the variable eddy-transfer coefficient on model stability. In this note, results from a 80-year integration have been analyzed with an emphasis on the evolution of the salinity and temperature during and after the spin-up phase needed for the adjustment of the model ocean circulation to the density field. The diagnostic analysis focuses on the trends in freshwater and heat content of a region of the Labrador Sea, to give an indication of the stability of the model.

3.2 Model

SPOM (Sub-Polar Ocean Model) is a regional configuration of the Modular Ocean Model - Array (MOMA) set up for process and sensitivity studies of ocean variability in the subpolar North Atlantic. The original model formulation is based on a Bryan-Cox-Semtner type ocean general circulation model and uses the inviscid version of the Killworth et al. (1991) free surface scheme.

The model has a horizontal resolution of $\frac{1}{3}^{\circ}$ and 36 vertical levels, unevenly spaced in the vertical, with greater resolution in the upper water column. The lowest level in each column of the model is represented by a finite volume partial cell approach that allows for a significant improvement in the representation of the underlying topography. The model topography is taken from the $\frac{1}{12}^{\circ}$ ETOPO5 (NOAA, 1988) data set, linearly interpolated to the model's resolution.

The model uses the GM parameterization with a VMHS variable eddy-transfer coefficient whose lower and upper bounds are set to 0.5×10^6 and 10^7 $cm^2\ s^{-1}$, respectively. A value for the biharmonic horizontal diffusion coefficient of 7.5×10^{14} $cm^4\ s^{-1}$ ensures a low background horizontal diffusion. The biharmonic horizontal viscosity coefficient is 7.5×10^{18} $cm^4\ s^{-1}$, the vertical viscosity is 1.5 $cm^2\ s^{-1}$, and the vertical diffusion is 0.3 $cm^2\ s^{-1}$. Convective adjustment is performed using the complete convection scheme of Rahmstorf (1993).

The southern boundary is open and its formulation is based on that of Stevens (1991), modified with a flow relaxation scheme that restores the sea surface height to a reference state (taken from the diagnostic model of Myers and Weaver (1995)). Data along the southern boundary is taken from Grey and Haines (1999). Restoring buffer zones are included along the model's closed northern boundaries.

At the surface the forcing is perpetual year, for both the tracers and the winds. The surface temperature and salinity are relaxed to monthly data taken from the

NODC (1994) data atlas, with a hard restoring timescale of 2 hours. As discussed in (Myers, 2002), this choice is made to fix the potential water formation regions while leaving the basin interior free to evolve. Surface momentum fluxes are provided by the monthly climatology of Trenberth et al. (1990), averaged over the period 1980 – 1986.

The model initial conditions are taken from the NODC (1994) data set, for the month of June, linearly interpolated to the model grid and depth levels. More details of the model can be found in Myers (2002) and Deacu and Myers (2005).

3.3 Results

The ocean model has been integrated from rest for 80 years. The time series of the salinity and temperature averaged over the entire computational domain at three different depths (Fig. 3.1) indicate that, after the initial adjustment to the climatological fields and the achievement of a dynamic quasi-equilibrium, there is little long term variability beyond that associated with the annual cycle.

We shall focus on the Labrador Sea Water (LSW) pathways, as it is the most important water mass formed within the model domain. The use of the VMHS scheme, as shown in Deacu and Myers (2005), significantly improves the spreading of LSW by increasing the accuracy of the advection of this water mass along isopycnal surfaces. The eddy-induced velocity field plays a major role in this process, in the presence of a much reduced spurious diapycnal mixing obtained for the relatively small value of the explicit horizontal diffusion coefficient.

The dispersal of the model LSW can be readily seen in Fig. 3.2, which depicts the model salinity averaged over the last 5 years of integration (years 76-80) on the $\sigma_2 = 36.95$ isopycnal surface. The LSW is spread away from the deep convection region towards the Labrador Current and the Labrador Sea countercurrent mainly by the eddy-induced velocities. It is then transported to the south by the Labrador Current and into the Irminger Sea by the countercurrent. As the LSW approaches the Northwest Corner region, a significant percentage of it is recirculated back to-

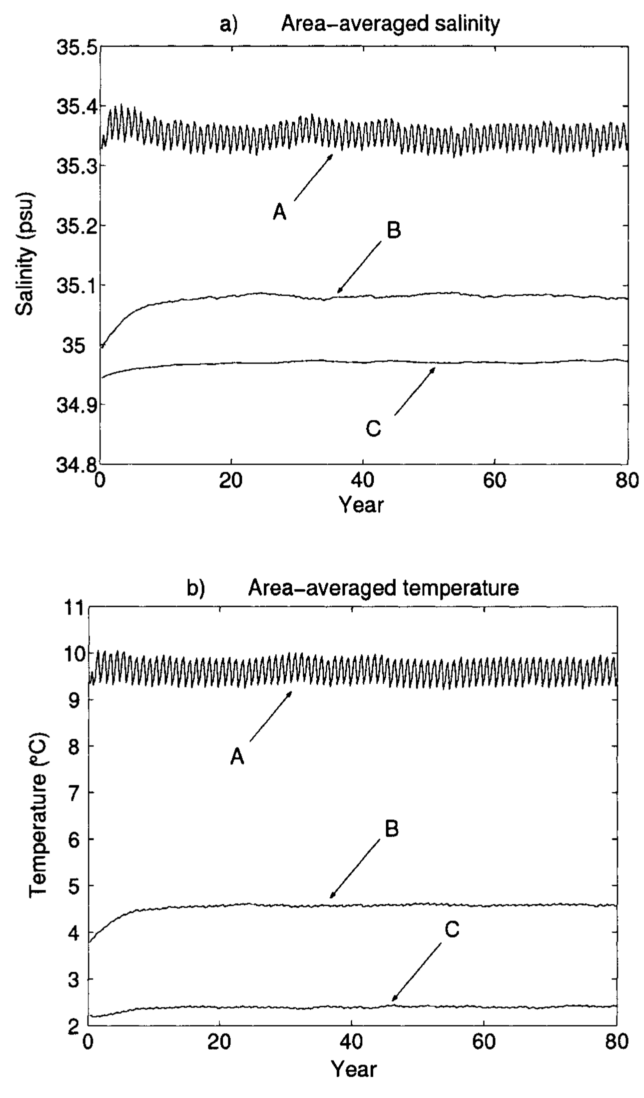

Figure 3.1: Area-averaged a) salinity and b) temperature for the entire computational domain, for three different depths: 200 m – A; 1500 m – B; 3100 m – C.

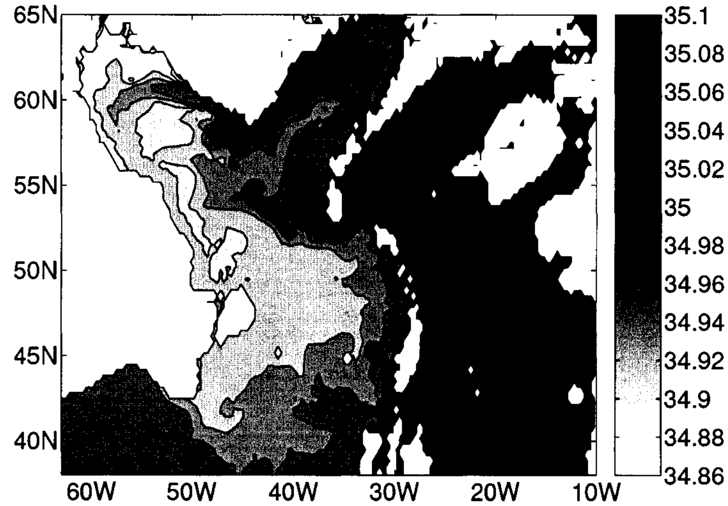

Figure 3.2: Time-averaged salinity (psu) on the $\sigma_2 = 36.95$ isopycnal (years 76-80). The contour interval is $0.02\,psu$.

wards the deep convection site by the countercurrent, with the remaining portion continuing south until it encounters the North Atlantic Current off the Flemish Cap. Dispersal then occurs via two pathways. To the south, the LSW continues along the topographic slope until it reaches the southern end of the Grand Banks. Transport further south, combined with recirculation, is accomplished by a number of quasi-stationary eddies. The eastward pathway starts off under the North Atlantic Current, spreading broadly to the north and south of the main current axis. However, very little LSW is able to penetrate the Mid-Atlantic Ridge in the model, such as through the Charlie-Gibbs Fracture Zone. At least in part, the Mid-Atlantic Ridge is acting as a barrier to the eastward spreading of LSW water in the model due to the fact that the depth of this surface in our simulations (2000-2200 m) is deeper than in reality (also noticed by Böning et al. (2003)).

The model salinity on the $\sigma_2 = 36.95$ isopycnal surface shown in Fig. 3.2 has been compared with that from a climatology based on an isopycnal vertical coordinate (Grey and Haines, 1999), as well as with the observed salinity at the LSW potential vorticity minimum depicted in Figure 4 of Talley and McCartney (1982) – neither is shown here. A good agreement has been obtained, which proves that the model has very good skill in representing LSW after long integrations, given its resolution and other limitations. The penetration of the LSW to the south, approaching the open boundary, is well simulated, the main discrepancy being an underpenetration of LSW along the topographic slope of the western boundary. The great failing of the model, as discussed in the previous paragraph, is related to the lack of penetration of LSW into the eastern basin.

The above discussion supports the statement that the model is able to provide a good representation of the hydrography and water masses within its domain, especially in the Labrador Sea. In order to assess the model's capability to maintain this skill level over a long integration, we have monitored properties within three isopycnal layers defined by the values of the potential density referenced to the surface. Since we know the model has problems in the eastern basin, we will limit this analysis to the central Labrador Sea, in a region bounded by the longitudes $63°W$ and $43°W$, and the latitudes $52°N$ and $64°N$. We characterize our three layers as surface waters ($\sigma_0 < 27.74$), LSW ($27.74 < \sigma_0 < 27.8$) and the deep waters ($\sigma_0 > 27.8$).

We define the freshwater content as

$$FW = \int_V \frac{S_r - S}{S_r} dV \tag{3.1}$$

where V is the integration volume, S is the model calculated salinity and S_r is a reference salinity. S_r was set to $35.0\ psu$; this value was chosen to be consistent with the model salinity at the offshore edge of the Labrador Current, see Myers (2002) for more details. The heat content is given by

$$H = c_p \rho_o \int_V (T - T_r) dV \tag{3.2}$$

with c_p being the specific heat capacity of water, ρ_0 the reference density (with a value of $1028\ kg\ m^{-3}$), T_r a reference temperature ($T_r = 0°\ C$), and T the model calculated temperature. In all cases, we calculate these quantities monthly and plot them seasonally. All times series (Fig. 3.3 and 3.4) show an initial drift from the values corresponding to the initial conditions, followed by a long period (the last

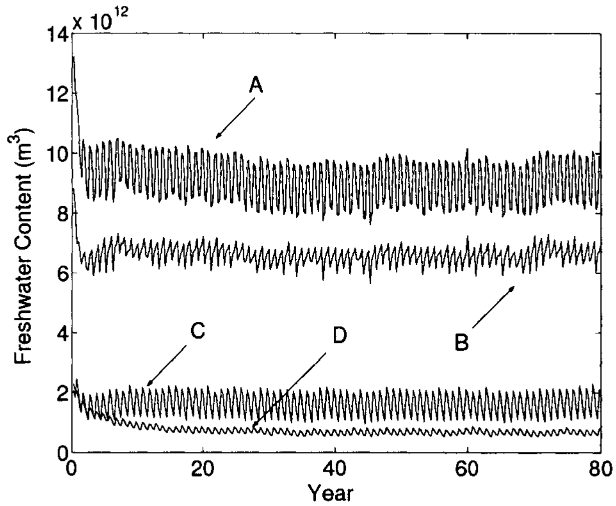

Figure 3.3: Time series of freshwater content for our Labrador Sea region. Line A is for the entire water column, B is for the surface waters ($\sigma_0 < 27.74$), C is for the intermediate waters ($27.74 < \sigma_0 < 27.80$) and D is for the bottom waters ($\sigma_0 > 27.80$).

50 years of integration) with basically no trend, during which the only variability is seasonal.

The freshwater content of our Labrador Sea region drops significantly during the first 2 years at an approximate rate of $2.0\times10^{12}\ m^3\ yr^{-1}$ and then at the much slower rate of $0.16 \times 10^{12}\ m^3\ yr^{-1}$ until around year 30 (Fig. 3.3), thereafter essentially displaying seasonal variation about an annual mean value of $\sim 9.0 \times 10^{12}\ m^3\ yr^{-1}$. The steep initial decrease is mainly due to a rapid adjustment of the water mass properties in the upper layer, whereas the following downward trend is associated with the continuous loss of freshwater content from the bottom layer. The heat content behavior is similar, albeit in the opposite direction, with an increase of $0.5 \times 10^{13}\ GJ$ from an initial value of $3.6 \times 10^{13}\ GJ$ (Fig. 3.4). After this initial period, there is essentially no trend over the rest of the integration.

Through the first 10 years of integration, the volume of the deep layer decreases while those of the upper and intermediate layers increase (Fig. 3.5). Consequently, LSW will be found, on average, at a greater depth than in the climatological density field that the model started with. The loss of volume in the deep layer is due to

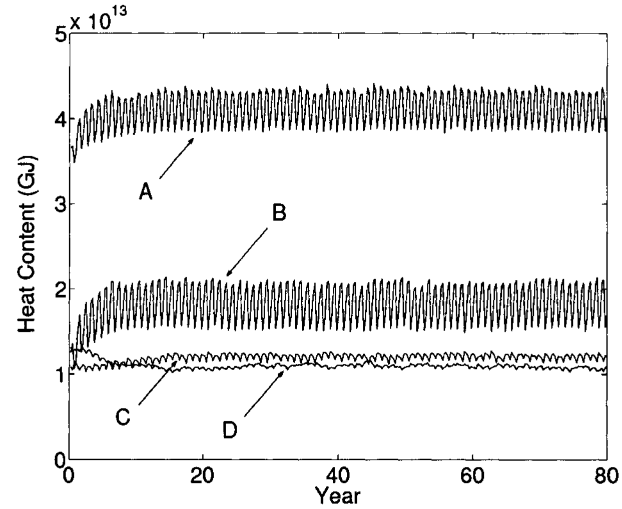

Figure 3.4: Time series of heat content for our Labrador Sea region. The curve definitions are the same as for Fig. 3.3.

weak production of dense water in the model, combined with a decrease in density of water overflowing the sills from the Nordic Seas. To understand better the evolution of watermass properties in the model, we examine the volume-averaged salinity and temperature for the three layers (Fig. 3.6). The advantage is that these quantities can clearly show whether a change in freshwater/heat content is related to an increase/decrease in salinity/temperature, or is brought about by a change in volume in the layer in question.

The time series of the volume-averaged salinity shows that the sea water in all three layers becomes saltier during the spin-up phase. A replacement of freshwater by saltier water in the top layer mainly occurs as a result of an inflow of salty and warm water of North Atlantic Current origin by means of the simulated countercurrent. Similarly, the volume-averaged temperature exhibits the same initial abrupt upward trend. As shown by Deacu and Myers (2005), the model still simulates too strong a countercurrent.

The time series for the intermediate layer — where most of the model Labrador Sea Water resides — shows only a small initial increase in salinity and temperature. In addition, there is little variability even in the seasonal amplitude in this layer over

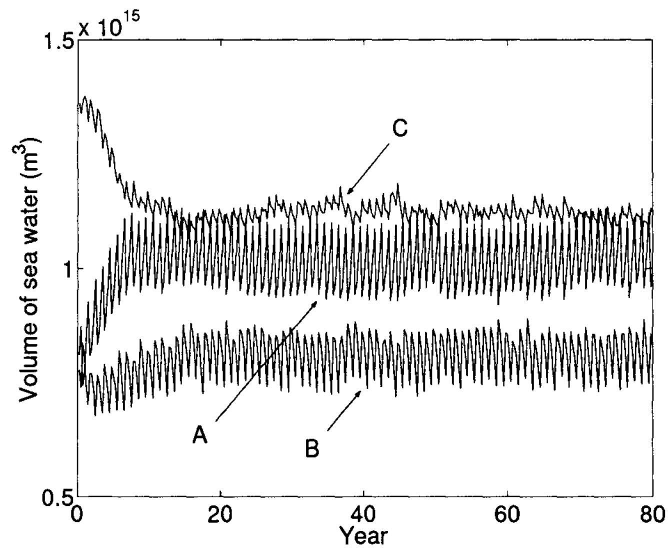

Figure 3.5: Time series of sea water volume within each layer in our Labrador Sea region. Line A is for the surface waters ($\sigma_0 < 27.74$), B is for the intermediate waters ($27.74 < \sigma_0 < 27.80$) and C is for the bottom waters ($\sigma_0 > 27.80$).

most of the integration.

In the bottom layer, the significant decrease in heat content during the first 20 years of the simulation is mainly caused by a decrease in volume rather than cooling. Temperature increases very slightly during the first 50 years of integration and then decreases to a value close to that of the initial conditions field. The volume decrease can be associated with poor deep water formation in the Nordic Seas region of the model, combined with excessive mixing (and loss of density) of those waters through entrainment of adjacent water masses as they overflow the sills connecting to the rest of the Atlantic and begin their descend along continental slope.

A comparison of the model salinity and temperature averaged over the years 76-80, and over each of the three layers of the region considered in the Labrador Sea, with the corresponding annual means from the Levitus climatology (Levitus et al., 1994) and the modified Lozier climatology (Grey and Haines, 1999) for the same layers, gives an indication of the model drift. Figure 3.6 shows that the drift from the initial conditions (taken from the Levitus climatology for the month of June) over the entire integration period is built-up almost entirely during the spin-

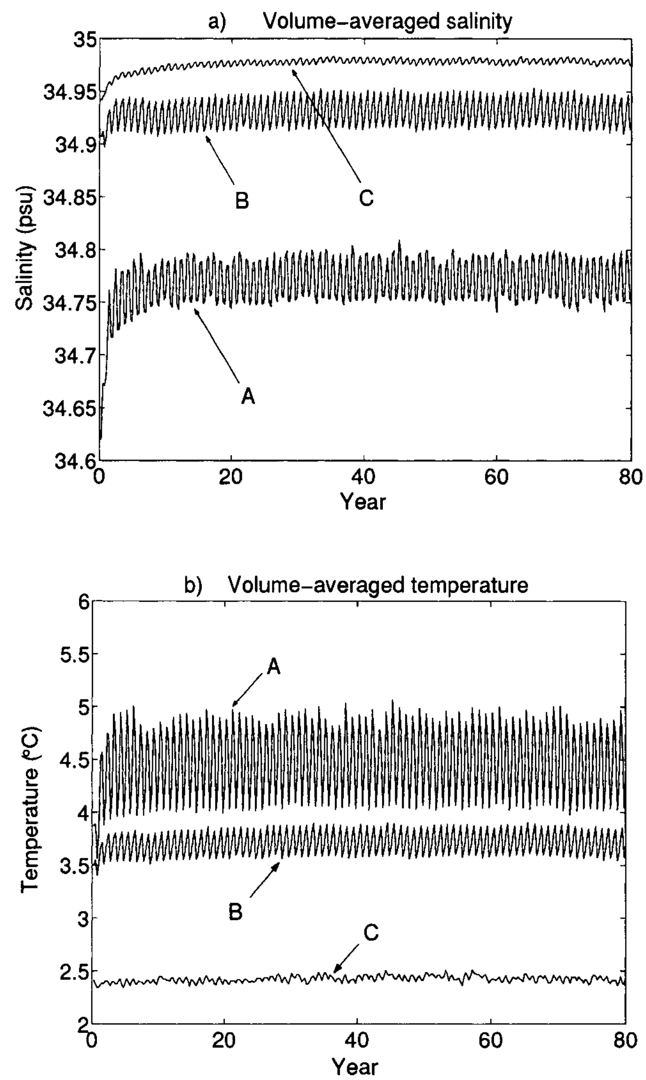

Figure 3.6: Time series of volume-averaged a) salinity and b) temperature within each layer of our Labrador Sea region. The curve definitions are the same as for Fig. 3.5.

		Model	Levitus	Lozier
Entire Water Column	S	34.90	34.86	34.85
	T	3.53	3.28	3.50
Surface Waters	S	34.78	34.70	34.72
	T	4.43	3.78	3.83
Intermediate Waters	S	34.93	34.91	34.91
(LSW)	T	3.78	3.50	3.55
Deep Waters	S	34.98	34.93	34.93
	T	2.43	2.80	3.03

Table 3.1: Average salinity (S, psu) and temperature (T, $°C$), for the model and the Levitus and modified Lozier climatologies. The climatological values are annual means, whereas the model values are spatio-temporal averages over the last 5 years of integration and over the region of the Labrador Sea bounded by the longitudes $63°W$ and $43°W$, and the latitudes $52°N$ and $64°N$. The surface, intermediate and deep waters are defined by ranges for the potential density σ_0, that is $\sigma_0 < 27.74$, $27.74 \leq \sigma_0 \leq 27.80$, $\sigma_0 > 27.80$, respectively. Note that the Lozier temperatures are in-situ temperatures while the others are potential temperatures.

up phase. The mean values for the Labrador Sea region as a whole, as well as for three layers, are provided in Table 3.1.

Interestingly, the model drift brings the temperature averaged over the Labrador Sea region to a value that is very close to that given by the modified Lozier climatology, by the end of the simulation. There are, however, differences in the vertical breakdown of the average temperature, with the model overestimating it in the upper and LSW layers and underestimating it in the deep layer. The model salinity undergoes a significant decrease, drifting away from the climatological values, especially in the surface and deep layers, as discussed above. The layer closest to the observations may be the LSW intermediate layer, where part of the model drift may be related to the poor dispersal of LSW into the eastern basin.

3.4 Summary and Discussion

Deacu and Myers (2005) reported on the results of a series of 14-year integrations involving a model of the subpolar gyre of the North Atlantic using a variable eddy-transfer coefficient for the GM scheme. As discussed in that paper, the use of this coefficient led to a number of model improvements. Since a 14-year time period is not sufficient for a complete adjustment of the intermediate and deep waters, this note investigates the model behaviour over a significantly longer integration period of 80 years.

The model is able to provide a fairly good representation of the hydrography and water masses in the model domain, especially in the Labrador Sea and retains this representation through the entire 80-year integration. Although there is a significant drift of model properties away from the initial conditions during the first 30 years of integration, there is little trend during the final 50 years. The drift in salinity is significant in the surface and deep layers. In the deep layer, it is related to excessive mixing occuring during the descent of the overflow waters.

The LSW dispersal is very well simulated in the western basin, with a good correspondence between model and observed salinity on the $\sigma_2 = 36.95$ isopycnal surface, even in the proximity of the open southern boundary. In the case of the LSW, the main dispersal pathways are set up quickly, within the first 15 years, with model LSW replacing all the water on that surface from the initial conditions. Afterwards, the LSW pattern remains stable, as low levels of diapycnal mixing prevent the erosion of this water mass.

Chao and Lozier (2001) examined the skill of a $\frac{1}{6}^\circ$ ocean general circulation model by comparing an Atlantic Ocean model to a pair of observed climatologies. Although they found a good agreement between the model and climatologies in the upper water column, they had substantial differences at intermediate and deep layers. From their comparisons, they suggested two possible model problems: bottom boundary layer processes and improper boundary specification of water masses. We would potentially restate the first of these points as the representation of the bottom topography and its interaction with the overlying circulation. As shown by our model's difficulty in dispersing LSW into the eastern basin over the Mid-Atlantic Ridge, the circulation is strongly influenced by the bottom topography. However, in this case, the problem is not purely a boundary layer process and would not be fixed by the inclusion of a bottom boundary layer scheme.

As for the statement of Chao and Lozier (2001) about the importance of the proper specification of boundary water masses, it is sensible that the source of the data for the model's open boundary condition is important. As shown in Myers (2002), the use of data from the modified Lozier isopycnal climatology (which has a better representation of the deep western boundary current and the Mediterranean Water) leads to noticeable improvements in our model. However, we would generalize the statement of Chao and Lozier (2001) to include the proper specification of the surface boundary conditions. Potentially, the success of our model in maintaining a reasonable heat content is because the use of a restoring boundary condition on the surface temperature is physically defensible, while the use of such a boundary condition on salinity has no physical justification. Additionally, sea-ice processes and its import into the region, which are not taken into account in this version of the model, are expected to play a significant role in governing the freshwater in high latitude regions.

As a final statement, we might suggest that the lack of noticeable trend in the time series analyzed in this note reflects the positive effect of both the eddy-induced velocity using a variable eddy-transfer coefficient and the low levels of spurious diapycnal mixing that the GM parameterization permitted us to use. The evidence from this note also suggests that the open boundary conditions employed do not generate significant model drift, even for integrations on the decadal to century timescale.

Bibliography

Böning, C. W., R. Holland, F. Bryan, G. Danabasoglu, and J. C. McWilliams, 1995: An overlooked problem in model simulations of the thermohaline circulation and heat transport in the Atlantic Ocean. *J.Climate*, **8**, 515–523.

Böning, C. W., M. Rhein, J. Dengg, and C. Dorow, 2003: Modelling CFC inventories and formation rates of Labrador Sea Water. *Geophys. Res. Lett.*, **30**, 22–1 to 22–4.

Chao, Y. and M. S. Lozier, 2001: Evaluation of North Atlantic property field simulations at $\frac{1}{6}^{\circ}$. *J. Phys. Oceanogr.*, **31**, 3200–3213.

Danabasoglu, G. and J. C. McWilliams, 1995: Sensitivity of the global ocean circulation to parameterizations of mesoscale tracer transports. *J.Climate*, **8**, 2967–2987.

Deacu, D. and P. G. Myers, 2005: Effect of a variable eddy transfer coefficient in an eddy-permitting model of the subpolar North Atlantic. *J. Phys. Oceanogr.*, **35**, 289–307.

England, M. H. and G. Holloway, 1998: Simulations of CFC content and water mass age in the deep North Atlantic. *J. Geophys. Res.*, **103**, 15885–15901.

Gent, P. R., A. P. Craig, C. M. Bitz, and J. W. Weatherly, 2002: Parameterization improvements in an eddy-permitting ocean model for climate. *J. Climate*, **15**, 1447–1459.

Gent, P. R. and J. C. McWilliams, 1990: Isopycnal mixing in ocean circulation models. *J. Phys. Oceanogr.*, **20**, 150–155.

Grey, S. M. and K. Haines, 1999: Climatological hydrography of the North Atlantic. *Int. WOCE Newsletter*, **36**, 23–25.

Killworth, P. D., D. Staniforth, D. J. Webb, and S. M. Patterson, 1991: The development of a free-surface Bryan-Cox-Semtner ocean model. *J. Phys. Oceanogr.*, **21**, 1333–1348.

Levitus, S., R. Burgett, and T. P. Boyer, 1994: World Ocean Atlas 1994. Volume 3: Salinity. Technical report, U.S. Department of Commerce, National Oceanographic and Atmospheric Administration.

Myers, P. G., 2002: SPOM: A regional model of the sub-polar North Atlantic. *Atmos.-Ocean*, **40**, 445–463.

Myers, P. G. and D. Deacu, 2004: Labrador Sea freshwater content in a model with a partial cell topographic representation. *Ocean Modelling*, **6**, 359–377.

Myers, P. G. and A. J. Weaver, 1995: A diagnostic barotropic finite-element ocean circulation model. *J. Atmos. Oceanic Technol.*, **12**, 511–526.

NOAA, 1988: Data announcement 88-MGG-02, Digital relief of the surface of the earth. Technical report, National Geophysical Data Center, National Oceanic and Atmospheric Administration, Boulder, Colorado.

NODC, 1994: *World ocean atlas CD-ROM series 1994.* National Oceanographic Data Center, National Oceanic and Atmospheric Administration.

Rahmstorf, S., 1993: A fast and complete convection scheme for ocean models. *Ocean Modelling*, **101**, 9–11.

Stevens, D. P., 1991: The open boundary condition in the United Kingdom fine-resolution Antarctic model. *J. Phys. Oceanogr.*, **21**, 1494–1499.

Talley, L. D. and M. S. McCartney, 1982: Distribution and circulation of Labrador Sea Water. *J. Phys. Oceanogr.*, **12**, 1189–1205.

Trenberth, K. R., W. G. Large, and J. G. Olson, 1990: The mean annual cycle in global ocean wind stress. *J. Phys. Oceanogr.*, **20**, 1742–1760.

Visbeck, M., J. Marshall, T. Haine, and M. Spall, 1997: Specification of eddy transfer coefficients in coarse-resolution ocean models. *J. Phys. Oceanogr.*, **27**, 381–402.

Wright, D. K., 1997: A new eddy mixing parametrization and ocean general circulation model. *International WOCE Newsletter*, **26**, 27–29.

Chapter 4

A Particle Model for Sea Ice Dynamics

4.1 Introduction

Most of the numerical models that have been used to simulate complex sea ice dynamics are Eulerian and rely either on finite-difference (e.g. Hibler, 1979; Hunke and Dukowicz, 1997) or finite-volume spatial discretizations (Hutchings et al., 2004). Some of them have shown considerable skill in simulating observed features of the large-scale deformation, such as the deformation localization in the interior of ice packs (e.g. Hutchings et al., 2005). However, advection in these models is inherently plagued by spurious diffusion and dispersion.

To circumvent this problem, Flato (1993) proposed a particle-in-cell (PIC) model in which the volumes of the particles are conserved along their trajectories. It was shown that the Lagrangian transport of this model led to much improved predictions of the ice edge location and the ice thickness near the same edge, in comparison with transport on an Eulerian grid. But, the model still integrates the momentum equation, and hence transports momentum, on an underlying fixed grid. Therefore, as with Eulerian models, it may alter deformation patterns in an unphysical manner.

Full Lagrangian sea ice models based on finite element methods that have many

[3] A version of this chapter has been submitted for publication. Deacu, D. and P. G. Myers, 2005. Ocean Modelling.

similarities with those that have been successfully used in computational solid mechanics have been developed by Morland and Staroszczyk (1998) and Wang and Ikeda (2004). One of their advantages over Eulerian models consists of the association of their finite elements with sea ice regions, whose evolution can thus be tracked. Of concern is the fact that the accuracy of simulations is compromised and such models may become unstable when their meshes become very distorted in regions of highly localized deformation. For instance, a highly distorted mesh near the ice edge obtained after several days of integration is shown in Morland and Staroszczyk (1998). We also note that the conservation properties of these models have not been addressed.

To deal with large deformations, the state-of-the-art finite element models used in engineering applications have the capability to refine their meshes and to increase the order of the interpolation. Nonetheless, they still encounter difficulties when slip lines or cracks occur in the material. Therefore, there has been increasing interest in recent years in the development of meshless methods that are able to overcome such problems (e.g. Rabczuk and Belytschko, 2004; Li and Liu, 2000).

A Lagrangian meshless method is the Smoothed Particle Hydrodynamics (SPH) method, which was originally developed by Gingold and Monaghan (1977) and Lucy (1977) to simulate complex astrophysical fluid flows. Since then, it has been successfully applied to the development of Lagrangian models for many complex fluid and solid dynamics problems (e.g. Tartakovsky and Meakin, 2005; Wang et al., 2005). In many instances, such models were preferred to models based on finite element or finite difference methods due to their ability to handle large deformations (e.g. Libersky et al., 1993). Apart from being meshless, this method offers the advantage of handling free boundaries and highly irregular rigid boundaries with relative ease.

The SPH formalism was first used in modelling sea ice dynamics by Gutfraind and Savage (1997a,b). They implemented a viscous-plastic rheology with a Mohr-Coulomb yield curve in their model and found a general agreement between velocity and pressure profiles obtained with their SPH model and those from a discrete-particle model. The authors also emphasized the advantage of an SPH model over Eulerian models in providing accurate predictions of the ice edge, free of artificial diffusion. However, they treated sea ice as a compressible fluid and neither the sea ice thickness nor the ice fraction were among the model variables. Instead, density became a state variable and an equation of state relating the ice pressure to the density was prescribed.

More recently, Lindsay and Stern (2004) have built a Lagrangian sea ice model (with a resolution of about 100 km) for the Arctic Ocean. They used SPH techniques to interpolate model variables and to smooth their fields as well as for the evaluation of the spatial derivatives of the velocity, and finite differences to calculate the stress gradients (at different locations). Unlike Gutfraind and Savage (1997a), Lindsay and Stern (2004) followed the approach used in the formulation of many sea ice models, that of considering the ice fraction and thickness as model variables with their evolution governed by the standard equations of Hibler (1979). In addition, the SPH particles were associated with sea ice regions obtained every time step by a Voronoi tessellation of the computational domain.

Inspired by the successful use of the SPH method in the previously mentioned sea ice models as well as by the improved accuracy provided by the PIC model of Flato (1993), we considered it worthwhile to develop an SPH-based particle model, with a view of producing more accurate simulations and eliminating ad hoc techniques. This paper presents a particle model (SPICE) for sea ice dynamics that relies on a corrected SPH method for the evaluation of the spatial derivatives of both the velocity and the internal stress, at the same locations. For a more realistic representation of an ice pack with a set of model particles, each particle represents the same pack ice patch throughout the simulation, the one associated with it after partitioning the initial domain covered by pack ice.

The pack ice of each particle is treated as a mixture of ice and lead water forming a layer whose thickness is set by that of the ice, and the evolution equations of the thickness and ice fraction are those of Gray and Morland (1994). Thus, the particle thickness is preserved as long as ridging does not occur (thermodynamic processes are neglected in the model). Moreover, the introduction of an evolution equation for the particle area ensures that the volume of the ice within each particle is conserved. SPH smoothing is not necessary to maintain the stability of SPICE, and there is no need to introduce repulsive forces to prevent the penetration of rigid boundaries by particles.

Two rheologies have been implemented and tested in SPICE, the nonlinear viscous rheology of Morland and Staroszczyk (1998) and the viscous-plastic rheology of Hibler and Schulson (2000). It is shown that SPICE is able to deal with free boundaries and to simulate the occurrence of localized shear deformation in the interior of the ice pack (with the viscous-plastic rheology).

The paper is organized as follows. Section 4.2 describes the formulation of the model and Section 4.3 its numerical integration. Results from tests with two different rheologies are given and discussed in Section 4.4. A summary and conclusions are given in Section 4.5.

4.2 Model

4.2.1 Pack ice particles

This paper proposes a model for simulating the dynamics of an ice pack by determining the evolution of a finite number of particles that represent pack ice patches making up the ice pack. These patches are obtained by partitioning the initial domain covered by the ice pack. Both external and internal forces act upon each particle. Our goal is to determine its dynamical evolution by continuously updating its position and velocity, as well as a set of state variables (e.g. area, ice fraction, thickness) associated with it. Therefore, the approach is Lagrangian.

We assume that the horizontal length scale of the particles is of the order of 10 km, relative to which the length scale of the ice floes is expected to be small

($O(1\ km)$). The chosen length scale is generally accepted as a minimum continuum length scale (e.g. Richter-Menge et al., 1996; Overland et al., 1998). The continuum hypothesis allows us to use continuum mechanics formulations for describing the mechanical behaviour of pack ice.

The model incorporates many concepts and ideas from the theoretical work of Gray and Morland (1994), who proposed a sea ice model in the context of mixture theory. As in Gray and Morland (1994), we treat pack ice as an ice-water layer that is a mixture of ice and water trapped in leads (lead water), both components moving with the same horizontal velocity $\vec{u}$. The lower and upper boundary surfaces of the layer are those of the ice. The internal stress due to floe-floe interactions corresponds to a plane stress condition in the horizontal plane. It is represented by a tensor $\boldsymbol{N}^e$ whose components are obtained by integrating the so-called extra stress (the local stress with the water pressure removed) over the depth of the layer. More details will be given in the following sections.

4.2.2 Ice volume conservation and evolution equations for particle area, ice fraction and mean thickness

Consider a pack ice particle with horizontal area S. At the bottom of the ice-lead-water interface, the pressure exerted by the water in the lead must equal that exerted by the ice, hence

$$\rho_{ice} h_{ice} = \rho_w h_w, \tag{4.1}$$

where ρ_{ice} and h_{ice} are the ice density and thickness, and ρ_w and h_w are the water density and the thickness of the lead water column, respectively. Therefore, replacing the column of lead water of thickness h_w with one of ice with the thickness h_{ice} given by (4.1) will not change the mass of the particle (the mass of the air within the particle is negligible). As a consequence, the density of the mixture in the pack ice layer, ρ, equals that of the ice. In addition to S, we introduce two new state variables for our particle: the ice fraction, denoted by A, and the mean thickness, denoted by h. A is the fraction of the particle area covered by ice, and h is the integral average of the ice thickness over the ice covered area AS. The mass of the mixture within the particle will then be $m = \rho Sh$.

The horizontal area $S(t)$ can be expressed as

$$S(t) = \int_{S(t)} ds. \tag{4.2}$$

By invoking the Reynolds transport theorem and then the divergence theorem, the rate of change of this area can be expressed in terms of the mean value of the divergence of the horizontal velocity $\vec{u}$ over the area S as follows,

$$\frac{dS}{dt} = \frac{d}{dt}\int_S ds = \int_S \frac{\partial 1}{\partial t} ds + \int_{\Gamma=\partial S} 1\vec{u}\cdot\vec{n}d\Gamma = \int_S \nabla\cdot\vec{u}\, ds = \overline{\nabla\cdot\vec{u}}S. \tag{4.3}$$

Hereinafter the overbar denotes an integral average. With the notation $\beta := \nabla\cdot\vec{u}$, we obtain

$$\frac{1}{S}\frac{dS}{dt} = \overline{\beta}. \tag{4.4}$$

The mass of ice within the particle of area S is $m_{ice} = \rho ASh$. When considering dynamic processes only – we neglect thermodynamic processes such as ice growth and melt – the mass of ice m_{ice} must be conserved. For $\rho = const.$, this is equivalent to ice volume conservation, which can be mathematically expressed as

$$\frac{d(ASh)}{dt} = 0. \tag{4.5}$$

Assuming that A, h and S are non-zero, we divide (4.5) by the ice volume ASh and obtain,

$$\frac{1}{A}\frac{dA}{dt} + \frac{1}{S}\frac{dS}{dt} + \frac{1}{h}\frac{dh}{dt} = 0. \tag{4.6}$$

From (4.4) and (4.6) we get

$$\frac{1}{A}\frac{dA}{dt} + \frac{1}{h}\frac{dh}{dt} = -\overline{\beta}. \tag{4.7}$$

Because the thermodynamic processes are neglected, the ice thickness, and hence that of the particle, can only increase. That happens when dynamic processes act to reduce the ice covered area such that sea ice starts undergoing vertical (out-of-plane) deformations. This process, generally referred to as ridging, results in an increase of the mean thickness.

A sensible assumption for low ice concentrations is that ridging does not take place. In this case, the thickness term in (4.7) vanishes and the rate of change of the ice fraction is entirely due to the variation of the area of the patch following the equation,

$$\frac{1}{A}\frac{dA}{dt} = -\overline{\beta}. \tag{4.8}$$

According to (4.8), the ice fraction increases in convergent flow ($\overline{\beta} < 0$), but nothing prevents it from becoming unphysical by exceeding its maximum value ($A_{max} = 1$), which corresponds to an arrangement/tiling of the ice floes such that no open water areas are left. In reality, even this limit state is very unlikely to be reached as a sole result of continuous rearrangement of the ice floes during sustained convergence.

A plausible assumption is that ridging starts when sea ice fraction has reached some critical level A_c, and then its contribution to the evolution of the ice fraction evolution increases with A, in such a way that it cancels that of the divergence $\overline{\beta}$ when $A = A_{max}$. Gray and Morland (1994) took into account the ridging contribution in convergent flow by inserting a term proportional to the divergence, of the form $\alpha(A)\beta\Gamma(-\beta)$, in the ice fraction equation. Repeating this procedure here for (4.8) yields

$$\frac{1}{A}\frac{dA}{dt} = -\overline{\beta}[1 - \alpha\Gamma(-\overline{\beta})]. \tag{4.9}$$

The function $\alpha(A)$ is the ratio of the vertical ridging flux to the horizontal flux of ice volume, and is prescribed such that it monotonically increases with the ice fraction from 0 (for $0 < A < A_c$) to 1 (for $A = 1$). The Heaviside function Γ acts as a switch to include (when $\Gamma(-\overline{\beta}) = 1$) or exclude (for $\Gamma(-\overline{\beta}) = 0$) the ridging term in (4.9) in convergent or divergent flow, respectively. A ridging term somewhat similar to that of Gray and Morland (1994) is given in Stern et al. (1995).

The conservation of the ice volume of an arbitrary particle requires that (4.7) be satisfied. By substituting the rate of change of the ice fraction given by (4.9) in

(4.7), we get

$$\frac{1}{h}\frac{dh}{dt} = -\alpha\overline{\beta}\Gamma(-\overline{\beta}). \tag{4.10}$$

It can be seen from this equation that h can only increase through ridging (in convergent flow, and for $A > A_c$), otherwise it is conserved along the trajectory of the particle. It should be noted that the velocity divergence due to differential motion of the floes making up the ice pack plays a key role in the evolution of the state variables S, A, and h. For the original and more rigorous derivation of (4.9) and (4.10) the reader is referred to Gray and Morland (1994).

4.2.3 Momentum equation

The momentum equation derived by Gray and Morland (1994) for a pack ice layer of unit area is,

$$\rho h\frac{D\vec{u}}{Dt} = \nabla\cdot\boldsymbol{N}^e + A\vec{\tau^a} + A\vec{\tau^w} - \rho hf\vec{e_3}\times\vec{u} - \rho hg\nabla H, \tag{4.11}$$

where $\boldsymbol{N}^e$ is the depth-integrated extra stress tensor for the mixture, $\vec{\tau^a}$ and $\vec{\tau^w}$ are the wind and water stress, respectively, f is the Coriolis parameter, $\vec{e_3}$ is a unit vector pointing vertically upwards, g is the gravitational acceleration, H is the sea surface elevation relative to a reference level, and D/Dt denotes a material derivative. Note that the term on the left hand side of (4.11) only represents the component of the rate of change of the linear momentum of the patch of pack ice due to variations of its velocity; the component due to mass variation has not been taken into account.

The integral of the sum on the right hand side of (4.11) over the area of an arbitrary particle is the resultant of the forces acting on that particle. Because the meridional variation of f over a particle with a length scale $O(10\ km)$ is negligible, we set the value of f equal to that at the current position of the particle's centroid. Additionally, consider that h is the mean thickness of the particle. Using the integral mean values of the quantities that vary over its area, the resultant force can be expressed as,

$$\vec{F} = S\left(\overline{\nabla\cdot\boldsymbol{N}^e} + A\overline{\vec{\tau^a}} + A\overline{\vec{\tau^w}} - \rho hf\vec{e_3}\times\overline{\vec{u}} - \rho hg\overline{\nabla H}\right). \tag{4.12}$$

The linear momentum of the particle is

$$\int_S \rho h \vec{u} ds = \rho h \int_S \vec{u} ds = \rho h S \overline{\vec{u}}. \tag{4.13}$$

The momentum equation of the particle is obtained by equating the rate of change of its linear momentum with the resultant force,

$$\frac{d(\rho S h \overline{\vec{u}})}{dt} = \overline{\vec{F}}. \tag{4.14}$$

By employing (4.5) and (4.9), the left hand side of this equation can be written as follows,

$$\begin{aligned} \frac{d(\rho S h \overline{\vec{u}})}{dt} &= \rho S h \frac{d\overline{\vec{u}}}{dt} + \rho \overline{\vec{u}} \frac{d(Sh)}{dt} \\ &= \rho S h \frac{d\overline{\vec{u}}}{dt} - \rho S h \frac{1}{A} \frac{dA}{dt} \overline{\vec{u}} \\ &= \rho S h \frac{d\overline{\vec{u}}}{dt} + \rho S h \overline{\beta} [1 - \alpha \Gamma(-\overline{\beta})] \overline{\vec{u}}. \end{aligned} \tag{4.15}$$

The second term on the right hand side of this equation is the contribution of the change in mass to the rate of change of the particle's momentum. This contribution is non-zero both in divergent and convergent flows, in the latter case as long as the particle contains open water. In divergent flows, both the ice covered area AS and h remain constant. Therefore, the increase in S will be solely due to the increase of the open water area. In this case, there is an influx of water in leads from the ocean, and the particle acquires a greater inertia through addition of mass. Conversely, in convergence and when ridging does not take place, S decreases while AS and h remain constant. This is accompanied by a reduction of the open water area, which in turn generates an outflux of water into the ocean. Then, the particle will lose mass and its inertia will decrease. When ridging occurs, the amount of expelled water decreases because the lead water column deepens as the pack ice layer becomes thicker.

One may now wonder what is the relative magnitude of the two contributions to the rate of change of the momentum, and if that of change in mass could be neglected. From (4.12), (4.14) and (4.15), we obtain

$$\frac{d\overline{\vec{u}}}{dt} = \frac{1}{\rho h}\overline{\nabla \cdot \boldsymbol{N}^e} + \frac{A}{\rho h}(\overline{\vec{\tau^a}} + \overline{\vec{\tau^w}}) - f\vec{e_3} \times \overline{\vec{u}} - g\overline{\nabla H} - \overline{\beta}[1 - \alpha\Gamma(-\overline{\beta})]\overline{\vec{u}}, \quad (4.16)$$

after dividing by the mass ρSh. The last term on the right hand side of this equation incorporates the effect of the change in mass on the acceleration of the particle in convergent/divergent flow. In the simulations presented in this paper, the ratio of the magnitude of this term to the sum of the three forcing terms on the right hand side of (4.16) was found to be of the order of 10^{-1}, in the absence of the Coriolis and sea surface elevation gradient forces. Consequently, keeping it in (4.16) for increased accuracy is justified.

As we shall see when we describe the rheology used in the model, the stress divergence term in (4.16) contains A as a factor. This term vanishes when ice floes do not interact with each other, but the common velocity predicted by the reduced equation will still depend on A. This is because A appears as a factor in the wind and water stress terms in (4.16), which in turn is a consequence of the assumption made by Gray and Morland (1994) that the wind and water drag forces acting upon slabs of lead water balance each other. The result is not consistent with the free-drift limit (Connolley et al., 2004), when the constituents of the mixture are expected to drift freely with a common velocity independent of the ice fraction, and this can be considered as a deficiency of the model. However, one may argue that, given the different values of the drag coefficients for ice and water at both the surface and the bottom of the pack ice layer, it is sensible to consider that the free-drift velocity will depend to some extent on A.

We are also concerned with the situation when A is very small. When A tends to 0, so do the stress divergence term, and the water and wind drag terms. Consequently, if we neglect the last three terms on the right hand side of (4.16), the acceleration of the particle will tend to zero as well, irrespective of the magnitude of the wind stress. Thus, linear momentum is imparted by the wind to the mixture layer through the ice constituent only. The correction is obvious; simply reinsert in the momentum equation the contributions of the wind and water stresses for the water constituent neglected by Gray and Morland (1994), i.e. the term $(1 - A)(\vec{\tau_*^a} + \vec{\tau_*^w})/\rho h$. Note that the star subscript indicates that the drag coefficients used to calculate those stresses are different from those used for ice. If we assume that there is no difference between these coefficients, then the combined contribution of the wind and water drag forces in (4.16) becomes $(\vec{\tau^a} + \vec{\tau^w})/\rho h$. Now, since A is no longer present in this term, the "corrected" momentum equation,

$$\frac{d\overline{\vec{u}}}{dt} = \frac{1}{\rho h}\overline{\nabla \cdot \boldsymbol{N}^e} + \frac{1}{\rho h}(\overline{\vec{\tau^a}} + \overline{\vec{\tau^w}}) - f\vec{e_3} \times \overline{\vec{u}} - g\overline{\nabla H} - \overline{\beta}[1 - \alpha\Gamma(-\overline{\beta})]\overline{\vec{u}}. \quad (4.17)$$

will be consistent with the free-drift limit. In this limit, (4.17) appears as a generalized form of equation (5) in Connolley et al. (2004). It can also be seen that, when using this momentum equation, all of the momentum transfer from the atmosphere to the ocean underlying the pack ice layer is mediated by this layer. The momentum equation is used in the model to update the mean velocity $\overline{\vec{u}}$, which is used as the velocity of the particle.

In order to determine the trajectories of the model's particles, we need to associate a position vector with each of them. Let us first consider the (horizontal component of the) position vector of a particle's centroid,

$$\overline{\vec{r}} = \frac{1}{S}\int_S \vec{r} ds, \quad (4.18)$$

where $\vec{r}$ is the position vector of an arbitrary point within S. It can be shown that the (horizontal) velocity of the centroid can be related to $\overline{\vec{u}}$ through the equation,

$$\frac{d\overline{\vec{r}}}{dt} = \overline{\vec{u}} + \frac{1}{S}\int_S \nabla \cdot \vec{u}\left(\vec{r} - \overline{\vec{r}}\right) ds. \quad (4.19)$$

We see that the two velocities are equal if and only if the integral in (4.19) evaluates to zero. For instance, this is the case when the divergence is uniform over S (e.g. for a rigid particle).

In SPICE, the current position of the particle is determined by a vector $\vec{r_p}$ that is initially set equal to the position vector of its centroid. Then, this vector is updated using the relation

$$\frac{d\vec{r_p}}{dt} = \vec{\overline{u}}. \tag{4.20}$$

By doing so, the equality $\vec{r_p} = \vec{\overline{r}}$ will no longer be guaranteed at a later time because the second term of the right hand side of (4.19) is neglected. We assume that $\vec{r_p}$ will not deviate much from the $\vec{\overline{r}}$, so that it can still be used to determine the current position of the particle.

4.2.4 Constitutive equations

To determine the resultant of the internal forces acting on a particle, which is represented by the stress-divergence term in (4.17), the depth-integrated stress tensor $\boldsymbol{N}^e$ need be known. It is assumed that this tensor can be related to the strain rate tensor via a relationship (constitutive equation) that describes how pack ice deforms under loading (i.e. its rheology). In the following, we give a brief presentation of two rheologies that we have implemented and tested in our model.

The nonlinear viscous rheology of Morland and Staroszczyk

The state of plane stress within an arbitrary ice floe (supposed to be rigid) induced by its interaction with surrounding floes is expressed in Gray and Morland (1994) by means of a depth integrated extra stress averaged over the floe. The authors show that this mean stress, denoted by $\boldsymbol{N}^E$, is essentially determined by the extra edge tractions and the geometry of the floe. Since the extra stress is due to ice-ice interactions only, the depth integrated extra stress for the mixture will be given by $\boldsymbol{N}^e = A\boldsymbol{N}^E$.

Gray and Morland (1994) consider that $\boldsymbol{N}^E$ is proportional to an actual stress $\boldsymbol{\sigma}^E$ that corresponds to the situation when the floe is in full contact with the adjacent floes. The coefficient of proportionality is the product of two functions, $t = t(h)$ and $l = l(A)$, which depend on the thickness and ice fraction, respectively. The former accounts for the integration of $\boldsymbol{\sigma}^E$ over the depth of the floe, while the latter varies from 0 to 1 and gives the fraction of this stress that contributes to $\boldsymbol{N}^E$.

Obviously, this contribution should increase with the contact length measured along the lateral boundary of the floe, which in turn increases with A. Hence, the depth integrated extra stress for the mixture becomes

$$\boldsymbol{N}^e = A\boldsymbol{N}^E = Atl\boldsymbol{\sigma}^E. \tag{4.21}$$

The expressions of the functions t and l used in the experiments with the nonlinear viscous rheology presented in this paper,

$$t(h) = h \tag{4.22}$$

and

$$l(A) = \frac{e^{-\lambda(1-A)} - e^{-\lambda}}{1 - e^{-\lambda}}, \tag{4.23}$$

where $\lambda \gg 1$, are taken from Gray and Morland (1994).

Morland and Staroszczyk (1998) (MS hereinafter) proposed a nonlinear viscous law for the plane stress tensor $\boldsymbol{\sigma}^E$ of the form

$$\boldsymbol{\sigma}^E = \sigma^* \left(\phi_1 \boldsymbol{D} + \phi_0 \boldsymbol{I}\right) \Gamma(-\beta), \tag{4.24}$$

where σ^* is a typical value for the compressive strength of compact sea ice, ϕ_0 and ϕ_1 are two functions (called viscous response functions), $\boldsymbol{I}$ is the identity tensor, and $\boldsymbol{D}$ is the strain rate tensor. The presence of the Heaviside function in the constitutive equation (4.24) shows a particular feature of this rheology, namely that it predicts non-zero stresses in converging flows only. In the context of this nonlinear viscous rheology, the depth integrated extra stress will be given by

$$\boldsymbol{N}^e = \sigma^* hA \frac{e^{-\lambda(1-A)} - e^{-\lambda}}{1 - e^{-\lambda}} \left(\phi_1 \boldsymbol{D} + \phi_0 \boldsymbol{I}\right) \Gamma(-\overline{\beta}). \tag{4.25}$$

Note that the mean value of the divergence, $\overline{\beta}$, is used in our implementation of this viscous law.

The quantity

$$P_{GM} = \sigma^* hA \frac{e^{-\lambda(1-A)} - e^{-\lambda}}{1 - e^{-\lambda}} \tag{4.26}$$

represents the compressive strength per unit width of a mixture of thickness h and ice fraction A, and has units of $N\ m^{-1}$. When A and h take unit values, we retrieve the compressive strength of a layer of compact ice of unit width and thickness, i.e. $P_{GM} = \sigma^*$.

The components of tensor $\boldsymbol{D}$ are

$$D_{ij} = \dot{\epsilon}_{ij} = \frac{1}{2}\left(\frac{\partial u_i}{\partial x_j} + \frac{\partial u_j}{\partial x_i}\right), \quad i,j = 1,2. \tag{4.27}$$

We adopt the convention that summation over repeated indices will be implicit. The divergence of the velocity field, also referred to as dilation rate, is the first invariant of tensor $\boldsymbol{D}$,

$$\dot{\epsilon}_{kk} = \nabla \cdot \vec{u} = \beta. \tag{4.28}$$

The second invariant is the maximum shear strain rate,

$$\gamma = \left[\left(\frac{\dot{\epsilon}_{11} - \dot{\epsilon}_{22}}{2}\right)^2 + \dot{\epsilon}_{12}^2\right]^{1/2} = \dot{\epsilon}_{12,max}. \tag{4.29}$$

To ensure that the viscous law is independent on the orientation of the horizontal axes, MS considered the functions ϕ_0 and ϕ_1 to depend on β and γ only.

We introduce a mechanical pressure p^E associated with the stress tensor $\boldsymbol{\sigma}^E$ by $p^E = -(\sigma_{11}^E + \sigma_{22}^E)/2$. Using the indicial notation, (4.24) reads

$$\sigma_{ij}^E = (\sigma^* \phi_1 \dot{\epsilon}_{ij} + \sigma^* \phi_0 \delta_{ij})\, \Gamma(-\beta). \tag{4.30}$$

Therefore,

$$p^E = -\sigma^* \left(\phi_0 + \frac{1}{2}\phi_1 \beta\right) \Gamma(-\beta) = -\sigma^* \phi_b\,. \tag{4.31}$$

MS name ϕ_b the bulk response function and assume that it depends only on the dilation rate β through the relation

$$\phi_b = \phi_b^* \frac{\beta}{(\beta_c^2 + \beta^2)^{1/2}} \Gamma(-\beta), \tag{4.32}$$

where β_c is a prescribed dilation rate value. We see that $\phi_b \to -\phi_b^*$ as $\beta \to -\infty$. Thus, $-\phi_b^*$ is a lower bound for ϕ_b, or, equivalently, ϕ_b^* is an upper bound for $-\phi_b$. Therefore,

$$p^E < \sigma^* \phi_b^* \ \text{ and } \ p^E \to \sigma^* \phi_b^* \ \text{ as } \ \beta \to -\infty. \tag{4.33}$$

The viscous response function ϕ_1 of the same rheology is given by the relation

$$\phi_1 = \frac{-\phi_b \phi_s^*}{(\gamma_c^2 + \gamma^2)^{1/2}}, \tag{4.34}$$

where γ_c is a constant shear strain rate value, and ϕ_s^* is a constant value for which we shall provide a physical interpretation later on. Once ϕ_b and ϕ_1 are determined, ϕ_0 can be calculated as $\phi_0 = \phi_b - \phi_1 \beta/2$.

MS express ϕ_b^* as a function of ϕ_s^*, such that the stress returned by (4.30) lies within a region bounded by a teardrop-like curve in the negative principal stress quadrant, defined by

$$\left[\left(\sigma_1^E\right)^2 + \left(\sigma_2^E\right)^2 \right]^n = 2\left(\sigma^*\right)^{2n-2} \sigma_1^E \sigma_2^E, \tag{4.35}$$

where σ_1^E and σ_2^E are the principal stresses, and n is a parameter ($n > 1$). The length of the major axis of this closed curve in principal axes is σ^*, regardless of the value of n, which only modifies the aspect ratio of the curve. If ϕ_s^* takes on a prescribed value, then ϕ_b^* will depend on it through the relation

$$\phi_b^* = \frac{1}{\sqrt{2}} \left\{ \frac{[1 + (\phi_s^*)^2]^n}{1 - (\phi_s^*)^2} \right\}^{-\frac{1}{2n-2}}. \tag{4.36}$$

If the parameter β_c is set equal to a typical magnitude for β, then γ_c can be calculated with the formula

$$\gamma_c = 2\phi_s^* \beta_c, \tag{4.37}$$

for $n = 1.5$.

We now give a physical interpretation of the parameter ϕ_s^*, which is not found in MS. The maximum shear stress (the second invariant of the stress tensor) for the stress state given by (4.30), denoted here by q^E, is

$$q^E = \sigma_{12,max} = \left[\left(\frac{\sigma_{11}^E - \sigma_{22}^E}{2} \right)^2 + (\sigma_{12}^E)^2 \right]^{1/2} = \sigma^* \phi_1 \dot{\epsilon}_{12,max} = \sigma^* \phi_1 \gamma\,. \tag{4.38}$$

Therefore, the ratio of q^E by p^E (the first stress invariant) will be

$$\frac{q^E}{p^E} = \frac{\sigma^* \phi_1 \gamma}{-\sigma^* \phi_b} = \phi_s^* \frac{\gamma}{(\gamma_c^2 + \gamma^2)^{1/2}} < \phi_s^*\,. \tag{4.39}$$

If the stress point represented by the pair (p^E, q^E) lay on a Mohr-Coulomb yield curve (commonly used for granular materials), then the ratio q^E/p^E would be equal to the sine of an internal friction angle characteristic to the material. The friction angle is a shear strength parameter that relates the normal stress to the shear strength along the sliding surface. Although our rheology is different, we can still infer a friction angle Φ via the relation

$$sin(\Phi) = \frac{q^E}{p^E} = \phi_s^* \frac{\gamma}{(\gamma_c^2 + \gamma^2)^{1/2}}, \tag{4.40}$$

which shows that Φ will increase with the amount of shear strain rate (quantified by γ). Therefore, Φ appears as a mobilized friction angle whose upper bound is the friction angle Φ^* defined by $sin(\Phi^*) = \phi_s^*$. The region of allowable stress states in the principal axes is thus bounded by means of the limit of bulk response function ϕ_b^* and the friction angle $\Phi^* = sin^{-1}(\phi_s^*)$. The former limits the pressure p^E via (4.31), while the latter limits the maximum shear stress q^E via $q^E/p^E < sin(\Phi^*)$, once p^E is known. The interpretation of the parameter ϕ_s^* as the sine of a limit friction angle for sea ice is useful when prescribing its value. For example, if we set Φ^* equal to a typical value for the friction angle for sea ice of 30°, we get $\phi_s^* = sin(30°) = 0.5$.

The viscous-plastic rheology of Hibler and Schulson

Sea ice deformation inferred from satellite imagery data covering the Arctic Ocean is concentrated along linear features with preferred orientations (Kwok, 2001). But the occurrence of such large scale linear patterns in the ice pack is not restricted to the Arctic. They have also been observed in subpolar seas, such as the Labrador Sea (Drinkwater and Squire, 1989). These features, also referred to as linear kinematic features (LKFs), may be leads created when ice floes drift apart, pressure ridges that result when ice floes are pushed together, or slip lines that develop in regions of localized shear failure. Therefore, they reveal discontinuities in the pack ice motion. There is observational evidence that LKFs divide the ice pack into quasi-rigid plates or floe aggregates characterized by quasi-uniform motion of the constituent ice floes (e.g. Stern et al., 1995; Overland et al., 1998;

Lindsay and Stern, 2003; McNutt and Overland, 2003). This suggests a mechanical behaviour for pack ice similar to that of plastic granular materials (Overland et al., 1998), and is one of the reasons why sea ice modellers have used many ideas from plasticity theories developed for such materials (e.g. Coon et al., 1974; Hibler, 1979; Tremblay and Mysak, 1997).

Hopkins et al. (2004) used a floe-scale discrete sea ice model to simulate the dynamics of pack ice that was enabled to withstand tension by initially freezing together its ice floe constituents. Under the action of a nonuniform wind stress field, fractures were initiated and then propagated within the ice pack as a result of tensile failure. Consequently, the ice floes organized into aggregates delineated by fractures (leads). The aggregates underwent continuous transformation, mainly due to closing of existent leads and opening of new ones. In addition, the deformation of the ice pack was localized along the boundaries of these aggregates, in agreement with observed deformation patterns. Therefore, Hopkins et al. (2004) argued for an aggregate structure of the Arctic ice pack that results from ice floes freezing together and localized fracturing. Note that although the assumption that pack ice has tensile strength due to cementation of ice floes through freezing is in contradiction with a postulate for sea ice dynamics (Smith, 1983) stating that pack ice cannot withstand tension due to the existence of cracks, measurements of pack ice stress have indicated the opposite (e.g. Coon et al. (1998)). Thus, the postulate appears to be valid at length scales of $\sim 100\ km$, i.e. larger than the typical size of floe aggregates, or where pack ice can no longer be considered isotropic (Coon et al., 1998).

Both the orientation and distribution of the LKFs, which have a controlling effect on the motion of floe aggregates, and the reduced strength of the thin ice formed in leads induce anisotropy in the pack ice dynamics. This has prompted the development of models of sea ice dynamics with anisotropic rheologies (Coon et al., 1998; Hibler and Schulson, 2000; Hibler, 2001a; Wilchinsky and Feltham, 2004). Hibler (2001a) performed sea ice dynamics simulations with three different rheologies (of which one was anisotropic and the other two isotropic), and focused on their ability to reproduce LKFs in the Arctic basin as narrow regions of failure reflected by highly localized shear deformation. For a grid resolution of 55 km, the anisotropic rheology provided the highest density of intersecting failure lines. The closest to this rheology, in terms of the similarity of the maximum shear patterns produced, was the isotropic modified Coulombic rheology of Hibler and Schulson (2000), whereas the classical rheology with elliptical yield curve of Hibler (1979) provided smoother fields and a reduced number of intersections. Hibler (2001a) concluded that the results obtained with the anisotropic rheology and with the isotropic modified Coulombic rheology were qualitatively similar. Moreover, the simulations of Heil and Hibler (2002) and Hutchings et al. (2005) have proved the appropriateness of the latter rheology for predicting sea ice deformation. In addition, since floe aggregates are partly resolved at a resolution of about 10 km, while the individual floes are not, the use of a constitutive model that incorporates Coulombic failure is justified according to Hibler (2001b). Therefore, we have decided to test the modified Coulombic rheology in our model.

The isotropic modified Coulombic constitutive law proposed by Hibler and Schulson (2000) (HS hereinafter) can be expressed in the form

$$N_{ij}^{e} = 2\eta\dot{\epsilon}_{ij} + \left[(\zeta - \eta)\dot{\epsilon}_{kk} - \frac{P_{HS}}{2}\right]\delta_{ij}, \tag{4.41}$$

where N_{ij}^{e} should be viewed as a depth integrated extra stress, in the context of the theory of Gray and Morland (1994), ζ and η are the nonlinear bulk and shear viscosities, respectively, and P_{HS} is a pressure related to the compressive strength of pack ice with the same units ($N\ m^{-1}$) as N_{ij}^{e}. This equation is used to evaluate the strain-rate-driven stress state for any deformation state.

A combined strain rate invariant defined by

$$\Delta = \left(\beta^2 + \frac{4\gamma^2}{e^2}\right)^{1/2}, \tag{4.42}$$

where e is a parameter that we shall introduce shortly, is used to discern between two possible states pack ice can have at a given point and time, within the framework of the proposed viscous-plastic rheology: plastic or viscous. (Note that β and γ have the same meaning throughout this paper.) For deformation levels greater than a prescribed threshold value Δ_c, i.e. for $\Delta \geq \Delta_c$, pack ice is assumed to be in a state of plastic yielding. When $\Delta < \Delta_c$, pack ice is considered to behave similarly to very viscous fluids.

For the plastic yielding state, HS proposed that

$$P_{HS} = 0.91 P^{yield}. \tag{4.43}$$

Since the expression of P^{yield} is not given in that paper, we assume that its traditional form (Hibler, 1979) was employed. For our model, we have inserted the ice fraction as an additional factor in that expression to obtain

$$P^{yield} = P^* h A e^{-\lambda(1-A)}, \tag{4.44}$$

which is similar to that of the compressive strength of the viscous rheology of Morland and Staroszczyk (1998), given by (4.26). This ensures that $P^{yield} \rightarrow 0$ when $A \rightarrow 0$. P^* and λ are empirical parameters, with the former giving the compressive strength of compact sea ice (with units of $N\ m^{-2}$).

For the same plastic regime, HS determine the bulk and shear viscosities such that the stress state returned by (4.41) is represented by a point that lies on a Mohr-Coulomb yield curve capped by a semi-ellipse (whose ratio of the major axis to the minor axis is denoted be e) in the principal stress axes. The sign of the divergence β gives the location of the stress point on the yield curve. The stress point lies on the elliptical portion of the curve for $\beta < 0$ (convergent flow), and on the linear part for $\beta > 0$ (divergent flow). The two curves intersect each other at two points reached when $\beta = 0$ (state of pure shear). The expressions of the viscosities for the elliptical part of the yield curve,

$$\zeta = \frac{P^{yield}}{2\Delta} \tag{4.45}$$

and

$$\eta = \eta_{ellipse} = \frac{\zeta}{e^2} \tag{4.46}$$

are obtained by considering the plastic flow rule to be associative there (see, for example, Hibler (1977) for more details). For the linear (Coulombic) part of the yield curve, ζ is still given by (4.45), whereas η is calculated with the formula

$$\eta = \frac{\frac{P^{yield}}{2} - \zeta\beta}{2e\gamma} = \frac{\frac{P_{HS}}{1.82} - \zeta\beta}{2e\gamma}, \tag{4.47}$$

for $\gamma \neq 0$.

By invoking this relation, we can obtain the friction angle associated with the coulombic part the yield curve as

$$\Phi_{HS} = sin^{-1}\left(\frac{1}{e}\right) \approx 46°, \tag{4.48}$$

for $e = \sqrt{1.91716} \approx 1.38$ (the value used by HS and Heil and Hibler (2002)). Examples of friction angle values for pack ice inferred from observations are 30° (Alexeev et al., 2003), 31° (Overland and Pease, 1988) and 42° (Coon et al., 1998). A friction angle of 30° corresponds to $e = 2$ (the value usually used for the elliptical yield curve of Hibler (1979)).

There seems to be some confusion regarding the compressive strength of the pack ice in the context of this rheology. To show this, we first determine the maximum value of the pressure obtained from the constitutive law (4.41). The relation for the mechanical pressure p^e is,

$$p^e = -\frac{N_{11}^e + N_{22}^e}{2} = \frac{P_{HS}}{2} - \zeta\beta. \tag{4.49}$$

By invoking (4.43) and (4.45), we obtain

$$p^e = \frac{P^{yield}}{2}\left(0.91 - \frac{\beta}{\Delta}\right). \tag{4.50}$$

When pack ice undergoes no shearing deformation ($\gamma = 0$), $\Delta = |\beta|$. If, in addition, pack ice is converging, then p^e reaches its maximum value, $p^e_{max} = 1.91P^{yield}/2 = 0.955P^{yield}$. Thus, the constitutive law gives a magnitude of the compressive strength ($0.955P^{yield}$) that is smaller than that of the prescribed compressive strength P^{yield}.

The rheology of HS allows for a small tensile strength. This is set by the minimum value of the pressure, $p^e_{min} = -0.09P^{yield}/2 = -0.045P^{yield}$, which is returned by the constitutive law for $\beta > 0$ and $\gamma = 0$ (pack ice undergoes purely divergent deformation). Notice that the maximum pressure difference is $p^e_{max} - p^e_{min} = P^{yield}$, and this controls the size of the yield curve. We note that allowing for a small tensile strength amounts to treating pack ice as a cohesive material. This could be attributed to the cementation of adjacent floes by freezing together. Thus, the Mohr-Coulomb portion of the yield curve would describe the shear failure of pack ice as a cohesive-frictional material with dilatant behaviour.

When $\Delta < \Delta_c$, pack ice is treated as a very viscous fluid. To achieve this state, HS limit the bulk viscosity to a maximum value,

$$\zeta_{max} = 10^6 P^{yield}. \tag{4.51}$$

This value can be obtained by setting the minimum value of Δ used in (4.45) to $\Delta_c = 5\times10^{-7}\, s^{-1}$. For the viscous state, the shear viscosity is obtained by replacing ζ with ζ_{max} in either (4.46) or (4.47), depending on the sign of β. Additionally, the pressure used in (4.41) is now given by

$$P_{HS} = 0.91\frac{\Delta}{\Delta_c}P^{yield}. \tag{4.52}$$

Note that $P_{HS} \rightarrow 0$ when $\Delta \rightarrow 0$.

4.3 Numerical integration

4.3.1 Spatial Discretization - Smoothed Particle Hydrodynamics

In the previous sections, pack ice was treated as a continuum following the theory of Gray and Morland (1994). We tacitly assumed that the field variables were represented by sufficiently smooth functions so that their differentiation and integration was possible whenever necessary. A set of pack ice particles was obtained by partitioning the pack ice cover at the beginning of the simulation. The evolution equations (4.4), (4.9), (4.10), (4.17) and (4.20), derived for an arbitrary particle, contain integral averages of field variables over the horizontal domain of the particle. It should be noted that the time integration of this set of differential equations does not update all of the information related to the pack ice patch associated with this particle at the beginning of the simulation. The current geometry of the patch undergoing continuous deformation, for example, remains unknown. Therefore, the particle only represents the associated pack ice patch, without being identical to it.

Since the equations of the model particles are formulated in a Lagrangian framework, there are no advection terms. However, spatial derivatives of field variables are still present in the stress divergence term of (4.17) as well as in the strain rate tensor (Eq. 4.27). We use Smoothed Particle Hydrodynamics (SPH) techniques to evaluate these derivatives.

SPH methods are numerical techniques for finding *approximations* of functions and their derivatives when the function values are known at a finite number of moving points. As an example, the value of a function f at an arbitrary point (represented by a position vector $\vec{r}$) can be approximated by

$$f(\vec{r}) \approx f_{\xi}(\vec{r}) = \sum_{n=1}^{N} f(\vec{r_n}) W(\vec{r} - \vec{r_n}, \xi_n) S_n, \tag{4.53}$$

where N is the number of points where the value of f is known, W is a differentiable kernel function depending on a parameter ξ_n (called the smoothing length), and S_n is an area (or volume in 3D) associated with the point represented by $\vec{r_n}$. With the notation $W_n(\vec{r}) = W(\vec{r} - \vec{r_n}, \xi_n)$, one can approximate the gradient of f by taking the gradient of (4.53) as follows (Monaghan, 1992),

$$\nabla f(\vec{r}) \approx \nabla f_{\xi}(\vec{r}) = \sum_{n=1}^{N} f(\vec{r_n}) \nabla W_n(\vec{r}) S_n. \tag{4.54}$$

Importantly, because this step only involves taking the gradient of an analytical function (W), no underlying computational grid is needed.

In SPH-based models, each moving point has an area (in 2D), carries values of field variables (e.g. state variables), and is usually referred to as an SPH particle.

One may now wonder if such a particle could be identical to the same physical parcel of a deformable continuum at all times. Obviously, that would require that information on the shape of the SPH particles be updated during calculations. But, this is not usually done in applications, due the complexity that would entail. Consequently, as long as the information these particles carry is incomplete, they are fictitious parcels and should not be viewed as physical parcels. This is also the case of the particles of our model, which will become SPH particles when SPH approximations are used.

For most of the kernel functions used in standard SPH approaches (e.g. Monaghan, 1992), $f(\vec{r}) \neq f_\xi(\vec{r})$. In many cases, the kernel approximation (4.53) does not even have zeroth-order consistency (Belytschko et al., 1996), i.e. it cannot reproduce constant functions. One way to overcome this problem is to replace the kernel W with a corrected kernel W^* (e.g. Bonet and Lok, 1999) defined by

$$W_m^*(\vec{r}) = W_m(\vec{r}) I_\xi^{-1}, \text{ with } I_\xi = \sum_{n=1}^{N} W_n(\vec{r}) S_n. \tag{4.55}$$

Then, the kernel approximation will exactly interpolate any constant function. This can be easily shown for $f(\vec{r}) = c$,

$$f_\xi(\vec{r}) = \sum_{n=1}^{N} f(\vec{r_n}) W_n^*(\vec{r}) S_n = c I_\xi^{-1} \sum_{n=1}^{N} W_n(\vec{r}) S_n = c = f(\vec{r}). \tag{4.56}$$

Bonet and Lok (1999) have also proposed a correction for the gradient of the corrected kernel of the form,

$$\nabla^* W_n^*(\vec{r_m}) = \boldsymbol{L}_m \nabla W_n^*(\vec{r_m}). \tag{4.57}$$

Here, $\vec{r_m}$ identifies the location of the SPH particle where the gradient is evaluated, whereas n identifies an arbitrary particle. The correction matrix $\boldsymbol{L}_m$ is evaluated using the relation

$$\boldsymbol{L}_m = \left(\sum_{n=1}^{N} S_n \nabla W_n^*(\vec{r_m}) \otimes \vec{r_n} \right)^{-1}, \tag{4.58}$$

where the symbol $\otimes$ denotes the dyadic product of two vectors. The gradient of the corrected kernel is obtained by taking the gradient of (4.55),

$$\nabla W_m^*(\vec{r}) = \left(\nabla W_m(\vec{r}) - W_m^*(\vec{r}) \sum_{n=1}^{N} \nabla W_n(\vec{r}) S_n \right) I_\xi^{-1}. \tag{4.59}$$

(If one compares (4.59) with the equivalent equation given in Bonet and Lok (1999), then one finds a factor missing in the latter.)

In our model, W is the two-dimensional Gaussian kernel defined by

$$W(\vec{r}, \xi) = \frac{1}{\pi \xi^2} e^{-\frac{r^2}{\xi^2}}, \quad r = |\vec{r}|, \tag{4.60}$$

and we evaluate W^* and its corrected gradient using (4.55) and (4.57), respectively. Then, the spatial derivatives of the velocity vector and stress tensor are approximated using (4.54). All of the prognostic variables and SPH approximations are evaluated at the same locations, namely those of the particles. Thus, the approximations obtained for the components of the strain rate tensor (Eq. 4.27) at the current location of particle m are

$$\dot{\epsilon}_{ij}(\vec{r_m}) \approx \frac{1}{2} \sum_{n=1}^{N} \left[u_i(\vec{r_n}) \frac{\partial^* W_n^*}{\partial x_j}(\vec{r_m}) + u_j(\vec{r_n}) \frac{\partial^* W_n^*}{\partial x_i}(\vec{r_m}) \right] S_n, \quad i, j = 1, 2, \tag{4.61}$$

where the star superscript indicates that corrections are used. These approximations are then used to calculate the stress tensor by means of the chosen constitutive law. Once the stress state is determined, the evaluation of the stress divergence term in the momentum equation is performed using derivatives of the stress tensor components, N_{ij}^e, whose gradients are approximated by

$$\nabla N_{ij}^e(\vec{r_m}) \approx \sum_{n=1}^{N} N_{ij}^e(\vec{r_n}) \nabla^* W_n^*(\vec{r_m}) S_n. \tag{4.62}$$

It should be noted that only SPH approximations of derivatives are actually used in calculations, and that there is no need to determine the SPH estimates of the velocity and stress fields in the model. Lindsay and Stern (2004) found it necessary for the stability of their numerical model to smooth (by calculating the SPH approximation) the velocity in the vicinity of the boundary, every time step. This is not the case in SPICE, and we do not smooth any of the prognostic variables. Thus, a potentially significant degradation of the particles velocity, thickness, and ice fraction is avoided. In addition, this also helps in getting narrower shear zones in the ice pack by preventing the simulation of overly smooth deformation fields.

The smoothing length ξ_n of the kernel associated with an arbitrary SPH particle n controls the weight with which a property value $(f(\vec{r_n}))$ carried by that particle enters an SPH approximation of type (4.53), for example. The larger its value, the larger the radius of influence of the local value on the approximations calculated in its neighbourhood, which results in increasingly smooth fields. On the other hand, ξ_n cannot be too small as this will mean that the particle will not be "felt" by the surrounding particles. Actually, the local spatial resolution in an SPH model is more related to the local value of the smoothing length than to the inter-particle distances.

The methods of prescribing optimum values for the smoothing length that improve the accuracy of the SPH simulations are more or less ad hoc. For example, in two-dimensional compressible flows, ξ_n can be varied with the local density ρ_n according to (Benz, 1990),

$$\rho_n(t)\xi_n^2(t) = const. \tag{4.63}$$

Since the density of the pack ice layer is constant in our model, we vary ξ_n using the relation

$$\xi_n(t) = \kappa S_n^{1/2}(t), \tag{4.64}$$

where κ is a constant. As in (4.63), the smoothing length in (4.64) is proportional to the square root of the particle area.

4.3.2 Time integration

The time integration scheme used in the model is based on the predictor-corrector version of the leapfrog algorithm described in Monaghan (2000). The particle area, ice fraction and thickness are time-stepped in the same manner as density is in Monaghan (2000).

Assume that at time t_n the state variables associated with an arbitrary particle are all known. We denote the right hand sides of (4.17), (4.4), (4.9) and (4.10) evaluated at time t_n by $\vec{R}_{u,n}$, $R_{S,n}$, $R_{A,n}$ and $R_{h,n}$, respectively. The time-stepping starts by calculating predictors for velocity, area, ice fraction and thickness

$$\begin{aligned}
\vec{u}^{\star}_{n+1} &= \vec{u}_n + \delta t \vec{R}_{u,n}, && (4.65)\\
S^{\star}_{n+1} &= S_n + \delta t S_n R_{S,n}, && (4.66)\\
A^{\star}_{n+1} &= A_n + \delta t A_n R_{A,n}, && (4.67)\\
h^{\star}_{n+1} &= h_n + \delta t h_n R_{h,n}. && (4.68)
\end{aligned}$$

Then, the position vector is updated,

$$\vec{r}_{p,n+1} = \vec{r}_{p,n} + \delta t \left(\vec{u}_n + 0.5 \delta t \vec{R}_{u,n} \right). \quad (4.69)$$

Next, $\vec{R}_{u,n+1}$, $R_{S,n+1}$, $R_{A,n+1}$ and $R_{h,n+1}$ are calculated with the predicted values and then used to correct these values,

$$\begin{aligned}
\vec{u}_{n+1} &= \vec{u}^{\star}_{n+1} + 0.5\delta t(\vec{R}_{u,n+1} - \vec{R}_{u,n}), && (4.70)\\
S_{n+1} &= S^{\star}_{n+1} + 0.5\delta t(S^{\star}_{n+1} R_{S,n+1} - S_n R_{S,n}), && (4.71)\\
A_{n+1} &= A^{\star}_{n+1} + 0.5\delta t(A^{\star}_{n+1} R_{A,n+1} - A_n R_{A,n}), && (4.72)\\
h_{n+1} &= h^{\star}_{n+1} + 0.5\delta t(h^{\star}_{n+1} R_{h,n+1} - h_n R_{h,n}). && (4.73)
\end{aligned}$$

This time-stepping scheme breaks the conservation of ice volume at particle level, which is preserved by the evolution equations (4.4), (4.9) and (4.10). However, the artificial change in ice volume over time scales on the order of days is negligible (Fig. 4.1). An estimation of this change is presented in the Appendix B.

In the simulations with the viscous-plastic rheology, the stress and strain rate fields are characterized by spurious checkerboard patterns when the time step exceeds a certain limit. There is an alternation of regions of convergent flow, where stress magnitudes are large (of the order of P_{HS}), and highly divergent flow with low shear, where the stress magnitudes are low. Consequently, the internal force

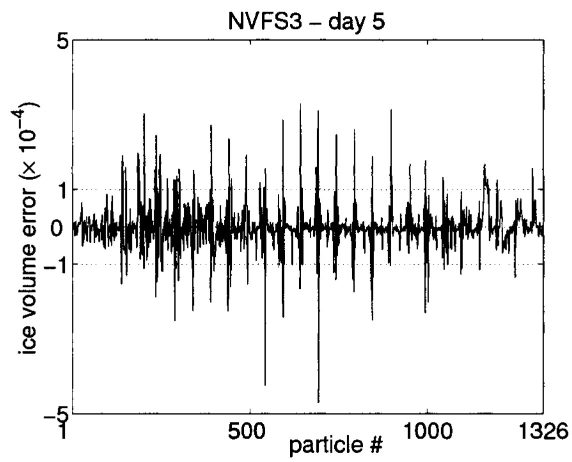

Figure 4.1: Particle ice volume error ($E = \frac{V_{day5} - V_0}{V_0}$) after 5 days, in NVFS3.

may have an unrealistically large contribution to the local momentum balance expressed by (4.17), of the order $O\left(\frac{P_{HS}}{\rho h \xi}\right)$, and may thus become a driving force. This can sometimes lead to unphysical situations; a realistic situation of a particle being accelerated only by the internal forces is when these forces result from the differential movement of the neighbouring particles, in the absence of external forces acting upon the particle.

We start our search for a time step limit by stating that unphysical situations may occur when the internal force acting on a particle does positive work, increasing the kinetic energy of the particle. Therefore, we require that this work (per unit time) must be less than the (positive) rate of change of the kinetic energy of the particle, which means that there are also other (driving) forces contributing to the increase in kinetic energy. Expressed per unit mass, this condition becomes

$$\frac{1}{\rho h}\overline{\nabla \cdot \boldsymbol{N}^e} \cdot \vec{u} < \frac{d\bar{\vec{u}}}{dt} \cdot \vec{u} \tag{4.74}$$

Using typical magnitudes, and dividing through by U (typical velocity) we get

$$\frac{P_{HS}}{\rho h \xi} < \frac{\delta U}{\delta t}, \tag{4.75}$$

or, equivalently,

$$\delta t < \frac{\rho h \xi \delta U}{P_{HS}}. \tag{4.76}$$

To eliminate δU from (4.76), we first write

$$P_{HS} \sim P^{yield} = 2\Delta\zeta \sim \dot{\epsilon}_{kk}\zeta \sim \frac{\delta U}{\xi}\zeta, \tag{4.77}$$

and then substitute for P_{HS} in that inequality. We thus obtain

$$\delta t < \rho h \frac{\xi^2}{\zeta}. \tag{4.78}$$

Interestingly, the proportionality of the time step limit (given by the right hand side of (4.78)) to $\frac{\xi^2}{\zeta}$ is not unlike the one mentioned in Hunke and Zhang (1999) for the explicit discretization of the viscous-plastic equations of Hibler (1979). This limit is also very similar to the viscous time scale of Hunke and Dukowicz (1997), in which the finite difference grid spacing replaces the smoothing length ξ.

For a maximum bulk viscosity, $\zeta_{max} = 10^7 P^{yield}$ (in $kg\ s^{-1}$), $\xi = O(10^4\ m)$ and $\rho h = O(10^3\ kg\ m^{-2})$, we get the following limiting condition for the time step (in seconds):

$$\delta t < \frac{10^4}{P^{yield}}. \tag{4.79}$$

Now, for $h \sim 1\ m$, $A \sim 0.9$ and $\lambda = 20$, we obtain $hAe^{-\lambda(1-A)} \sim 0.9/e^2 \sim 0.1$, and $P^{yield} \sim 0.1P^*$. It follows that

$$\Delta t < 10^5/P^* \sim 10\ s, \tag{4.80}$$

for $P^* = O(10^4\ N\ m^{-2})$. This limit has offered a very good prediction of the upper bound of the time step range, for which simulations free of spurious patterns have been obtained in the experiments with variable and parameter values on the orders of magnitude mentioned above.

4.3.3 Rigid boundaries

Various methods have been proposed in the SPH literature to deal with rigid boundaries, most of which rely on the estimation of contact/repulsive forces along the boundary (e.g. Gutfraind and Savage, 1997b; Lindsay and Stern, 2004; Kulasegaram et al., 2004). For instance, Lindsay and Stern (2004) implement a no-slip coastal boundary by means of stationary cells with given area and thickness (10 m). Moreover, to ensure that their moving cells do not penetrate the coast represented by the fixed cells, they introduce repulsive forces along the coastline. In SPICE, we have tried to represent the effect of the rigid boundaries in a simple and natural manner. Thus, to simulate the effect of no-slip boundaries we place stationary SPH particles along such boundaries, which can represent sea ice anchored to land (fast ice). A stationary particle fully participates in the calculations and only differ from a regular SPH particle by not updating its velocity and position. The internal forces that developed in the vicinity of the solid boundary in the simulations with our model were found to be sufficient to keep the SPH particles from penetrating it, making the use of repulsive forces unnecessary. A slightly more complicated scheme was used to implement slip boundaries, but we do not give details here, simply because such boundaries are not realistic for sea ice dynamics. We have only used them in one set of experiments, to make the comparison with previously published results presented in the next section.

4.4 Test case simulations

The test problem of Flato (1993), used by this author to evaluate the skill of his particle-in-cell (PIC) sea ice model in simulating the position of the ice edge and the Lagrangian transport of quantities such ice thickness, has been used to test SPICE with the two rheologies described in the previous section. The initial conditions of this test case specify the state of an ice pack as being at rest and having a uniform ice fraction, $A = 0.9$ (this value is identical to that used by Morland and Staroszczyk (1998) in their tests), and thickness, $h = 1\ m$, and covering a rectangular portion of an ocean at rest of size 500 $km \times 250\ km$. Rigid boundaries (represented by the dashed lines in Fig. 4.2) are placed along three of the sides of the rectangle.

The ice pack is then forced by a counter-clockwise vortex geostrophic wind field that does not vary in time, given by

$$\vec{V_g}(\vec{r}) = \min\left\{\omega R, \frac{\chi}{R}\right\}\vec{k} \times \frac{\vec{r}-\vec{r_c}}{R}, \tag{4.81}$$

where $\vec{r_c}$ is the position vector of the vortex centre (located at a distance of 50 km off the initial location of the free edge of the ice cover), $R = |\vec{r} - \vec{r_c}|$, $\omega = 0.5 \times 10^{-3}\ s^{-1}$, $\chi = 8 \times 10^5\ m^2\ s^{-1}$, and $\vec{k}$ is a unit vector parallel and opposite to the local gravity acceleration vector. The wind speed calculated with (4.81) increases linearly with the distance R from the vortex centre, from zero to a maximum of $20\ m\ s^{-1}$, reached when $R = 40\ km$, and then decreases as $1/R$.

The wind and water stresses that appear in the momentum equation (4.17) are calculated using the linear drag laws

$$\vec{\tau^a} = C_a(cos\psi_a + sin\psi_a\vec{k}\times)\vec{V_g}, \tag{4.82}$$

$$\vec{\tau^w} = C_w(cos\psi_w + sin\psi_w\vec{k}\times)(\vec{V_w} - \vec{u}), \tag{4.83}$$

where $\vec{V_w}$ is the geostrophic ocean current velocity, $\vec{u}$ is the pack ice velocity. The wind and water drag coefficients are taken to be constant and their values are, $C_a = 0.0126\ kg\ m^{-2}\ s^{-1}$ and $C_w = 0.6524\ kg\ m^{-2}\ s^{-1}$, respectively. A value of 25° is assigned to both the air and water drag turning angles, ψ_a and ψ_w. The ocean is assumed to remain still throughout the simulation, hence $\vec{V_w}$ is set equal to zero. In addition, the surface tilt and Coriolis terms are neglected in (4.17).

The ridging function $\alpha(A)$ is taken to be identical to that proposed by Morland and Staroszczyk (1998), which is defined by

$$\alpha(A) = \begin{cases} \frac{A-A_c}{1-A_c}, & \text{when } 0 < A_c < A < 1, \\ 0, & \text{when } 0 \le A \le A_c. \end{cases} \tag{4.84}$$

According to (4.84), ridging only takes place when the ice fraction exceeds a prescribed critical value, A_c. Moreover, for $A > A_c$, α increases with A, up to a maximum value of 1.

In all of the experiments reported herein, the pack ice cover consists of a number of 1326 (51×26) particles whose shapes and areas change continuously. These particles are obtained by dividing up the initial cover into squares of size 10 $km \times$ 10 km; the centroids of the particles form a rectangular grid with a spacing of 10 km. Unless specified otherwise, both our results and those that these are compared with have been obtained after 5 days of integration from rest. Note also that in the plots presented hereinafter, the centres of the dots are defined by the position vectors associated with the corresponding particles.

4.4.1 Simulations with the nonlinear viscous rheology of Morland and Staroszczyk

In this section, we present results of four experiments with SPICE using the nonlinear viscous rheology of MS and compare them with those obtained by MS with a more complex Lagrangian finite element (FE) model. The experiments are denoted NVFS1, NVFS2, NVFS3, NVNS1, where the prefix NV stands for nonlinear viscous, the next two letters indicate the type of boundary (FS for free slip, NS for no-slip), and the last digit is associated with the value of the parameter β_c. The values of the constants and parameters used in these simulations are given in Table 4.1; the ones used in NVFS1 and NVNS1 are identical to those of MS. Note that MS only implemented free slip boundary conditions in their model.

Of major interest is the ability of SPICE to simulate the location of the free sea ice edge. The differences among the free edge locations after 5 days in the four simulations are indistinguishable, and this can be readily seen in Figs. 4.2 and 4.3, for three of them. In addition, these locations are in very good agreement with the those simulated by Morland and Staroszczyk (1998) and Flato (1993), not shown here. We conclude that, as with the Lagrangian FE and the PIC models, our particle-based model can handle very large deformations as those characterizing the MIZ and has the ability to accurately predict the sea ice edge position. This is one of the much sought-after capability of a sea ice model, especially for one meant to be used for sea ice forecasting (e.g. Pritchard et al., 1990; Flato, 1993; Van Woert

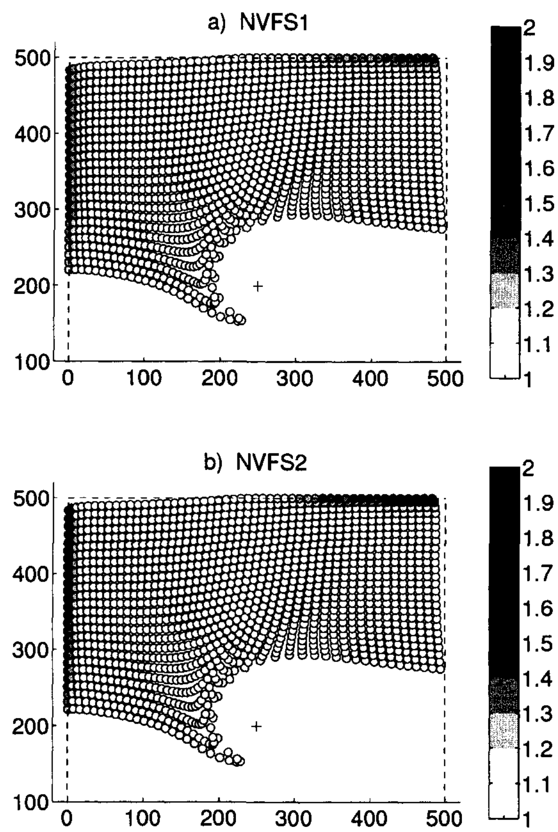

Figure 4.2: Pack ice thickness (in m) after 5 days in a) NVFS1 and b) NVFS2. Distances along the axes are in km.

Table 4.1: Constant and parameter values used in the experiments with the nonlinear viscous rheology of Morland and Staroszczyk.

Name	Symbol	Value	Experiment
sea ice density	ρ	$910\ kg\ m^{-3}$	all
smoothing length constant	κ	1.2	all
critical ice fraction	A_c	0.5	all
max. compressive strength	σ^*	$2.75 \times 10^4\ N\ m^{-2}$	all
sine of limit friction angle	ϕ_s^*	0.5	all
bounding curve parameter	n	1.5	all
ice strength parameter	λ	20	all
divergence magnitude	β_c	$10^{-5}\ s^{-1}$	NVFS1, NVNS1
		$3 \times 10^{-5} s^{-1}$	NVFS2
		$10^{-6}\ s^{-1}$	NVFS3
time step	δt	$300\ s$	NVFS1, NVNS1, NVFS2
		$60\ s$	NVFS3

et al., 2004) for navigation and offshore operations.

Of no less importance is the accurate prediction of the sea ice thickness and concentration (ice fraction), throughout the ice cover. The thickness field obtained in NVFS1 shows similarities to that of Morland and Staroszczyk (1998) consisting in the localization of the thickness build-up in narrow regions adjacent to the rigid boundaries (Fig. 4.2(a)). However, our maximum thickness values along the left and upper boundaries (as they appear in Fig. 4.2) only slightly exceed $1.5\ m$ (see also Fig. 4.4) and $1.4\ m$, respectively. These are lower than the values predicted by MS, which are slightly larger than $1.8\ m$ and $1.6\ m$, respectively. The thickness magnitude difference most likely reflects differences in the β values in the boundary layers. This may stem from the different numerical methods used but it can also be related to the resolution offered by the models in the viscous boundary layers, as well as to the way the effect of the free-slip boundary is taken into account.

Interestingly, the experiment with no-slip boundaries (NVNS1) provided maximum thickness values that are very close to those predicted in NVFS1 (Fig. 4.4). This is the effect of having very similar magnitudes of convergence in the boundary

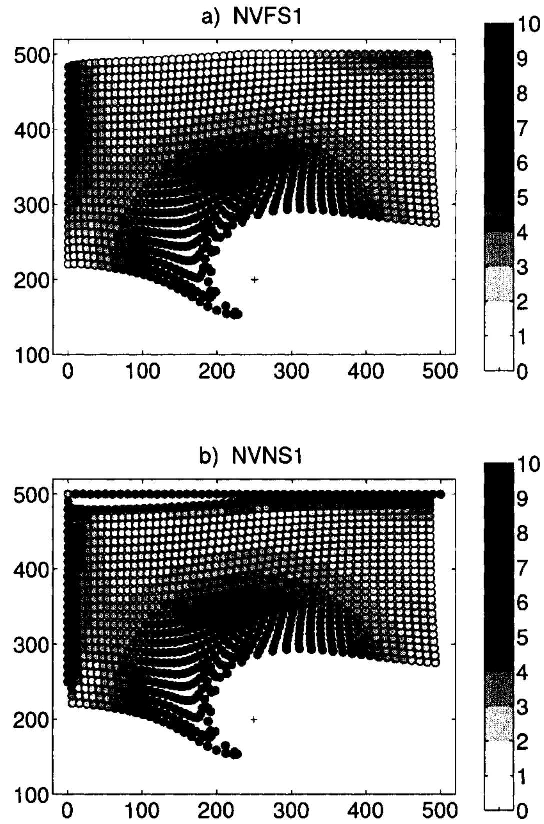

Figure 4.3: Maximum shear strain rate ($\times 10^{-7}\ s^{-1}$) after 5 days in a) NVFS1 and b) NVNS1. Distances along the axes are in km.

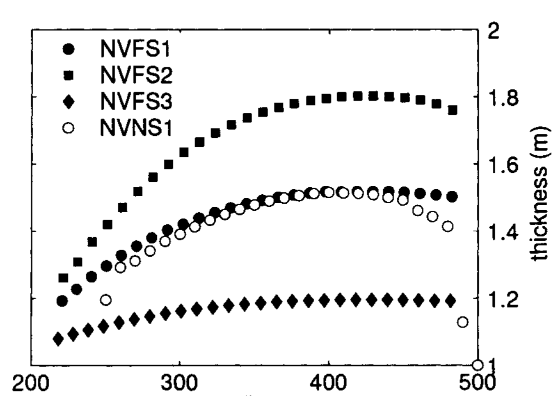

Figure 4.4: Particle thickness along the left boundary of the domain, after 5 days, in the experiments with nonlinear viscous rheology.

layers in these runs, despite the very large dissimilarities observed in the maximum shear fields in the same areas (Fig. 4.3). The explanation lies in the similarity of the bulk viscous response along the boundaries, which is transmitted to the mechanical pressure gradients via (4.31).

A very good agreement with the thickness fields predicted by MS has been obtained in NVFS2 (Fig. 4.2(b)), in which β_c is increased. The fact that β_c is one order of magnitude larger than the typical β magnitudes obtained in the boundary layers in both NVFS1 and NVFS2 means that it plays a dominant role in setting the ϕ_b (Eq. 4.32) values, with little contribution from the local β. Therefore, the higher is β_c, the lower are the bulk viscous response of the ice pack and the mechanical pressure gradients. The result is an increased convergence in the vicinity of the rigid boundaries. Consequently, the ridging term that appears in the thickness equation will have larger values in convergent flow and this will lead to higher rates of change of thickness.

One may now wonder if prescribing a β_c value on the order of the typical β would have a significant impact on the simulations. We have performed such an experiment, NVFS3, taking $\beta_c = 10^{-6}\ s^{-1}$. As expected, following our explanation of the high sensitivity of the thickness field to the bulk viscous response function ϕ_b, a decrease in β_c is accompanied by smaller thickness build-up in the boundary layers in NVFS3 (Fig. 4.4). More interesting if the fact that now the bulk viscous response of the pack will exhibit an increased variation with β and will generally have higher values. As a result, a stiffer ice pack is simulated (as a more viscous fluid) near the solid boundaries, where the flow is convergent. Therefore, increased mechanical pressure gradients occur, now spreading over larger distances away from the rigid boundaries. This leads to a less convergent flow in these boundary layers due to increased resistance to compression. This situation required a five-fold reduction in time step to avoid the occurrence of spurious patterns similar to those mentioned in the time integration section.

A very important feature of SPICE is that, as long as ridging does not take place (i.e. when $\alpha = 0$), it conserves the particle thickness both in the continuum (Eq. 4.10) and the discrete formulation (Eqns. 4.68 and 4.73). In this case, the Lagrangian transport of sea ice thickness (as a passive tracer) is not altered by numerical diffusion and a sharp sea ice edge is simulated. This is very difficult to obtain with grid-based or grid-assisted models as numerical diffusion plagues even the least diffusive Eulerian advection schemes tested in a sea ice dynamics context (e.g. Merryfield and Holloway, 2003; Hutchings, 2000), as well as the simulations with the Flato's PIC model (Flato, 1993). When thickness diffusion occurs along the free ice edge, the thickness is artificially reduced near the edge. Therefore, when a thermodynamic component is added to the model, it takes less time for sea ice to completely melt in this region than it would in a model that does not diffuses the thickness. The effect is a reduced accuracy of the ice edge prediction in the former model.

The maximum shear strain rate (γ) fields obtained in the four experiments exhibit a pattern typical to viscous fluids, with shear deformation localized in boundary layers along the rigid boundaries (Fig. 4.3). As expected, increased shear deformation is simulated in the experiment with no-slip boundaries (Fig. 4.3(b)). High shear deformation is also observed in the region closest to the vortex centre, where the gradient in the wind field is highest. Here, however, the rheology plays a much reduced role because the flow becomes mostly divergent as sea ice is pushed offshore by the wind. No shear deformation localization has been observed in the interior of the pack ice cover in any of our experiments, and this signals a potential inability of the rheology of MS to capture the development of LKFs.

4.4.2 Simulations with the viscous-plastic rheology of Hibler and Schulson

Three numerical experiments have been performed with the viscous-plastic rheology of HS, all of them with no-slip boundaries, to investigate whether SPICE can simulate the development of LKFs with this rheology. The values of the constants and parameters used in these experiments are given in Table 4.2.

Table 4.2: Constant and parameter values used in the experiments with the viscous-plastic rheology of Hibler and Schulson.

Name	Symbol	Value	Experiment
sea ice density	ρ	$910\ kg\ m^{-3}$	all
smoothing length constant	κ	1.2	all
critical ice fraction	A_c	0.5	all
axes ratio	e	1.3846	all
max. compressive strength of sea ice	P^*	$2.75 \times 10^4\ Nm^{-2}$	all
sea ice strength parameter	λ	20	all
combined strain rate threshold	Δ_c	$5 \times 10^{-8}\ s^{-1}$	VPNS1
		$5 \times 10^{-7}\ s^{-1}$	VPNS2
		$5 \times 10^{-6}\ s^{-1}$	VPNS3
time step	δt	$5\ s$	VPNS1
		$15\ s$	VPNS2
		$100\ s$	VPNS3

We have performed a first experiment, VPNS1, by setting $\Delta_c = 5 \times 10^{-8}\ s^{-1}$. This allowed the ice pack to be in a state of plastic yielding almost everywhere. This situation corresponds to the critical state hypothesis (Overland et al., 1998), which has been validated by stress measurements (e.g. Coon et al., 1993). For this Δ_c value we get $\zeta_{max} = 10^7 P^{yield}$. As shown in section 4.3.2, an estimate for the maximum time step in this case is $10\ s$.

Unlike the shear deformation patterns simulated with the nonlinear viscous rheology (Fig. 4.3), those obtained in VPNS1 (Fig. 4.5) show the occurrence of regions with localized and intense shear deformation in the interior of the ice pack. Figure 4.5 (left column) shows how shear bands initiate and evolve. The most pronounced feature is the shear band that extends across the domain from the high-shear region near the vortex centre to the upper boundary, where the development of a crack is mimicked as particles move away from the boundary. This shear band (that will be referred to as SB1) is not a static feature, but it is displaced to the left by the moving particles. Note the counter-clockwise rotation of the particles about the particles forming the centreline of SB1 that shows the tendency of this band for contraction. The plot of the particle displacement vectors (Fig. 4.6(a)) shows regions of quasi-uniform motion (also visible in the velocity plot in Fig. 4.6(b)) that could be viewed as particle aggregates. It turns out that this shear band constitutes the boundary between the central aggregate (moving to the left) and the one adjacent to it on the left (moving down and to the left because of the deformation of the wind field and the proximity to the left boundary), which explains the previously mentioned localized rotation.

A careful investigation of the evolution of SB1 in VPNS1 reveals that, at the beginning, the particles in this band experience shearing and dilation (Fig. 4.5(a)-4.5(d)). Because the flow is divergent, the corresponding stress states are represented by stress points that lie on the Coulombic portion of the yield curve. Additionally, the ridging term in (4.10) vanishes, hence thickness cannot increase within SB1. However, as the central aggregate continues to move to the left, an increasing number particles in SB1 start undergoing convergence (Fig. 4.5(f) and 4.5(h)). Therefore, thickness can now increase in SB1, and does increase in this simulation, but very little because convergence is weak. Nonetheless, this shows that SPICE is able to simulate the complex dynamics of some LKFs where pack ice initially undergoes shearing and opening (Pritchard, 1988), then pure shear, and eventually shearing and closing (accompanied by ridging and strengthening). A particle going through these stages will have its stress state represented by a point that will move along the yield curve from the Coulombic portion to the elliptic portion.

We have seen that SPICE with the HS rheology is able to simulate localized deformation in ice packs and motion of aggregates, for low values of the plastic regime threshold (Δ_c) that cause pack ice to yield plastically almost everywhere. What happens if Δ_c is increased so that there is a significant number of particles with sub-yield (viscous) stress states? The γ field obtained in two experiments, VPNS2 and VPNS3, in which Δ_c takes on values that are one order and two orders of magnitude larger than that used in VPNS1, respectively, are shown in Fig. 4.7.

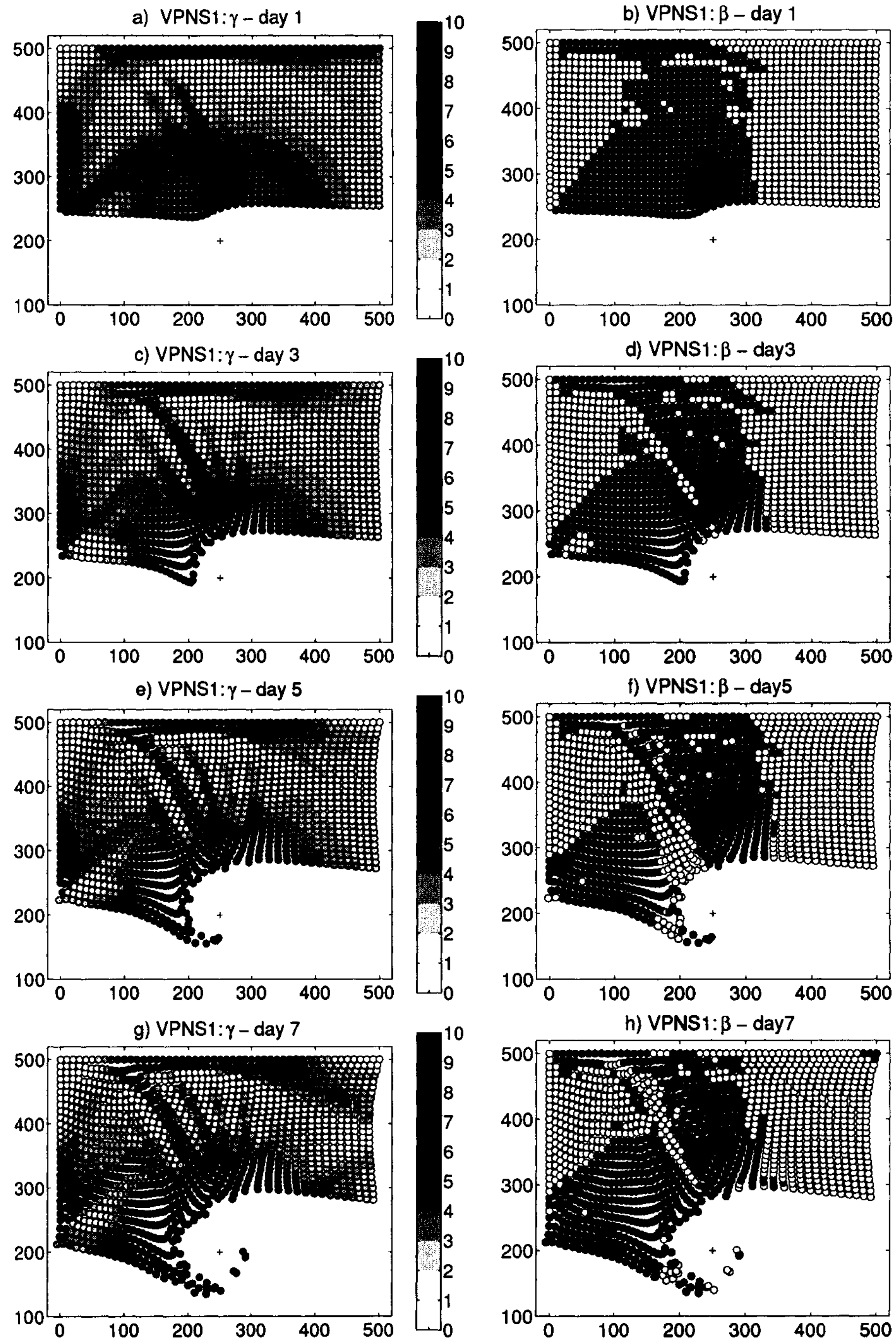

Figure 4.5: Maximum shear strain rate ($\times 10^{-7}\ s^{-1}$) in VPNS1 after a) 1 day, c) 3 days, e) 5 days, and g) 7 days. The plots in right column show where the dilation occurs, at the same times. Black indicates divergent flow, whereas white indicates convergence.

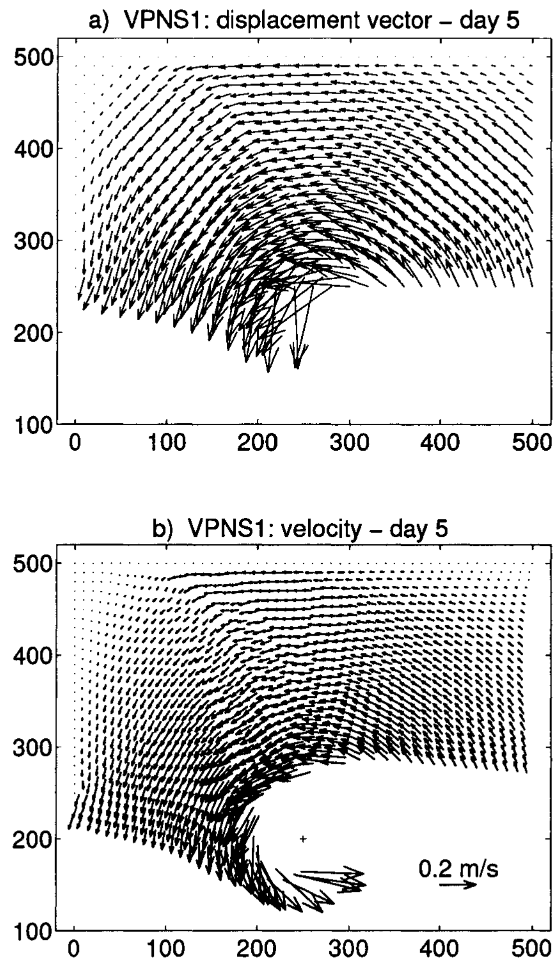

Figure 4.6: Displacement vectors (plotted for every other particle) and velocity vectors after 5 days, in VPNS1. Distances along the axes are in km.

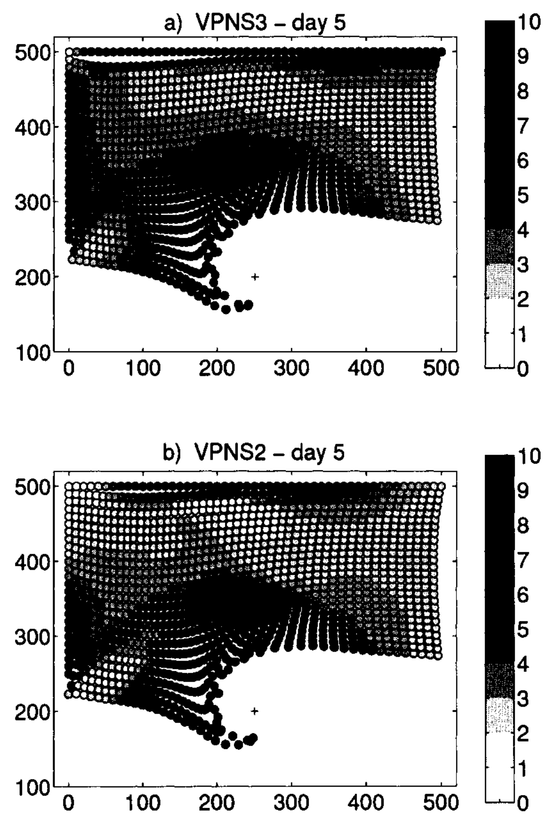

Figure 4.7: Maximum shear strain rate ($\times 10^{-7}\ s^{-1}$) after 5 days in a) VPNS3 and b) VPNS2. Distances along the axes are in km.

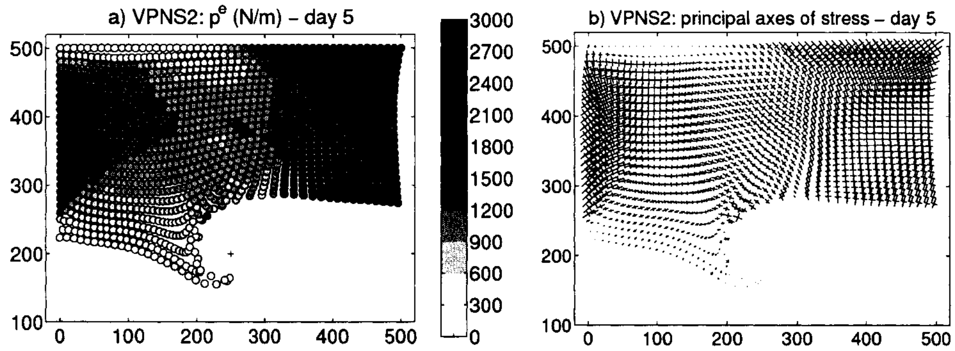

Figure 4.8: a) Depth-integrated mechanical pressure (in $N\ m^{-1}$) and b) principal axes of stress after 5 days in VPNS2. The length of each principal axis is proportional to the magnitude of the corresponding principal stress. Distances along the axes are in km.

After 5 days, $\Delta < \Delta_c$ almost everywhere in VPNS3, indicating a viscous behaviour. There is no sign of shear localization in the γ field (Fig. 4.7(a)). The simulation of a viscous flow explains the strong resemblance of this γ pattern to that produced in NVNS1 (Fig. 4.3(b)).

There are many more particles with pack ice in the plastic regime ($\Delta > \Delta_c$) in VPNS2, including interior particles, away from the boundary layers. A shear band develops (Fig. 4.7(b)) at the boundary between the particles that feel the compression against the left boundary (Fig. 4.8), thus experiencing relatively high mechanical pressure gradients (Fig. 4.8(a)), and those in the region below, whose motion is much less confined. Also visible in Fig. 4.7(b) is a weak tendency of the shear deformation to intensify along the direction of the most pronounced LKF produced in VPNS1 (Fig. 4.5(e)). Overall, however, the localization of the shear deformation in the interior of the ice pack is weaker in VPNS2. Moreover, the discontinuities observed in the displacement fields in VPNS1, marking boundaries of particle aggregates, are less pronounced in VPNS2. It thus seems that the simulations with SPICE using the HS rheology are more realistic when pack ice is yielding plastically almost everywhere, and this may also be the case for other viscous-plastic rheologies. Further investigation will probably clarify this issue.

The differences among the locations of the sea ice edge predicted in the experiments with the HS rheology after 5 days (Figs. 4.5(e) and 4.7) are very small. These locations differ from those predicted by SPICE with the MS rheology in the highly deformed zone found in the proximity of the vortex centre, as well as near the left boundary. Here, there are particles in the runs with the HS rheology that slip past the lowest fixed particle of the left boundary (Fig. 4.6(b)).

The reason why we limited the length of left boundary to the initial extent of the sea ice cover along that side in the experiments with the viscous-plastic rheology, was to allow pack ice to move freely to the left, past its southern end. This has triggered the development of the shear band extending from this end towards the interior in VPNS1 and VPNS2. The region located below it is characterized by reduced compressive stresses relative to the surrounding pack ice (Fig. 4.8), and plays a minor role in transmitting compressive load from the central region of the ice-covered domain towards the left boundary. Consequently, an effect somewhat similar to arching is simulated as this load is transmitted mainly through the pack ice situated above this region (Fig. 4.8(b)). Future work will address the ability of the model to simulate arching effects in narrow straits.

Compared to the simulations with the nonlinear viscous rheology, those with the viscous-plastic rheology produced lower convergence values near the rigid boundaries, hence a reduced thickness build-up along these boundaries (Fig. 4.9). This a consequence of simulating a stiffer ice pack (with larger bulk viscosities) and increased mechanical pressure gradients in the latter experiments. Also worth noting is that that there is more sea ice build-up along the lower half of the left boundary in VPNS1 and VPNS2, whereas the opposite is true in the rest of the experiments (in which pack ice has a viscous behaviour).

The plots of the pack ice thickness, ice fraction and compressive strength (P^{yield}) obtained in VPNS1 after 5 days are shown in Fig. 4.10. The ice fraction of the particles that have experienced mostly divergent flow has decreased (from the initial value of 0.9). Readily visible are its relatively low values in SB1 as well as in

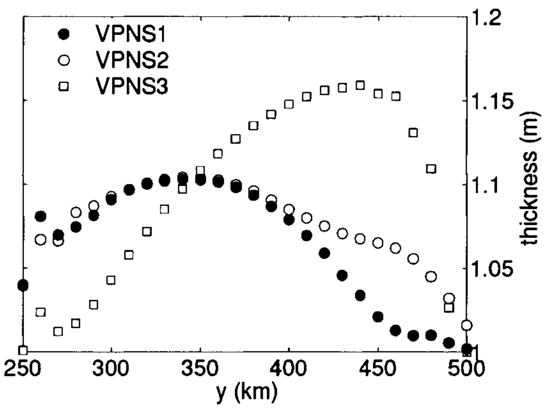

Figure 4.9: Particle thickness along the left boundary of the domain after 5 days, in the experiments with the viscous-plastic rheology.

the next shear band situated to the right of it, which caused pack ice to weaken (Fig. 4.10(c)); we remind the reader that thickness has only very slightly increased there. The regions where pack ice weakens will very likely have a significant impact on the initiation and propagation of LKFs at a later time (e.g. Hutchings et al., 2005). Note that unlike the experiments of Hutchings et al. (2005), the ice pack had an initial uniform strength in ours. Regarding the advection of patterns of weak pack ice, a Lagrangian model (e.g. SPICE) has the advantage of carrying the compressive strength information through h and A, whose values are normally better preserved at particle level in such models than they are in Eulerian models.

The simulation of the LKFs is very sensitive to the local smoothing length. Fewer LKFs have been obtained in experiments in which κ was increased. This effect is not surprising because larger smoothing lengths translate into decreased spatial resolution. Since the smoothing length can only be decreased up to a certain limit in SPH-based models, the refinement of the resolution is usually achieved by inserting new particles in areas where high gradients occur. This should normally lead to narrower shear bands and a better representation of pack ice in highly divergent areas (e.g. ice edge). To prevent the number of the particles from becoming very large, some particles could be then removed from areas with low gradients in the prognostic variables and forcing.

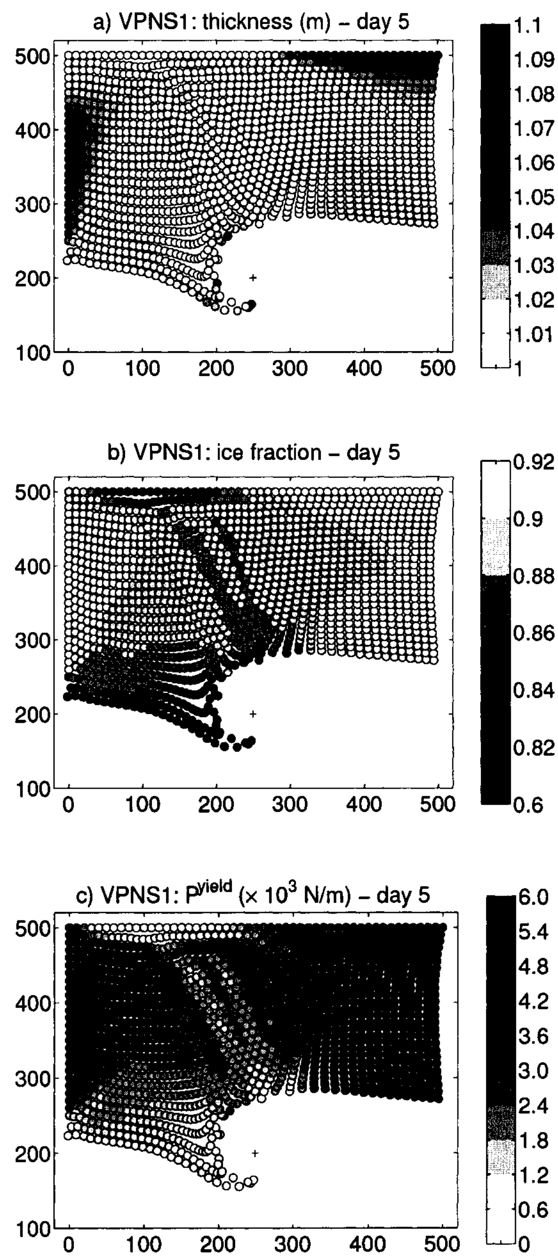

Figure 4.10: Pack ice thickness (in m) (a), ice fraction (b), and compressive strength, P^{yield} (in $\times 10^3$ N m^{-1}) (c) in VPNS1, after 5 days. Distances along the axes are in km.

Two particles (located at the left end of the crack developing by the upper boundary) have been identified in the VPNS1 as having negative values of mechanical pressure, which indicates tension (allowed by the HS rheology). This has not caused any problems in that simulation. Cracks should naturally occur as particles move apart. However, this situation could lead to instabilities in Eulerian models.

The size of the time step in our simulations with the HS rheology is much greater than that used in the explicit time integration of Eulerian models with the same rheology and a similar resolution. As an example, Hutchings et al. (2005) used a time step of 1×10^{-4} s for a resolution of 10 km. This aspect is definitely worth further investigation given its impact on the computational cost.

The VPNS1 simulation has been computationally expensive, requiring about 80 min. of CPU time per model day, on an AlphaServer DS20E. This cost can be greatly decreased by implementing a search algorithm for finding the particles within a certain radius from a given particle, and then only use the values they carry to update the information carried by that particle. Most SPH models rely on such algorithms to speed up the simulations, and one has to be implemented in SPICE before adding a thermodynamic component and configuring it for a specific geographical region.

4.5 Summary and conclusions

This paper presents a new particle model for sea ice dynamics, SPICE, that has no underlying computational grid. An arbitrary model particle represents the same patch of pack ice throughout the simulation. As in Gray and Morland (1994), pack ice is treated as a mixture of ice and lead water. The equation introduced for the evolution of the horizontal area of the particle, along the evolution equations for ice fraction and thickness, ensures that the ice volume of the particle is conserved. The momentum equation takes into account the change in its inertia as water is exchanged with the underlying ocean in convergent/divergent flow.

The numerical integration of the model relies on a corrected Smoothed Particle Hydrodynamics (SPH) technique for the computation of the spatial derivatives. The method of Bonet and Lok (1999) of calculating corrected kernel functions and their gradients, and a variable smoothing length are used for improved accuracy of the SPH estimates. An explicit scheme is used for the time integration, and we propose a method of estimating its maximum time step. The rigid boundaries are represented by fixed particles, without the need of artifacts, such as repulsive forces.

Results from a series of experiments performed to test the particle model with two different rheologies, in an idealized case of an ice pack with a free edge driven by a vortex wind are presented. The nonlinear viscous rheology of Morland and Staroszczyk (1998) governs the mechanical behaviour of pack ice in the first set of simulations that are compared with simulations with a more complex Lagrangian finite element model. The predicted locations of the free ice edge compare very well, whereas SPICE predicts a reduced ice build-up near the solid boundaries. Deformation localization in the interior of the ice pack – an ubiquitous feature in the observed large-scale deformation of ice packs – does not occur in any of the simulations with this rheology.

In the second set of experiments, SPICE has been tested with the viscous-plastic rheology of Hibler and Schulson (2000). In agreement with previous studies, we have found that the development of linear kinematic features as narrow bands of intense shearing that separate regions with quasi-uniform motion (aggregates) can be simulated with this rheology. An increased number of such features and more pronounced discontinuities in the displacement field along aggregate boundaries have been obtained in the experiment in which pack ice was in a state of plastic yielding almost everywhere. Novel is the simulation of shear banding in an ice pack with a Lagrangian sea ice model using a viscous-plastic rheology. The shear bands can be tracked as the particles move, and SPICE captures the transition from shearing and opening to shearing and closing, when aggregates that initially moved apart start approaching each other.

The thickness of an arbitrary particle is carried by that particle and its transport is not plagued by spurious diffusion, as it is in grid-based models. Because the particle thickness can only change through ridging in SPICE (thermodynamic processes are neglected), the simulated sea ice edges are not eroded by thickness diffusion.

The results from the experiments with the viscous-plastic rheology show that SPICE is able to simulate complex sea ice dynamics. However, more work needs to be done to improve this model. The accuracy of the simulations is strongly influenced by that of the SPH estimates, which in turn depends both on the particle distribution and the kernel used. Reliable long-term simulations in realistic cases will only be possible when SPICE is capable of adapting its spatial resolution by adding/removing particles, as needed. Further work will address this aspect as well as others, such as ridging schemes and the incorporation of a thermodynamic component.

Bibliography

Alexeev, V., I. Lavrenov, and V. Smirnov, 2003: Estimation of the internal friction angle in sea ice cover. *Geophys. Res. Abstr.*, **5**, 13195.

Belytschko, T., Y. Krongauz, D. Organ, M. Fleming, and P. Krysl, 1996: Meshless methods: An overview and recent developments. *Comp. Meth. Appl. Mech. Engrg.*, **139**, 3–47.

Benz, W.: 1990, Smooth particle hydrodynamics: A review. in *The numerical modelling of nonlinear stellar pulsations*, edited by J. R. Buchler, Kluwer Academic Publishers, Dordrecht, The Netherlands, 269–288.

Bonet, J. and T. S. L. Lok, 1999: Variational and momentum preservation aspects of Smooth Particle Hydrodynamic formulations. *Comp. Meth. Appl. Mech. Engrg.*, **180**, 97–115.

Connolley, W. M., J. M. Gregory, E. Hunke, and A. J. McLaren, 2004: On the consistent scaling of terms in the sea-ice dynamics equation. *J. Phys. Oceanogr.*, **34**, 1776–1780.

Coon, M. D., G. S. Knoke, D. C. Echert, and R. S. Pritchard, 1998: The architecture of an anisotropic elastic-plastic sea ice mechanics constitutive law. *J. Geophys. Res.*, **103**, 21915–21925.

Coon, M. D., G. S. Knoke, D. C. Eckart, and H. L. Stern: 1993, Contemporaneous field measurements of pack ice stress and ice strain measurements from SAR imagery. paper presented at *Oceans '93*, Inst. of Electr. and Electron. Eng., Victoria, BC, Canada.

Coon, M. D., G. A. Maykut, R. S. Pritchard, D. A. Rothrock, and A. S. Thorndike, 1974: Modeling the pack ice as an elastic-plastic material. *AIDJEX Bull.*, **24**, 1–106, Univ. of Washington, Seattle.

Drinkwater, M. R. and V. A. Squire, 1989: C-band SAR observations of marginal ice zone rheology in the Labrador Sea. *IEEE Trans. Geosc. Rem. Sens.*, **27**, 522–534.

Flato, G. M., 1993: A particle-in-cell sea-ice model. *Atmos.-Ocean*, **31**, 339–358.

Gingold, R. A. and J. J. Monaghan, 1977: Smoothed particle hydrodynamics: Theory and application to non-spherical stars. *Mon. Not. R. Astron. Soc.*, **181**, 375–389.

Gray, J. M. N. T. and L. W. Morland, 1994: A two-dimensional model for the dynamics of sea ice. *Phil. Trans. R. Soc. Lond.* A, **347**, 219–290.

Gutfraind, R. and S. B. Savage, 1997a: Marginal ice zone rheology: Comparison of results from continuum-plastic models and discrete-particle simulations. *J. Geophys. Res.*, **102**, 12647–12661.

— 1997b: Smoothed particle hydrodynamics for the simulation of broken-ice fields: Mohr-Coulomb-type rheology and frictional boundary conditions. *J. Comp. Phys.*, **134**, 203–215.

Heil, P. and W. D. Hibler, 2002: Modeling the high-frequency component of Arctic sea ice drift and deformation. *J. Phys. Oceanogr.*, **32**, 3039–3057.

Hibler, W. D., 1977: A viscous sea ice law as a stochastic average of plasticity. *J. Geophys. Res.*, **82**, 3932–3938.

— 1979: A dynamic thermodynamic sea ice model. *J. Phys. Oceanogr.*, **9**, 815–846.

— 2001a: Modeling the formation and evolution of oriented fractures in sea ice. *Ann. Glac.*, **33**, 157–164.

— 2001b: Sea ice fracturing on the large scale. *Eng. Frac. Mech.*, **68**, 2013–2043.

Hibler, W. D. and E. M. Schulson, 2000: On modeling the anisotropic failure and flow of flawed sea ice. *J. Geophys. Res.*, **105**, 17105–17120.

Hopkins, M. A., S. Frankenstein, and A. S. Thorndike, 2004: Formation of an aggregate scale in Arctic sea ice. *J. Geophys. Res.*, **109**, C01032, doi:10.1029/2003JC001855.

Hunke, E. C. and J. C. Dukowicz, 1997: An elastic-viscous-plastic model for sea ice dynamics. *J. Phys. Oceanogr.*, **27**, 1849–1867.

Hunke, E. C. and Y. Zhang, 1999: A comparison of sea ice dynamics models at high resolution. *Mon. Wea. Rev.*, **127**, 396–408.

Hutchings, J. K., 2000: On modelling the mass of Arctic sea ice. Ph.D. thesis, University of London.

Hutchings, J. K., P. Heil, and W. D. Hibler, 2005: On modelling linear kinematic features in sea ice. *Mon. Wea. Rev.*, *in press*.

Hutchings, J. K., H. Jasak, and W. L. Seymour, 2004: A strength implicit correction scheme for the viscous-plastic sea ice model. *Ocean Modelling*, **7**, 111–133.

Kulasegaram, S., J. Bonet, R. W. Lewis, and M. Profit, 2004: A variational formulation based contact algorithm for rigid boundaries in two-dimensional SPH applications. *Comp. Mech.*, **33**, 316–325.

Kwok, R., 2001: Deformation of the Arctic Ocean sea ice cover: November 1996 through April 1997. in *Scaling Laws in Ice Mechanics and Dynamics*, edited by J. Dempsey and H. H. Shen, 315-323. Kluwer Academic, Dordrecht.

Li, S. and W. K. Liu, 2000: Numerical simulations of strain localization in inelastic solids using mesh-free methods. *Int. J. Numer. Meth. Engng*, **48**, 1285–1309.

Libersky, L. D., A. G. Petschek, T. C. Carney, J. R. Hipp, and F. A. Allahdadi, 1993: High strain Lagrangian hydrodynamics: A three-dimensional SPH code for dynamical material response. *J. Comp. Phys.*, **109**, 67–75.

Lindsay, R. W. and H. L. Stern, 2003: The RADARSAT geophysical processor system: Quality of sea ice trajectory and deformation estimates. *J. Atmos. Ocean. Tech.*, **20**, 1333–1347.

— 2004: A new Lagrangian model of Arctic sea ice. *J. Phys. Oceanogr.*, **34**, 272–283.

Lucy, L. B., 1977: A numerical approach to the testing of the fission hypothesis. *Astron. J.*, **82**, 1013–1024.

McNutt, S. L. and J. E. Overland, 2003: Spatial hierarchy in Arctic sea ice dynamics. *Tellus*, **55A**, 181–191.

Merryfield, W. J. and G. Holloway, 2003: Application of an accurate advection algorithm to sea-ice modelling. *Ocean Modelling*, **5**, 1–15.

Monaghan, J. J., 1992: Smoothed particle hydrodynamics. *Annu. Rev. Astron. Astrophys.*, **30**, 543–574.

— 2000: SPH without a tensile instability. *J. Comp. Phys.*, **159**, 290–311.

Morland, L. W. and R. Staroszczyk, 1998: A material coordinate treatment of the sea-ice dynamics equations. *Proc. R. Soc. Lond.* A, **454**, 2819–2857.

Overland, J. E., S. L. McNutt, S. Salo, J. Groves, and S. Li, 1998: Arctic sea ice as a granular plastic. *J. Geophys. Res.*, **103**, 21845–21867.

Overland, J. E. and C. H. Pease, 1988: Modeling ice dynamics of coastal seas. *J. Geophys. Res.*, **93**, 15619–15637.

Pritchard, R. S., 1988: Mathematical characteristics of sea ice dynamics models. *J. Geophys. Res.*, **93**, 15609–15618.

Pritchard, R. S., A. C. Mueller, D. J. Hanzlick, and Y.-S. Yang, 1990: Forecasting Bering Sea ice edge behavior. *J. Geophys. Res.*, **95**, 775–788.

Rabczuk, T. and T. Belytschko, 2004: Cracking particles: a simplified meshfree method for arbitrary evolving cracks. *Int. J. Numer. Meth. Engng*, **61**, 2316–2343.

Richter-Menge, J. A., B. C. Elder, J. E. Overland, and S. Salo: 1996, Relating Arctic pack ice stress and strain at the 10 km scale. in *Proceedings of the ACSYS Conference on the Dynamics of the Arctic Climate System*, edited by P. Lemke et al., WMO/TD Pub. 760, pp. 327-331, World Meteorol. Organ., Geneva.

Smith, R. B., 1983: A note on the constitutive law for sea ice. *J. Glaciol.*, **29**, 191–195.

Stern, H. L., D. A. Rothrock, and R. Kwok, 1995: Open water production in Arctic sea ice: Satellite measurements and model parameterizations. *J. Geophys. Res.*, **100**, 20601–20612.

Tartakovsky, A. M. and P. Meakin, 2005: A smoothed particle hydrodynamics model for miscible flow in three-dimensional fractures and the two-dimensional Rayleigh-Taylor instability. *J. Comp. Phys.*, **207**, 610–624.

Tremblay, L. B. and L. A. Mysak, 1997: Modelling sea ice as a granular material, including the dilatancy effect. *J. Phys. Oceanogr.*, **27**, 2342–2360.

Van Woert, M. L., C. Z. Zou, W. N. Meier, P. D. Hovey, R. H. Preller, and P. G. Posey, 2004: Forecast verification of the Polar Ice Prediction System (PIPS) sea ice concentration fields. *J. Atmos. Oc. Tech.*, **21**, 944–957.

Wang, L. R. and M. Ikeda, 2004: A Lagrangian description of sea ice dynamics using the finite element method. *Ocean Modelling*, **7**, 21–38.

Wang, Z. Q., Y. Lu, H. Hao, and K. Chong, 2005: A full coupled numerical analysis approach for buried structures subjected to subsurface blast. *Comp. Struct.*, **83**, 339–356.

Wilchinsky, A. V. and D. L. Feltham, 2004: A continuous anisotropic model of sea-ice dynamics. *Proc. R. Soc. Lond.* A, **460**, 2105–2140.

Chapter 5

General Discussion and Conclusions

This thesis presents contributions to the fields of ocean and sea ice modelling with application to the modelling of the subpolar North Atlantic Ocean. In the first part, it is shown that significantly improved simulations can be obtained with eddy-permitting z-level ocean models by carefully formulating and implementing parameterizations of the unresolved eddy-induced transport of tracers. Their use is justified by the fact that the eddy-permitting models do not fully resolve the mesoscale eddy field. Although such schemes may either over- or under-parameterize the effect of the unresolved mesoscale eddies, it has been found that they outperform the horizontal tracer diffusion schemes, which are still commonly used in the eddy-permitting regime. More realistic simulations have been obtained with eddy parameterizations employing a variable eddy transfer coefficient, mainly as a result of enhanced dispersal of water masses along isopycnal surfaces, combined with significantly decreased spurious mixing of tracers.

Equipping ocean models with appropriate parameterizations for the sub-grid tracer stirring and mixing is far from being an easy task and work still remains to be done in the area of adiabatic mixing parameterizations. A recent study by Smith and Gent (2004) proves that even in the eddy-resolving ocean models adiabatic tracer mixing schemes are preferable over biharmonic horizontal diffusion schemes. This result, along with those presented in this thesis, supports our claim that the degradation of watermass characteristics in the simulations of Treguier et al.

(2005), with a series of state-of-the-art high-resolution z-level models (of which one was eddy-permitting and the rest eddy-resolving), can be attributed not only to the unrealistic horizontal transport of salt mentioned by Treguier et al. (2005) but also to potentially high levels of artificial diapycnal mixing brought about by the horizontal diffusion schemes.

The accuracy of the simulations with an ocean model whose domain covers the subpolar North Atlantic can be further improved by coupling a sea ice model to the ocean model. The sea ice model has to have good conservation properties, and should be able to predict accurately the extent of the ice pack and to handle large deformations that occur near the free edge, in the Marginal Ice Zone. It is also very important that an appropriate sea ice rheology be used. This will allow for a realistic mechanical behaviour of pack ice and, consequently, lead to the simulation of sea ice deformation features that are still hard to simulate, such as shear bands. If the model domain includes straits such as the Fram and Denmark straits, both the sea ice mechanics and the model resolution will play a major role in the amount of the sea ice that flows through these straits, and that will eventually contribute to the freshwater budget of the subpolar gyre.

The second part of this thesis presents a particle model for sea ice dynamics that has been developed to have many of the desirable abilities mentioned above. It has been shown that the model has considerable skill in simulating complex sea ice dynamics (with a viscous-plastic rheology). Of much interest is its ability to simulate localized shearing in the interior of the ice pack, which occurs at the boundary of floe-aggregates. The development of such shear bands is known to have a steering effect on the sea ice motion. But, a less obvious effect it may have is that of localized Ekman pumping, which has recently been observed by McPhee et al. (2005) in the Arctic Ocean sea ice cover. McPhee et al. (2005) have shown that this leads to a localized pycnocline upwelling, which in turn results in increased ocean heat flux. Before the particle model can be coupled to an ocean model, it needs a thermodynamic component. Furthermore, among the features the model should have to be able to provide reliable long-term simulations is the ability to vary its resolution by increasing/decreasing the number of particles, where and when this is required.

Returning to the ocean model used in the first part, it is expected that a fresher LSW will be produced by coupling it to a sea ice model. Thus, a slightly modified density class distribution of the water mass in the computational domain is very likely to result. This may lead to LSW being lighter than the waters overlying it on the western flank of the Mid-Atlantic Ridge (MAR). In such circumstances, the eastward spreading of the model LSW, currently blocked by the MAR in the stand-alone ocean model, could extend into the eastern North Atlantic basin and thus be in better agreement with the observed pathways. The simulation of a third eastward pathway, in addition to the two obtained in the improved simulations with the stand-alone ocean model will complete the set of the known pathways of the LSW dispersal in the subpolar gyre of North Atlantic Ocean.

Bibliography

McPhee, M. G., R. Kwok, R. Robins, and M. Coon, 2005: Upwelling of Arctic pycnocline associated with shear motion of sea ice. *Geophys. Res. Lett.*, **32**, L10616, doi:10.1029/2004GL021819.

Smith, R. D. and P. R. Gent, 2004: Anisotropic Gent-McWilliams parameterization for ocean models. *J. Phys. Oceanogr.*, **34**, 2541–2564.

Treguier, A. M., S. Theetten, E. P. Chassignet, T. Penduff, R. Smith, L. Talley, J. O. Beismann, and C. Böning, 2005: The North Atlantic Subpolar Gyre in four high-resolution models. *J. Phys. Oceanogr.*, **35**, 757–774.

Appendix A

Details of the Length-Scale Algorithm

The algorithm for determining the length scale entering the expression of the variable eddy transfer coefficient (2.2) is attributed to the Hadley Centre, and is described in more detail in the MOM3 manual (Pacanowski and Griffies, 1998). In our model, this length scale is calculated separately at *ugent* and *vgent* velocity points on a C-grid, using the same algorithm, and an upper limit is imposed on its value. At a given *ugent* velocity grid point, the algorithm starts by setting the length scale equal to Δy (the meridional grid spacing), which is also $max(\Delta x, \Delta y)$. If the growth rate at this point is less than a threshold value of $1.4 \times 10^{-6}\ s^{-1}$ (Wright, 1997), which is equivalent to a time scale greater than 8.25 days, then the length scale remains unchanged. Otherwise it is considered that the grid point may belong to a larger baroclinic region. In the latter case, a search is performed in the four directions of the neighbouring *ugent* grid points to determine the extent of this region. The search is stopped when a node with a growth rate smaller than the threshold value is encountered. Such a node is considered outside the baroclinic region, and the distance to it is evaluated. The length scale corresponding to the given grid point will then be calculated from the four distances thus determined. Since we want to avoid the parameterization of the effects of the resolved eddies, we consider limiting the search to the first node in each of the four directions as acceptable. In the limiting case in which all four neighbouring *ugent* grid points are found to belong to the baroclinic region associated with the given *ugent* grid point, the algorithm returns a maximum value of $3\Delta x = min(3\Delta x, 3\Delta y)$ for the length scale, which corresponds to 1° of latitude in our model. Note that this value is smaller than the upper bound $3\Delta y$ (1° of longitude) imposed to the unresolved baroclinic eddies in the model. Notice also that the square of the maximum length scale will be almost one order of magnitude larger than the square of the minimum value, at the same latitude. Consequently, the maximum value of the eddy transfer coefficient will differ by roughly one order of magnitude from its minimum value, for the same value of the growth rate.

Appendix B

Estimating the Artificial Change in Ice Volume due to Time-stepping

Let us first estimate the change in ice volume during the prediction step. From (4.66), (4.67), and (4.68), we get

$$\begin{aligned} A^\star_{n+1}S^\star_{n+1}h^\star_{n+1} &= A_nS_nh_n(1+\delta t R_{A,n})(1+\delta t R_{S,n})(1+\delta t R_{h,n}) \\ &= A_nS_nh_n[1+\delta t(R_{A,n}+R_{S,n}+R_{h,n}) \\ &\quad +\delta t^2(R_{A,n}R_{S,n}+R_{S,n}R_{h,n}+R_{A,n}R_{h,n})) \\ &\quad +\delta t^3 R_{A,n}R_{S,n}R_{h,n}]. \end{aligned} \tag{B.1}$$

But, $R_{A,n}+R_{S,n}+R_{h,n} = \overline{\beta}_n - \overline{\beta}_n[1-\alpha_n\Gamma(-\overline{\beta}_n)] - \overline{\beta}_n\alpha_n\Gamma(-\overline{\beta}_n) = 0$. Hence, the term proportional to δt vanishes. Note that $R_{A,n} = O(\overline{\beta})$, $R_{S,n} = O(\overline{\beta})$, and $R_{h,n} = O(\overline{\beta})$. Denoting the product $\delta t\overline{\beta}$ by ε, we get

$$\varepsilon = O(10^{-4}) \ll 1, \ \text{ for } \delta t = O(10^2\ s) \ \text{ and } \overline{\beta} = O(10^{-6}\ s^{-1}), \tag{B.2}$$

that is for the typical values of time step and dilation rate, in our simulations. Therefore, according to (B.1), we can write

$$A^\star_{n+1}S^\star_{n+1}h^\star_{n+1} = A_nS_nh_n(1+O(\varepsilon^2)). \tag{B.3}$$

Thus, the relative change in ice volume during the prediction step – used as an error indicator – will be

$$E_{\delta t} = \frac{A^\star_{n+1}S^\star_{n+1}h^\star_{n+1} - A_nS_nh_n}{A_nS_nh_n} = O(\varepsilon^2) \sim 10^{-8}. \tag{B.4}$$

It can be easily shown that the error for the entire time step is on the same order of magnitude, as the corrector step does not make any significant contribution. An error on the order of 10^{-8} for a time step on the order of 10^2 s gives an error on the order of 10^{-5} day^{-1}. A confirmation of the accuracy of this error estimation is given by the plot of the particle ice volume error obtained in one of our simulations after 5 days of integration from rest (Fig. 4.1). This allows us to conclude that the artificial change in ice volume over time scales of the order of days is negligible.

Bibliography

Pacanowski, R. C. and S. M. Griffies, 1998: *MOM 3.0 Manual*. NOAA/Geophysical Fluid Dynamics Laboratory, Princeton, USA 08452.

Wright, D. K., 1997: A new eddy mixing parametrization and ocean general circulation model. *International WOCE Newsletter*, **26**, 27–29.